THE UNIVERSITY OF MANITOBA

TURBULENT FLOW IN AN EQUILATERAL TRIANGULAR DUCT

by

Alex D. Gerrard

A THESIS

SUBMITTED TO THE FACULTY OF GRADUATE STUDIES

IN PARTIAL FULFILLMENT OF THE REQUIREMENTS

FOR THE DEGREE OF MASTER OF SCIENCE

DEPARTMENT OF MECHANICAL ENGINEERING

WINNIPEG, MANITOBA

February, 1976

"TURBULENT FLOW IN AN

EQUILATERAL TRIANGULAR DUCT"

by

ALEX D. GERRARD

A dissertation submitted to the Faculty of Graduate Studies of the University of Manitoba in partial fulfillment of the requirements of the degree of

MASTER OF SCIENCE

ABSTRACT

An experimental investigation of fully developed turbulent flow in an equilateral triangular duct at Reynolds numbers between 53,000 and 107,300 is described. By measuring one component of the secondary velocity, the secondary flow pattern was shown to consist of six counter-rotating cells bounded by the corner bisectors. Secondary flows were directed into the corners via the corner bisector and returned along the wall and wall bisector. A maximum secondary velocity of 1.5% of the bulk velocity was observed. The effects of secondary currents were evident in the distributions of mean velocity, wall shear, and Reynolds stresses and were very prominent in the turbulence kinetic energy distribution. The universal law of the wall can be used to describe the mean axial velocity distribution near the wall although the constants differ somewhat from those for pipe flow. The friction factors were 5.0 - 6.5% lower than pipe friction factors. It is demonstrated that, in order to obtain satisfactory results, techniques for predicting the distributions of mean flow quantities in a triangular duct must allow for secondary flow effects.

TABLE OF CONTENTS

LIST OF FIGURES

NOMENCLATURE

D_h	equivalent hydraulic diameter
E(n)	energy spectrum function
f	friction factor
g_c	dimensional universal constant
H	height of triangular duct
h	distance from duct centerline to midpoint of wall
K_τ	geometry factor for turbulent flow
k_1	yaw sensitivity of hot wire
L	axial distance from inlet of test section
l	one half length of duct sidewall
log	logarithm to the base 10
n	frequency
$\overline{P}$	mean static pressure
$\Delta\overline{P}$	mean static pressure referred to static pressure 2.65 cm from duct exit
p	fluctuating component of static pressure
$\overline{Q}$	mean flow kinetic energy per unit mass
q	instantaneous turbulence kinetic energy per unit mass
$\overline{q}$	mean turbulence kinetic energy per unit mass
q'	$q' = \overline{U}u + \overline{V}v + \overline{W}w$
Re	Reynolds number = $\frac{U_b D_h}{\nu}$
R_{uv}	correlation coefficient = $\overline{uv}/u'v'$
S	sensitivity of linearized hot wire anemometry system

U	instantaneous axial velocity
$\overline{U}$	mean axial velocity (time averaged)
U_b	bulk velocity
U^+	dimensionless mean axial velocity = $\overline{U}/u^*$
u,v,w	fluctuating components of velocity in the x, y and z directions
u',v',w'	root mean square values of velocity fluctuations in the x, y and z directions
u^*	friction velocity
V, W	instantaneous components of velocity parallel and normal to base of duct
$\overline{V}$, $\overline{W}$	mean velocities parallel and normal to base of duct
η	dimensionless distance from wall = $\frac{z\,u^*}{\nu}$.
μ	viscosity
ν	kinematic viscosity = μ/ρ
ρ	density
τ_w	wall shear stress
Ω	mean axial vorticity

Subscripts

loc	local

TURBULENT FLOW IN AN EQUILATERAL TRIANGULAR DUCT

1.0 INTRODUCTION

1.1 Motivation

Most nuclear fuel designs involve the transfer of heat from the elements of a rod bundle to an axial flow of coolant at high Reynolds numbers. Past studies of this heat transfer process have usually consisted of full scale experiments to evaluate bulk-average quantities such as pressure drop, heat transfer coefficients and subchannel mixing for a particular design and range of conditions. Due to the random nature of these experiments and the complex geometry of fuel bundles (Figure 1), it has not been possible to combine the existing heat transfer data in the form of simple correlations. A more fundamental knowledge of the turbulence structure in rod bundle flows is therefore important both for the analysis of experimental results and for the development of numerical techniques for predicting hydraulic and thermal performance.

Some fundamental studies of the structure of fully developed turbulent flow have been conducted in triangular array rod bundles [1,2,3]. These investigations indicate that rod bundle flows are strongly influenced by secondary velocities of the type arising in all straight non- axisymmetric flow passages under turbulent flow conditions. Although the secondary velocities are relatively small, they produce a spiral motion in the mean flow which convects kinetic energy and momentum in the plane normal to the main flow axis. A detailed knowledge of secondary velocities and their effects on the primary flow is of key importance. Certain effects such as the homogenization of local wall shear stress have been quantized. At present, however, there are no reliable measurements of secondary flows in rod bundle geometries. Hall and Svenningsson[2] attempted direct measurements of secondary velocities,but their results were not conclusive and they recommended further investigation. Similarly, although Trupp and Azad[3] could infer the direction and approximate magnitude of secondary flows from momentum and energy balances, they were unable to measure the tiny secondary velocities via conventional X-probes and a three-wire probe.

The present work constitutes the first phase of a continuation of rod bundle work[3] at the University of Manitoba. It involves an experimental investigation of the turbulence structure and secondary flows in fully developed turbulent flow in an equilateral triangular duct. This duct represents a simplification of a single subchannel in a triangular array rod bundle with a pitch to diameter ratio of 1.0. The triangular shape was chosen because it could easily be fabricated with a high degree of accuracy. Much of the information obtained in the triangular duct will be applicable to a subchannel in a triangular array rod bundle in spite of the differences in geometry. In addition, the triangular test section will provide a convenient facility for the future development of a secondary flow meter which can be used in rod bundles. The present work also contributes, in its own right, to the existing knowledge of turbulent duct flows since triangular ducts have received little attention to date.

1.2 Scope and Objectives

The present work was undertaken to establish the mean velocity fields, turbulence structure, and secondary flow patterns in fully developed turbulent flow in an equilateral triangular duct. The first phase of the work included the design and construction of a suitable test section to be attached to an existing wind tunnel. The wind tunnel layout and duct cross-section are shown in Figures 2 and 3 respectively.

The second phase of the work involved an experimental investigation of the fully developed flow near the exit of the test section. After initial measurements to verify flow symmetry, all measurements were made at the grid points shown in Figure 4. These grid points cover one of the six symmetric flow areas which are formed by lines of symmetry and which Trupp and Azad[3] refer to as primary flow cells.

The results of mean velocity and Reynolds stress measurements conducted at Reynolds numbers of 53,000, 81,000, and 107,300 are discussed in subsequent portions of this report. Additional data on local wall shear stresses and axial power spectra are also included. Information concerning secondary flows includes inferences derived from momentum balances and direct X-probe measurements of one component. Further exploration of the secondary velocities has been planned as a continuation of the present project.

2.0 LITERATURE REVIEW

Very few publications in the open literature have dealt with turbulent flow in triangular ducts. The first work to appear was that of Nikuradse[4] who, in 1930, presented mean axial velocity profiles for several triangular duct shapes. Nikuradse noted that isovel lines in these ducts tended to bulge towards the corners. This phenomenon had also been observed in an earlier study[5] in rectangular ducts and had been explained[6] by the postulated existence of secondary currents which transported momentum from the center region of the duct to the corner region. Flow visualization studies by Nikuradse[4] confirmed the presence of secondary flows in an equilateral triangle. As predicted, secondary flows are bounded by the corner bisectors which divide the triangle into six primary flow cells. The isovels are distorted by the convection of high momentum fluid into the corner via the bisector of the corner angle, and by the transport of low momentum fluid out along the wall and finally along the wall bisector. No flow crosses the lines of symmetry and, as illustrated by Figure 3, flow cells on opposite sides of a symmetry line are counter-rotating.

Cremers and Eckert[7] have published measurements of the mean axial velocity and five Reynolds stresses in an isosceles triangle with an aspect ratio of 5 to 1. They reported that there was no experimental evidence of secondary flows at a Reynolds number of 10,900 although contour plots of axial velocity fluctuations strongly suggest the presence of secondary flows near the base. At a Reynolds number of 5480, Cremers and Eckert noted a region near the apex in which no velocity fluctuations could be detected. A recent study by Bandopadhayay and Hinwood[8] confirms that, for a range of Reynolds numbers, laminar and turbulent flows may coexist near the apex of high aspect ratio triangular ducts. Cremers and Eckert also reported that, in the Reynolds number range from 5,000 to 10,000, fluctuating quantities in a triangle do not become Reynolds number independent when normalized by friction velocity. Laufer[9] had previously established that, in the case of fully developed pipe flow, the friction velocity could be used as a scaling factor to remove the Reynolds number dependence of turbulence quantities. Although pipe flow has been studied extensively since Laufer's original work, his investigation is probably the most comprehensive of any to date.

Of particular interest in the present investigation is the work done on secondary flows in fully developed turbulent flow in square ducts. Secondary flows are common to all turbulent flows in straight noncircular ducts, but the square duct has been studied the most extensively. As previously mentioned, Nikuradse[5] first noticed the distortion of isovels in a square duct in 1926 and Prandtl[6] attributed these distortions to secondary flows circulating in closed cells and bounded by lines of symmetry. However, it was not until 1960 that Hoagland[10], using a sensitive, rotatable hot-wire probe, was able to make quantitative measurements of the transverse velocity components. His measurements confirmed the flow patterns suggested by Prandtl and indicated that the ratio of secondary velocity to centerline velocity reached a maximum value of 1 to 1 1/2 percent near the corners. Hoagland also found that wall shear stresses in a square duct were almost uniform everywhere except in the corners. He concluded that secondary flows, by the convection of axial momentum, have a significant effect on the axial velocity distribution throughout most of the flow.

Leutheusser[11] in 1963 found that, while the inner law of velocity distribution applied to the wall region of flow in square ducts, the flow near the center of the duct does not follow the outer law formulation. He also postulated that the strength of secondary flows decreased with increasing Reynolds number.

Brundrett and Baines[12] carried out an investigation of the origin and dissipation of secondary flows by examining the mean axial vorticity equation. Their measurements of the Reynolds stresses indicate that the production of axial vorticity occurs along the bisector near the corner. Although they were able to show that secondary flows are the result of Reynolds stress gradients, they did not examine the turbulence mechanism producing the gradients.

Some further aspects of square duct flow were studied by Gessner and Jones[13]. They examined the Reynolds equation along a secondary flow streamline and concluded that secondary flows were caused by a complex interaction of Reynolds stresses and static pressure gradients. They also concluded that secondary flow velocities normalized with either bulk or centerline velocities decrease with increasing Reynolds numbers. Finally, their measurements showed that the greatest skewness of the wall shear stress occurs in the corners and that, in the cross-sectional plane, Reynolds stress principal planes are not normal and tangent to isovels.

Using ducts of different roughness Launder and Ying[14] determined that the friction velocity was the appropriate scaling factor to remove the Reynolds number and surface roughness dependency of secondary velocities.

In 1973, Gessner[15] conducted a study of the origins of secondary flows based on the experimental evaluation of terms in the mean energy and vorticity balance equations applied along a corner bisector in developing turbulent flows. His results indicated that secondary flows are initiated and sustained as a result of turbulent shear stress gradients normal to the bisector. He also concluded that the transport of turbulent kinetic energy and axial vorticity are second order effects of secondary flows, and the equations governing these processes do not govern the generation of secondary flows. First order effects are classified as the convection of axial momentum, total energy of the mean flow, and transverse vorticity. These conclusions are apparently applicable to all geometries, including exterior corners, which involve changes of curvature of isovels.

Although most studies of secondary flow patterns have involved square ducts, some work has been done in other duct shapes. Liggett et al[16] investigated secondary currents in an open triangular channel. Rectangular ducts have been studied by Hoagland[10], Leutheusser[11], Gessner and Jones[13], and Tracey[17]. Kacker[18] studied a circular pipe with one or two eccentric rods. For the two pin geometry, he identified two counter-rotating secondary flow cells in each symmetric quadrant. As is the case for square ducts, Kacker concluded that secondary flows have a significant influence on mean velocity and wall shear stress distributions.

Based on turbulence measurements in a rectangular duct with roughened sections of wall and consideration of the turbulent kinetic energy equations, Hinze[19] has proposed a general rule pertaining to the existence of secondary flows. This rule states that, when in a localized region the production of turbulent kinetic energy greatly exceeds viscous dissipation, there must be a secondary current that transports turbulence poor fluid into this region and turbulence rich fluid out.

There have been at least three attempts to compute mean velocity profiles and wall shear stress distributions in equilateral triangular ducts. The first attempt was made in 1954 by Deissler and Taylor[20] who developed an iterative technique based on the eddy diffusivity in a tube. They ignored secondary flows and assumed that shear stresses normal to isovels were negligible. The isovels obtained by this method had the same general shape as the experimental curves of Nikuradse[4] but did not penetrate as far into the corners.

A second technique, which is limited to prediction of wall shear stress distributions but includes the effects of secondary flows, was suggested by Kogorev et al[21] in 1971. In this technique, the axial momentum equation is written in eddy viscosity form and integrated by using an assumed universal velocity distribution and experimental data for secondary flows. For a square duct, Kogorev found that agreement between measured and predicted distributions was improved by including secondary flow effects. Using a secondary flow pattern obtained by transformation of square duct data, Kogorev also found that secondary flows tend to equalize the distribution of the wall shear stress about the perimeter of an equilateral triangle.

Finally, the finite element technique was adapted to the calculation of mean velocity and wall shear stress distributions in noncircular ducts by Gerard[22] in 1974.

His technique uses an eddy viscosity model to account for Reynolds shear stresses and requires information describing secondary flows as input data if their effects are to be taken into account. He applied the technique to an equilateral triangle by ignoring secondary flows and obtained results with the same deficiencies as the results obtained by Deissler and Taylor. In an effort to quantify the effects of secondary flows, the case of a square duct was considered with and without secondary flow data as input. The inclusion of secondary flow effects significantly improved the accuracy of his predictions. He concluded that secondary flows are responsible for the distorted isovels and unexpectedly uniform wall shear stress distributions found in turbulent flow in noncircular conduits.

3.0 THEORETICAL CONSIDERATIONS

In a duct with the cross-section of an equilateral triangle, flow properties are symmetric about the corner bisectors. As illustrated in Figure 3, this property of symmetry can be used to subdivide the duct cross-section into six primary flow cells. Each of these cells is identical when viewed with respect to rotated coordinate systems and no net mass or energy is transferred across their boundaries. A knowledge of the flow properties in one cell is therefore sufficient to describe the entire flow field.

The primary cell and coordinate system considered in the present investigation are shown in Figure 3. Equations governing the conservation of mass, momentum, axial vorticity and energy in this system are presented below. These equations are applicable to the isothermal, fully developed, turbulent flow of a constant property fluid.

3.1 Continuity and Reynolds Equations

Within a primary cell, the only allowable simplifications of the continuity and Reynolds equations are those due to the fully developed flow condition. This condition implies that the velocity fields and axial pressure gradient are independent of the axial coordinate. Consequently, the simplest forms of the continuity equations which can be applied within a flow cell are:

$$\frac{\partial \overline{V}}{\partial y} + \frac{\partial \overline{W}}{\partial z} = 0 \qquad (3.1)$$

$$\frac{\partial u}{\partial x} + \frac{\partial v}{\partial y} + \frac{\partial w}{\partial z} = 0 \qquad (3.2)$$

The Reynolds equations for fully developed flow within a primary cell are:

X - direction

$$\overline{V}\frac{\partial \overline{U}}{\partial y} + \overline{W}\frac{\partial \overline{U}}{\partial z} = -\frac{1}{\rho}\frac{\partial \overline{P}}{\partial x} + \nu\left(\frac{\partial^2 \overline{U}}{\partial y^2} + \frac{\partial^2 \overline{U}}{\partial z^2}\right) - \left(\frac{\partial \overline{uv}}{\partial y} + \frac{\partial \overline{uw}}{\partial z}\right) \qquad (3.3)$$

Y - direction

$$\overline{V}\frac{\partial \overline{V}}{\partial y} + \overline{W}\frac{\partial \overline{V}}{\partial z} = -\frac{1}{\rho}\frac{\partial \overline{P}}{\partial y} + \nu\left(\frac{\partial^2 \overline{V}}{\partial y^2} + \frac{\partial^2 \overline{V}}{\partial z^2}\right) - \left(\frac{\partial \overline{v^2}}{\partial y} + \frac{\partial \overline{vw}}{\partial z}\right) \qquad (3.4)$$

Z - direction

$$\overline{V}\frac{\partial \overline{W}}{\partial y} + \overline{W}\frac{\partial \overline{W}}{\partial z} = -\frac{1}{\rho}\frac{\partial \overline{P}}{\partial z} + \nu\left(\frac{\partial^2 \overline{W}}{\partial y^2} + \frac{\partial^2 \overline{W}}{\partial z^2}\right) - \left(\frac{\partial \overline{vw}}{\partial y} + \frac{\partial \overline{w^2}}{\partial z}\right) \qquad (3.5)$$

The Reynolds equation for the X - direction can be interpreted as an expression for the change in axial momentum of a small element of fluid. The roles of the various terms are more easily understood if the equation is rearranged in the following form:

$$-\frac{1}{\rho}\frac{\partial\overline{P}}{\partial x} = \overline{V}\frac{\partial\overline{U}}{\partial y} + \overline{W}\frac{\partial\overline{U}}{\partial z} - \nu\left(\frac{\partial^2\overline{U}}{\partial y^2} + \frac{\partial^2\overline{U}}{\partial z^2}\right) + \left(\frac{\partial\overline{uv}}{\partial y} + \frac{\partial\overline{uw}}{\partial z}\right) \tag{3.6}$$

The first term in equation 3.6, $-\frac{1}{\rho}\frac{\partial\overline{P}}{\partial x}$, represents the change in axial momentum due to the axial pressure gradient. Its magnitude is constant over the cross-section as can be verified by differentiating equations 3.3, 3.4 and 3.5 with respect to x.

On the right hand side of equation 3.6, the two bracketed terms represent the change in momentum due to viscous and Reynolds shear stresses. The two remaining terms indicate that changes in the axial momentum of a small fluid particle occur as a result of convection by secondary flows. These terms represent an important difference between flow in circular and noncircular ducts.

At the cell boundaries, the Reynolds equations can be simplified by using the following boundary conditions:

(1) Along the y axis or wall boundary

$\overline{U} = \overline{V} = \overline{W} = u = v = w = 0$

and $\frac{\partial}{\partial y} = 0$

due to the no-slip condition.

(2) Along the z axis normal to the midpoint of the wall, $\overline{V} = 0$, since no flow crosses the

cell boundary. Since $\overline{V} = 0$ for all z and is of opposite sign on each side of the z axis, it follows that:

$$\frac{\partial \overline{V}}{\partial z} = \frac{\partial^2 \overline{V}}{\partial z^2} = \frac{\partial^2 \overline{V}}{\partial y^2} = 0$$

Due to symmetry about the z axis, it can also be shown that:

$$\frac{\partial \overline{u^2}}{\partial y} = \frac{\partial \overline{v^2}}{\partial y} = \frac{\partial \overline{w^2}}{\partial y} = \frac{\partial \overline{U}}{\partial y} = \frac{\partial \overline{W}}{\partial y} = \frac{\partial \overline{P}}{\partial y} = 0$$

By applying the above simplifications, equation 3.4 reduces to:

$$\frac{\partial \overline{vw}}{\partial z} = 0$$

Upon integration, and using the boundary condition $\overline{vw} = 0$ at the wall, one obtains $\overline{vw} = 0$ for all z.

(3) Along the corner bisector, the condition that no net flow crosses the boundary implies that:

$$\overline{V} = -\sqrt{3}\,\overline{W}$$

Due to symmetry along this boundary

$$\frac{\partial \overline{u^2}}{\partial n} = 0$$

where n is the direction normal to the diagonal.

It should be noted that symmetry about the cell boundaries does not imply that the gradients of all quantities are zero across these boundaries. For example, $\overline{V}$ has an antisymmetric distribution about the z axis and $\partial\overline{V}/\partial y$ can have finite values along the z axis.

Using the above simplifications, the Reynolds equations at the wall become:

X - direction

$$0 = -\frac{1}{\rho}\frac{\partial\overline{P}}{\partial x} + \nu\frac{\partial^2\overline{U}}{\partial z^2} - \frac{\partial\overline{uw}}{\partial z} \tag{3.7}$$

Y - direction

$$0 = -\frac{1}{\rho}\frac{\partial\overline{P}}{\partial y} + \nu\frac{\partial^2\overline{V}}{\partial z^2} - \frac{\partial\overline{vw}}{\partial z} \tag{3.8}$$

Z - direction

$$0 = -\frac{1}{\rho}\frac{\partial\overline{P}}{\partial z} + \nu\frac{\partial^2\overline{W}}{\partial z^2} - \frac{\partial\overline{w^2}}{\partial z} \tag{3.9}$$

Along the z axis from the midpoint of the wall to the duct centerline, the Reynolds equations reduce to the following forms:

X - direction

$$\frac{1}{\rho}\frac{\partial\overline{P}}{\partial x} = -\overline{W}\frac{\partial\overline{U}}{\partial z} + \nu\left(\frac{\partial^2\overline{U}}{\partial y^2} + \frac{\partial^2\overline{U}}{\partial z^2}\right) - \left(\frac{\partial\overline{uv}}{\partial y} + \frac{\partial\overline{uw}}{\partial z}\right) \tag{3.10}$$

Y - direction

$$0 = 0 \tag{3.11}$$

Z - direction

$$\frac{1}{\rho}\frac{\partial \overline{P}}{\partial z} = - \overline{W}\frac{\partial \overline{W}}{\partial z} + \nu\left(\frac{\partial^2 \overline{W}}{\partial y^2} + \frac{\partial^2 \overline{W}}{\partial z^2}\right) - \left(\frac{\partial \overline{vw}}{\partial y} + \frac{\partial \overline{w^2}}{\partial z}\right) \tag{3.12}$$

It is of interest to examine equation 3.10 in more detail to see if anything can be learned about the distribution of $\overline{uw}$ along the z axis. First consider the viscous stress contribution. Due to the relatively flat axial velocity distribution, it is expected that the term $\partial^2\overline{U}/\partial z^2$ will be significant only very near the wall and $\partial^2\overline{U}/\partial y^2$ will be negligible everywhere. For points not too close to the wall both of these terms can therefore be ignored. Inspection of the remaining terms indicates that no further simplifications can be made. For example, the gradient of $\overline{uv}$ with respect to y may take on non-zero values since $\overline{uv}$ has an antisymmetric distribution about the z axis. $\overline{W}$ may also have a finite value everywhere except at the wall and the duct centerline. As a result, the simplest form to which equation 3.10 can be reduced is :

$$\frac{1}{\rho}\frac{\partial \overline{P}}{\partial x} = - \overline{W}\frac{\partial \overline{U}}{\partial z} - \left(\frac{\partial \overline{uv}}{\partial y} + \frac{\partial \overline{uw}}{\partial z}\right) \tag{3.13}$$

Evidently, it is not possible to obtain a theoretical distribution of $\overline{uw}$ without a detailed knowledge of the various quantities in equation 3.13.

3.2 Axial Vorticity

As derived by Brundrett and Baines(12), the equation governing conservation of axial vorticity is:

$$\bar{V}\frac{\partial\Omega}{\partial y} + \bar{W}\frac{\partial\Omega}{\partial z} = \frac{\partial^2}{\partial y\partial z}(\overline{v^2} - \overline{w^2}) - \left(\frac{\partial^2\overline{vw}}{\partial y^2} - \frac{\partial^2\overline{vw}}{\partial z^2}\right)$$
$$+ \nu\left(\frac{\partial^2\Omega}{\partial y^2} + \frac{\partial^2\Omega}{\partial z^2}\right) \qquad (3.14)$$

The terms on the left hand side of equation 3.14 represent the change in axial vorticity due to convection along a secondary flow streamline while the viscous terms on the right hand side represent the diffusion of vorticity down its gradient. Depending on the local turbulence field, the remaining terms may represent either production or dissipation of axial vorticity.

3.3 Energy Equations

A mean energy equation can be obtained by multiplying equations 3.3, 3.4 and 3.5 by $\bar{U}$, $\bar{V}$ and $\bar{W}$ respectively and adding the resultant equations. After rearrangement and simplification using the continuity equation, the mean energy equation for flow in a triangular duct can be written as follows:

$$\bar{U}\,\frac{\partial \bar{P}}{\partial x} + \rho\frac{\partial}{\partial y}\,\bar{V}\,(\bar{Q} + \frac{\bar{P}}{\rho}) + \rho\frac{\partial}{\partial z}\,\bar{W}\,(\bar{Q} + \frac{\bar{P}}{\rho})$$

I II

$$+ \rho\frac{\partial}{\partial y}\,\overline{vq'} + \rho\frac{\partial}{\partial z}\,\overline{wq'}$$

III

$$-\rho\,[\overline{uv}\frac{\partial \bar{U}}{\partial y} + \overline{uw}\frac{\partial \bar{U}}{\partial z} + \overline{v^2}\frac{\partial \bar{V}}{\partial y} + \overline{w^2}\frac{\partial \bar{W}}{\partial z} + \overline{vw}\,(\frac{\partial \bar{V}}{\partial z} + \frac{\partial \bar{W}}{\partial y})\,]$$

IV

$$-\mu\,[\frac{\partial^2 \bar{Q}}{\partial y^2} + \frac{\partial^2 \bar{Q}}{\partial z^2}\,] - \mu\,(\frac{\partial \bar{V}}{\partial y})^2 - \mu\,(\frac{\partial \bar{W}}{\partial z})^2 - 2\mu\,\frac{\partial \bar{V}}{\partial z}\,\frac{\partial \bar{W}}{\partial y}$$

V

$$+ \mu\,[2\,(\frac{\partial \bar{V}}{\partial y})^2 + 2\,(\frac{\partial \bar{W}}{\partial z})^2 + (\frac{\partial \bar{U}}{\partial y})^2 + (\frac{\partial \bar{U}}{\partial z})^2 + (\frac{\partial \bar{V}}{\partial z} + \frac{\partial \bar{W}}{\partial y})^2\,] = 0$$

VI

(3.15)

where

$$\bar{Q} = \frac{1}{2}\,[\bar{U}^2 + \bar{V}^2 + \bar{W}^2\,]$$

$$q' = \bar{U}u + \bar{V}v + \bar{W}w$$

The various terms in equation 3.15 can be given the following physical interpretations:

I = energy input per unit volume and time due to axial pressure drop.

II = change in energy per unit volume and time due to convection of mean energy by secondary flows.

III = change in energy per unit volume and time due to convection by turbulence.

IV = production of turbulence energy per unit volume and time.

V = viscous diffusion of mean flow energy.

VI = direct viscous dissipation per unit volume and time.

The mechanical energy balance equation for turbulence, as derived by Hinze[19], is:

$$\frac{\partial}{\partial y} \overline{V}\, \overline{q} + \frac{\partial}{\partial z} \overline{W}\, \overline{q}$$

VII

$$+ \frac{\partial}{\partial y} \overline{v\left(q + \frac{P}{\rho}\right)} + \frac{\partial}{\partial z} \overline{w\left(q + \frac{P}{\rho}\right)}$$

VIII

$$+ \overline{uv} \frac{\partial \overline{U}}{\partial y} + \overline{uw} \frac{\partial \overline{U}}{\partial z} + \overline{vw} \left(\frac{\partial \overline{V}}{\partial z} + \frac{\partial \overline{W}}{\partial y}\right) - (\overline{w^2} - \overline{v^2}) \frac{\partial \overline{V}}{\partial y}$$

IX

$$- \nu \frac{\partial}{\partial y} [\overline{u \left(\frac{\partial u}{\partial y} + \frac{\partial v}{\partial x}\right) + 2v \frac{\partial v}{\partial y} + w\left(\frac{\partial w}{\partial y} + \frac{\partial v}{\partial z}\right)}]$$

$$- \nu \frac{\partial}{\partial z} [\overline{u \left(\frac{\partial u}{\partial z} + \frac{\partial w}{\partial x}\right) + v\left(\frac{\partial v}{\partial z} + \frac{\partial w}{\partial y}\right) + 2w \frac{\partial w}{\partial z}}]$$

X

$$+ \nu [2 \overline{\left(\frac{\partial u}{\partial x}\right)^2} + 2 \overline{\left(\frac{\partial v}{\partial y}\right)^2} + 2 \overline{\left(\frac{\partial w}{\partial z}\right)^2} + \overline{\left(\frac{\partial u}{\partial y}\right)^2} + \overline{\left(\frac{\partial u}{\partial z}\right)^2}$$

$$+ \overline{\left(\frac{\partial v}{\partial x}\right)^2} + \overline{\left(\frac{\partial v}{\partial z}\right)^2} + \overline{\left(\frac{\partial w}{\partial x}\right)^2} + \overline{\left(\frac{\partial w}{\partial y}\right)^2} + 2 \overline{\left(\frac{\partial v}{\partial x}\right) \left(\frac{\partial u}{\partial y}\right)}$$

$$+ 2 \overline{\left(\frac{\partial w}{\partial x}\right) \left(\frac{\partial u}{\partial z}\right)} + 2 \overline{\left(\frac{\partial w}{\partial y}\right) \left(\frac{\partial v}{\partial z}\right)}] = 0$$

XI (3.16)

where

$$\overline{q} = \frac{1}{2} [\overline{u^2} + \overline{v^2} + \overline{w^2}]$$

$$q = \frac{1}{2} [u^2 + v^2 + w^2]$$

Physically the terms in equation 3.16 represent the following effects:

VII = convection of mean turbulence kinetic energy by secondary flows.

VIII = convection of turbulence kinetic and pressure energy by the turbulence.

IX = production of turbulence energy.

X = energy diffusion due to viscous effects.

XI = viscous dissipation of the turbulent motion.

A mean total energy equation can be obtained by multiplying equation 3.16 by the density and adding with equation 3.15. Since the term describing production of turbulence has opposite signs in the two equations, it will disappear. All other terms will appear in the total energy equation and will have the physical interpretations described above.

4.0 EXPERIMENTAL APPARATUS

The present work included the design and construction of a test section and traversing mechanism to be used in conjunction with an existing wind tunnel. Figure 2 shows the wind tunnel and test section layout. A brief description of the components is given below.

4.1 Wind Tunnel

The wind tunnel portion of the present facility was used previously by Trupp and Azad[3] in their investigation of rod bundle flow. For the present work, the wind tunnel was modified to operate in the open circuit mode. As shown in Figure 2, atmospheric air was drawn through a contraction cone by four counter-rotating axial aerofoil fans. Each of these fans was powered by a two speed motor which could be used for air flow control. A damper was located just upstream of the fans for finer flow adjustments and fan vibrations were isolated by a canvas coupling and silencer at the exit of the fan section.

Following the silencer, air passed through two sets of turning vanes, a screen section, and a circular contraction cone before entering a transition section. In this section, the flow area was gradually reduced and transformed to match the cross-section of the triangular test section. Air discharged through the open end of the triangular duct.

4.2 Test Section

As shown in Figure 2, the triangular test section consisted of a wooden entrance length and a final acrylic section. The entrance length totalled 7.32 m in length and was fabricated in 3 lengths from 2 cm thick mahogany plywood. A 2.44 m sheet of 2 cm thick clear acrylic plastic was used for the remaining section. The overall length of the duct was 9.76 m and the length of the interior sidewalls was 12.70 cm.

Both the wooden and acrylic sections were constructed from three interlocking walls as shown in Figure 3. The walls were fastened in place with closely spaced screws and all joints were sealed from the outside with a flexible silicone sealant. This method of construction provided accurate control of the interior dimensions and ensured a leak free duct. It is estimated that variations in the sidewall lengths were less than $\pm$ 0.25 mm and $\pm$ 1.0 mm for the acrylic and wooden sections respectively.

Prior to assembly, all interior wooden surfaces were varnished, sanded, and waxed to ensure a hydraulically smooth surface. Irregularities in the acrylic section were removed with a polishing compound. During assembly, great care was taken in matching the joints and aligning the sections to ensure that flow symmetry existed at the duct exit.

In order to provide the longest possible entrance length and easy access, the test plane for mean velocity and turbulence measurements was located 2.5 cm inside the open end of the duct. This location corresponded to a distance of about 133 equivalent hydraulic diameters from the test section inlet.

Provision for axial pressure gradient measurements was made by locating static taps at 15.24 cm intervals along the duct length. Taps in the wooden section consisted of 0.8 mm holes drilled midway across the base. In the plastic section, piezometric rings were formed by joining 0.6 mm square edge holes located in the middle of each wall. Connectors for the manometer tubing were epoxied in 8 mm holes drilled behind the small diameter holes.

4.3 Traversing Mechanism

The traversing mechanism shown in Figure 5 provided for accurate positioning of either a pitot tube or hot-wire probe in the test plane. Three directions of motion were possible. Vertical motion was achieved by means of a DISA 55H01 traversing mechanism. This mechanism was mounted on two vernier calipers which allowed up to 15 cm of horizontal travel in the test plane. The vernier scales gave an accurate indication of the horizontal position. Motion in the axial direction was provided by two concentric tubes.

Probes were located by observing their images as they were brought into contact with the shiny acrylic walls. The distance between the active sections of hot wire probes and the wall was measured with a travelling microscope. It was estimated that probe positions could be determined to within $\pm$ 0.05 mm and $\pm$ 0.1 mm in the vertical and horizontal directions respectively.

Most of the mean velocity and turbulence measurements were made at the nodes of a grid covering a flow cell along the duct base. This flow cell was chosen because it allowed the most accurate positioning of the probe in the direction normal to the wall.

4.4 Pitot and Static Pressure Probes

Two pitot tubes, with outside diameters of 1.067 mm and 1.27 mm, were built from stainless steel tubing with an inside to outside diameter ratio of 0.6. A chamfer of approximately 45° was placed on the inside diameters of the upstream ends of these tubes. Both pitot tubes extended 11 cm upstream from the probe holder which was located approximately 8.5 cm outside the duct during testing.

Mean velocity and wall shear stress measurements at the highest Reynolds number were made with the large pitot tube used in conjunction with a Betz Projection Manometer. This manometer has a range of 0 - 400 mm H_2O and an accuracy of $\pm$ 0.05 mm H_2O. An R. Fuess manometer (DISA 134B) and the smaller probe was used at the lower Reynolds numbers. The Fuess manometer had five ranges varying from 0 - 16 mm H_2O to 0 - 160 mm H_2O and an accuracy of $\pm$ 0.5% of full scale.

Static pressures for the mean velocity measurements were determined from the axial pressure drop in the duct and verified by measurements with a commercial static pressure probe and a HERO micromanometer. The static pressure probe was also used to investigate the extent of end effects near the duct exit.

4.5 Hot-Wire Anemometry Equipment

Turbulence measurements were made by using constant temperature linearized hot-wire anemometry. The anemometry systems were manufactured by DISA and consisted of two sets of 55D05 anemometers, 55D10 linearizers, and 55D25 auxiliary units and a single 55D01 anemometer. These systems were operated in conjunction with DISA probes having 1.25 mm sensing lengths of 5 μm platinum plated tungsten wire. The ancillary equipment, consisting of a 55D30 mechanical DC voltmeter, a 55D31 digital DC voltmeter, two 55D35 RMS voltmeters, two 55A06 correlators and a 55D70 correlator, was also manufactured by DISA.

Measurements of axial velocity fluctuations were made with a 55P01 single wire probe powered by the 55D01 anemometer. The 55P01 probe has widely spaced prongs and thick gold plated sections at each end of the sensing length to minimize prong interference[23]. During testing, the probe was operated at an overheat ratio of 0.8 and was positioned with the sensing wire normal to the flow and parallel to the base. The above system was also used in conjunction with a KROHN-HITE model 3700 band pass filter to obtain axial power spectra.

The $\overline{uw}$ and $\overline{uv}$ shear stresses and the three normal Reynolds stress were measured with X-probes and the matched anemometer systems described above. Simultaneous measurements of the shear stresses were made by the one and two correlator methods.[24] A miniature 55P61 probe[23] was used for most measurements of $\overline{uw}$ and w' since its shaft could be placed in contact with the wall even when the X-wires were aligned in the X-Z plane. Measurements of $\overline{uv}$ and v' were made with a gold plated 55P51 probe which is better suited to measurements in high turbulence fields. Both probes had to be operated at less than optimum overheat ratios because of the coarse operating resistance adjustments on the 55D05 anemometers. This feature also prevented exact matching of the operating resistances of the two wires in an X-probe if their cold resistances were not identical. As a result, it was necessary to match the X wire sensitivities by adjusting the amplification of the output signals.

Linearization of both the single wire probes and X-probes was accomplished by varying the tunnel speed while holding the probe at the duct centerline. The probe outputs were then compared with the known centerline velocities. Since the probes tended to drift with extended use, the probe sensitivity for each test was determined by comparing the output voltages with the known velocities at selected grid points. Gain adjustments were made with the auxiliary units.

5.0 RESULTS AND DISCUSSIONS

Measurements characterizing the mean velocity and turbulence fields at a point 2.5 cm from the exit of the triangular duct were made at each of the three nominal test conditions outlined in Table 1. The quantities measured included mean axial and secondary velocities, five Reynolds stresses, local wall shear stresses, and axial power spectra. Because of the symmetry properties referred to previously, most of the measurements were concentrated in one primary flow cell. The grid used for mean velocity and Reynolds stress measurements is shown in Figure 4.

Results of the above measurements and axial pressure drop measurements are presented and discussed in the following sections. The three nominal Reynolds numbers listed in Table 1 are used to identify all test results although the actual Reynolds numbers varied slightly from day to day. Any values of u^* and U_b which were used to non-dimensionalize data were corrected for daily variations in test conditions by the equations in Appendix A.

Reynolds Number	Centerline Velocity $\overline{U}$ - m/s	Avg. Velocity U_b - m/s	Friction Velocity u^* - m/s	Pressure Drop $\frac{d\overline{P}}{dx}$ - $\frac{gm}{sec^2\ cm}$
53,000	14.4	11.5	0.570	2.03
81,100	22.0	17.8	0.834	4.35
107,300	28.4	23.2	1.05	7.03

Table 1

Nominal Test Conditions

5.1 Flow Development and End Effects

The present test section provided an entrance length of 133 hydraulic diameters for flow development. This compares favourably with the required entrance length of less than 49 hydraulic diameters for flow in a circular pipe with boundary layer tripping[9]. Due to differences in geometry and entrance conditions, however, the state of flow development in the triangular test section could not be determined from the above comparison alone. Previous investigations of noncircular duct flows were therefore reviewed to establish whether or not fully developed flow would be achieved at the test station.

A survey of the literature revealed that fully developed turbulent flow has purportedly been achieved in noncircular ducts very much shorter than 133 hydraulic diameters. For example, Gessner and Jones[13] reported that, in a square duct with boundary layer tripping and variable density screens to thicken the boundary layer, fully developed flow was achieved at $L/D_h=40$. In a rectangular duct with only boundary layer tripping, they achieved fully developed flow at $L/D_h=60$. Hinze[19] found that, in a rectangular duct with one wall roughened, fully developed flow was achieved before $L/D_h=127$. In an investigation of fully developed turbulent flow in pipes with one and two eccentric rods, Kacker[18] made measurements at $L/D_h=67$ and $L/D_h=78$ respectively. Unfortunately, Kacker does not state whether or not boundary layer tripping was used.

Some experimenters have carried out investigations of fully developed flow in relatively short, square ducts without boundary layer tripping. For example, Ying(14) used a duct with an entrance length of $L/D_h=69$ and Gessner(15) reported essentially fully developed flow at $L/D_h=84$. In the case of a high aspect ratio (5 to 1) isosceles triangle, Cremers and Eckert(7) reported that, even with boundary layer tripping, an entrance length of 130 hydraulic diameters was required.

Although turbulent flow in an equilateral triangular duct may be somewhat more complex than square duct and pipe flows, it is probably less complex than flow in a high aspect ratio triangle. In light of the above review, it was therefore concluded that fully developed flow would very likely be achieved in the present test section. This conclusion was corroborated to some extent by a series of axial pressure drop measurements which indicated that fully developed flow was achieved at a point 30 hydraulic diameters upstream of the test station.

In order to prevent blockage of the flow at the test station, it was necessary to make turbulence measurements no farther than 2.5 cm inside the open end of the duct. In this position, the probe holder was entirely outside the duct and upstream disturbances due to its presence were found to be negligible. Pitot tube measurements indicated that end effects on the mean velocity field penetrated only about 1 cm.

5.2 Flow Symmetry

A number of tests were conducted to verify that flow at the test station was symmetric. At the mean velocity level, symmetry was checked by comparing Pitot tube readings from symmetric points along horizontal lines or corner bisectors. These tests indicated that, in the Reynolds number range of concern, asymmetrics in the mean velocity field were negligible in comparison with the uncertainties in the Pitot tube readings. For example, the mean absolute percentage differences between a large number of symmetric points were only 0.3% and 0.5% at the highest and lowest Reynolds numbers respectively. The good agreement between measurements in opposite halves of the duct is further illustrated by the superimposed velocity profiles presented in Figure 6.

Symmetry at the turbulence level was investigated by making horizontal traverses with a single hot wire and an X-probe with its wires aligned in the X-Y plane. Measurements of this type indicated a high degree of symmetry in the u' and v' fields. For example, the mean absolute percentage difference between the intensities of u' in opposite halves of the duct was only 1.3%. Variations in v' were equally small. Typical distributions of u' and v' are plotted in Figures 7 and 8.

Measurements to test the symmetry of R_{uv} indicated that it has an antisymmetric distribution about the z axis. As indicated by the results in Figure 9, however, the measured distributions of Ruv did not exhibit the high degree of symmetry characterizing u' and v'. Asymmetries in the form of a bias towards one sign were consistently observed in repeated experiments. The sign and magnitude of the bias appeared to be strongly dependent on the calibration and alignment of the probe. Since this dependence was particularly strong in the midwall region where R_{uv} is very small and the other Reynolds stresses are relatively large, it was concluded that the observed asymmetries were largely the result of experimental error.

In view of the high degree of symmetry in $\overline{U}$, u', and v' fields and the uncertainties in measurements of R_{uv}, it was decided that flow at the test station was, for all practical purposes, symmetric. This result was very important since it allowed subsequent measurements to be concentrated in one flow cell.

5.3 Axial Pressure Drop

The axial pressure distribution at each of the three test Reynolds numbers was determined from measurements at 64 static pressure taps spanning the length of the test section. All upstream measurements were referred to the pressure at a tap 2.65 cm from the open end and reduced by a dynamic pressure based on the bulk velocity. The normalized distributions are plotted in Figure 10 with straight lines faired through the data points for comparison.

No marked entrance region is evident in the plotted axial pressure distributions. At the higher Reynolds numbers, however, the pressure gradient does not attain its final value until $L/D_h=100$. Deviations from the general trend occured consistently at a few imperfect taps.

Friction factors for each Reynolds number were calculated from least square fits of straight lines to the last 16 downstream taps. The results are plotted in Figure 11 along with the empirical Blasius equation for friction factor in a smooth circular tube. On the basis of the equivalent hydraulic diameter concept, the experimental points should coincide with the Blasius equation. However, the experimental points are from 5 to 6.5% lower than the empirical prediction. In this respect, the present results are consistent with reported results for other noncircular ducts. For example, Leutheusser[11] found that friction factors in square ducts were significantly lower than predicted by the hydraulic diameter rule. Carlson and Irvine[25] reported similar results for isosceles triangular ducts. In both cases the magnitudes of the deviations were a function of geometry.

A correction for the above inadequacies in the equivalent hydraulic diameter concept has been suggested by Malak et al[26]. For $Re>10^4$, they report that friction factor and Reynolds number data can be correlated by the following relationship

$$f = 0.184\, K_\tau^{1.2}\, Re^{-0.2} \tag{5.1}$$

The variable K_τ is a function of geometry and can be obtained from the geometric dependence of the friction factor for laminar flow. They suggest a value of $K_\tau = 0.936$ for an equilateral triangle. As shown in Figure 11, equation 5.1 gives a satisfactory representation of the present results when the suggested value of K_τ is employed.

5.4 Local Wall Shear Stress

The local wall shear stress distribution for a primary flow cell was determined by the Preston technique. This technique relates the shear stress at the wall to the dynamic pressure at the open end of a total head tube in contact with the wall. The technique is applicable to any flow in which the velocity distribution for the wall region can be described by the inner law of the wall. Several investigations[27,28] have confirmed the validity of the technique for measuring wall shear in pipe flows and Leutheusser[11] has demonstrated its validity for a square duct with secondary flows. For the present case, the wall similarity requirement described above was tested by comparing velocity profiles in the triangular duct with the inner law of the wall. As discussed in subsequent sections, this comparison showed that the velocity distribution in the wall region can be described by the inner law of the wall when the values of the empirical constants are suitably modified.

Preston tube measurements corresponding to the axial component of wall shear in the triangular test section were obtained by comparing the stagnation pressures at the open end of a Pitot tube with the static pressure at an adjacent wall tap. Pitot tubes with outside diameters of 1.27 and 1.067 mm were used for measurements at the highest and two lower Reynolds numbers respectively. Actual values of the axial component of wall shear were obtained from the appropriate form of Patel's[28] correlations between the measured dynamic pressures and the wall shear in a pipe. The directional characteristics of the wall shear stress were not examined although it has been shown[13] that transverse components do exist in noncircular ducts.

The measured distributions of the axial component of wall shear at three Reynolds numbers are shown in Figure 12. In order to facilitate comparisons, each distribution has been normalized by its integrated average value. The average shear stress values obtained by integrating the local stress distributions ranged from 1.8% to 2.4% lower than the corresponding values obtained from axial pressure drop measurements. The cause of these small, systematic deviations was not apparent.

The shear stress distributions presented in Figure 12 do not show the tendency toward greater uniformity with increasing Reynolds number that Leutheusser[11] observed in a rectangular duct. As shown in Figure 13, however, the distributions at all Reynolds numbers investigated are considerably more uniform than the computed distributions of Deissler and Taylor[20] and Gerard[22]. For example, the maximum shear stress at the low Reynolds number is 16% to 18% lower than the predicted maxima. In addition, the peaks in the measured distributions are shifted towards the corners. Since neither of the computed distributions allowed for the existence of secondary flows, these discrepancies can probably be attributed to the effects of secondary flows. This conclusion is supported by the work of Kogorev et al[21]. Using a method which did not allow for secondary flows, they obtained a wall shear stress distribution similar to the computed distributions discussed above. When they allowed for a secondary flow pattern which they had inferred from square duct data, the much improved prediction shown in Figure 13 was obtained. Gerard observed a similar trend in the predicted wall shear distribution for a square duct when he included secondary flow data in his finite element prediction.

5.5 Mean Axial Velocity

The mean axial velocity distribution at the test station was examined by making Pitot tube measurements at each of the grid points shown in Figure 4. The measurements were repeated for three tunnel speeds and the results converted to point velocities. The resultant velocity distributions were integrated numerically to obtain the bulk velocities and Reynolds numbers listed in Table 1.

All mean velocity calculations were based on actual properties in the tunnel and included density corrections for variations in relative humidity. No corrections were made for velocity gradient or turbulence effects although the wall proximity correction suggested by Ower and Pankhurst[29] was applied. Excluding turbulence effects, it is estimated that the calculated velocities are accurate to within ±1% while the estimated accuracy of the bulk velocity is ±2%.

The measured velocity distributions at three tunnel speeds are presented in Figures 14a, 14b, and 14c in the form of plots of constant mean velocity (isovels). Although the data in these manually prepared plots has been normalized by the bulk velocities, slight variations between the distributions at different Reynolds numbers are evident. The Reynolds number dependence is most obvious near the centre of the duct where the normalized local velocity decreases with increasing bulk velocity. At higher Reynolds numbers, the isovels also extend farther into the corners. This trend towards greater uniformity at higher Reynolds numbers is consistent with Leutheusser's[11] results for a square duct.

A particularly interesting feature of the plotted velocity distributions is the distortion of isovels due to the presence of secondary flows. The direction and magnitude of these distortions is clearly illustrated by a comparison of the experimental results in Figure 14a with Gerard's[22] predicted isovel pattern for a triangular duct without secondary flows. This comparison indicates that secondary flows in a triangular duct tend to decrease the velocity in the midwall region and increase the velocity in the corners. Similar distortions have been observed in other noncircular ducts. In the case of a square duct, Gerard[22] has confirmed that the isovels are distorted as a result of the lateral convection of axial momentum by secondary flows. Evidently, secondary flow effects must be considered if accurate predictions of mean velocity fields, wall shear stresses, and local heat transfer coefficients are desired.

The present results indicate that, in spite of the three dimensional nature of the mean velocity vector, wall similarity exists over a considerable portion of the flow in an equilateral triangular duct. This is best demonstrated by plotting velocity profiles normal to the wall in terms of the dimensionless coordinates U^+ and η. A semilogarithmic plot such as the one in Figure 15 shows that, when these coordinates are based on the local friction velocity, the data points near the wall fall on a straight line. The data in this region can be correlated by a relationship of the form:

$$U^+_{loc} = A \log \eta_{loc} + B \tag{5.2}$$

Equation 5.2 is the familiar inner law of the wall. This law is based on the hypothesis that the velocity distribution near a wall is determined solely by the wall shear stress and the density and viscosity of the fluid. As shown by previous investigations,[11,30,31] the inner law can be applied to pipe, boundary layer, and square duct flows with only slight modifications to the values of the empirical constants A and B. Reported values of the constants for several geometries are presented in Table 2 for comparison.

Table 2
Empirical Constants For Inner Law of Wall

	A	B
Pipe - Nikuradse[30]	5.75	5.5
Boundary Layer - Clauser[31]	5.6	4.9
Rectangular Duct - Leutheusser[11]	5.67	5.5

For the present case, values of A and B were determined from the high Reynolds number data. A total of 44 points from the logarithmic portion of the mean velocity distribution normal to the wall were considered. A least squares fit of this data indicated that, for turbulent flow in an equilateral triangular duct, the inner law of the wall takes the form:

$$U^{+}_{loc} = 5.69 \log \eta_{loc} + 5.08 \qquad (5.3)$$

Equation 5.3 is plotted in Figure 15 for comparison with the experimental data and Leutheusser's[11] correlation for rectangular ducts. In the midwall region, equation 5.3

accurately represents the velocity distribution up to about $\eta = 1000$. However, the extent of the logarithmic distribution is reduced considerably in the corner region where the flow is influenced by the presence of a second wall.

As shown in Figure 15, the present data deviates slightly from Leutheusser's[11] correlation for flow in a rectangular duct. However, the empirical constants in equation 5.3 are within the range observed in previous investigations of various geometries. The present data therefore lends further support to the concept of wall similarity in non-circular ducts.

Since the use of equation 5.3 requires prior knowledge of the boundary shear distribution, some of the present data was also correlated in terms of coordinates calculated from the average friction velocity. A least squares fit of the inner law to 152 data points from all Reynolds numbers resulted in the following equation:

$$U^+ = 6.31 \log \eta + 5.1 \qquad (5.4)$$

As shown in Figure 16, the mean velocity distribution near the wall and in the region $y/l \leq 0.5$ is predicted satisfactorily by equation 5.4. For values of $y/l > 0.5$ and $\eta > 500$ the measured velocity distribution departs considerably from this relationship.

5.6 Reynolds Stresses

A summary of the experimental data for the three normal Reynolds stresses, the $\overline{uw}$ and $\overline{uv}$ shear stresses, and the turbulent kinetic energy is presented in this section. In general, only the data for the lowest Reynolds number has been plotted, although all quantities were measured at three Reynolds numbers. The v', w', $\overline{uv}$, and $\overline{uw}$ data has been corrected for tangential cooling effects as suggested by Lawn[32]. All results have been normalized by the average friction velocity, u*, to facilitate comparisons with data for other duct shapes.

Due to the complexity of the anemometry system no detailed estimate of the accuracy of the data was made. However, the errors in some quantities were estimated from the variations between repeated measurements with different probes. Errors in u' could be estimated best since four separate measurements were made at each Reynolds number. At the two lower Reynolds numbers, the maximum error (20:1 odds) in the quantity u'/u^* was estimated to be $\pm 5.5\%$. Calibration drift due to probe fouling resulted in slightly higher errors at the highest Reynolds number. Some typical results have been plotted in Figure 17 to illustrate the repeatability and trend accuracies of u' measurements.

The repeatability of the measurements of transverse velocity fluctuations was not as good as that for axial velocity fluctuations. For example, variations in the average values of w'/u^* obtained in successive tests with different probes ranged from 5% to 12%. However, in the same tests, trend errors were only about $\pm$ 3%. Similar accuracies are expected for v'/u^*, although no comparative measurements were made.

The largest absolute errors occured in the shear stress measurements. In the case of $\overline{uw}$, separate measurements with the miniature and the gold plated X-probes varied by an average of 14% and 22% at Reynolds numbers of 53,000 and 81,000 respectively. However, the trends indicated by the two sets of measurements were much more consistent, and, for a given test, measurements by the single and double correlator methods generally differed by less than 10%. As a result, it was estimated that trend errors in the measurements of $\overline{uw}$ were within about $\pm$ 10%.

Measurements of $\overline{uv}$ were complicated by the fact that, over much of the flow cell, $\overline{uv}$ was extremely small. As a result, $\overline{uv}$ measurements were very sensitive to probe misalignment and wire mismatch. Measurements were particularly difficult at the higher Reynolds numbers where probe fouling was encountered. In fact, satisfactory data could only be obtained by operating the tunnel at the lowest test velocity and making rapid measurements with a new gold plated probe and the 55D70 correlator. Trends in data obtained in this manner are thought to be reliable, although the accuracy of the data has not been established quantitatively.

In general, it may be concluded that trend accuracies in the turbulence measurements are much better than the absolute accuracies of the measurements. Inaccuracies in determining the wire sensitivities and wire mismatch were considered to be the largest sources of error.

5.6.1 Normal Stresses and Mean Turbulence Kinetic Energy

Contour plots of constant u'/u^*, v'/u^*, w'/u^*, and $\overline{q}/(u^*)^2$ are presented in Figures 18 - 21. The manually prepared plots cover only one primary flow cell and generally include only the data obtained at a Reynolds number of 53,000. Contour plots of the data for the two higher Reynolds numbers are similar to those presented. It should be noted that, with the present coordinates system, distributions of v' and w' are not symmetric about the corner bisector. As a result, portions of the w'/u^* contours were omitted because of uncertainty about their shape near the bisector.

The contour plots of turbulence intensities clearly indicate the effects of convection of turbulence kinetic energy by secondary flows. As would be expected, turbulence levels are highest near the wall, where the turbulence is produced, and lowest near the duct centerline. Due to the transverse component of mean velocity, however, the low turbulence region extends far into the corner while the high turbulence region bulges outwards from the midpoint of the wall. These distortions are similar to the bulges observed in the mean velocity field although much more pronounced. The distortions in the turbulence fields are also similar to those observed in the mean turbulence kinetic energy field in a square duct[12], and they are consistent with the secondary flow pattern observed by Nikuradse[4].

Distributions of u'/u^*, v'/u^*, and w'/u^* along the midwall bisector are compared in Figure 22. In the wall region, the largest of the three components, u'/u^*, reaches values of 18% of the local velocity or 10% of the centerline velocity. Velocity fluctuations parallel to the wall generally exceed those normal to the wall, although the two components have equal magnitudes in the central region of the duct. The fact that v'/u^* and w'/u^* are equal in the central region is significant since there are no symmetry arguments to indicate that this should be so. When considered in combination with the circular shape of the contours of constant v'/u^* and w'/u^* near the duct axis, this fact indicates that there is a small core region in which the transverse velocity fluctuations are essentially independent of orientation. This result is consistent with Laufer's[9] findings in pipe flow and the measurements of Brundrett and Baine[12] in a square duct.

The distributions of turbulence intensities along normals to the wall are compared with those in a pipe and a square duct in Figures 23 - 27. In the central region, the normalized intensities of u', v', w', and $\overline{q}$ for all Reynolds numbers are generally somewhat higher than the corresponding quantities in pipe flow and lower than those for a square duct. Use of the local friction velocity as a scaling factor would reduce the differences somewhat but would not change the order in which the quantities are stacked.

For $Z/h < 0.5$ in the midwall region, the intensities of v' and w' deviate further from the corresponding distributions in pipe flow and tend towards the distributions in a square duct. Very near the wall, the distributions for the triangular duct tend towards peaks which are sharper and closer to the wall than those in pipe flow at similar Reynolds numbers. (See Figures 25 and 26). The data of Cremers and Eckert[7] indicates that similar peaks occur in the transverse velocity fluctuations in a narrow isosceles triangle. Evidently, the turbulence structure in the wall region of a triangular duct is in some way altered by the action of secondary flows.

The above comments can generally be applied to the data at all Reynolds numbers since the turbulence quantities appear to be essentially independent of Reynolds number when reduced by the average friction velocity. Laufer [9] has demonstrated that this is also the case in the central region of a circular pipe. Near the wall, however, he found marked differences in the distributions at Reynolds numbers of about 41,000 and 420,000. Since the present results only cover a Reynolds number range of 53,000 to 107,300, any similar deviations in the wall region would be proportionally smaller. If such variations were present, they are masked by the scatter in the data.

5.6.2 Reynolds Shear Stresses

The distributions of the $\overline{uv}$ and $\overline{uw}$ shear stress components were measured by two techniques, the single correlator technique and the double correlator technique. In the case of $\overline{uw}$, measurements by the two techniques were generally in good agreement. However, the single correlator method proved unsuitable for measurements of $\overline{uv}$, since the measurements often contained scatter of the same order of magnitude as the actual value of $\overline{uv}$. In view of the above, only the data which was obtained by the two correlator technique has been presented in this section. It should be noted that, although both $\overline{uv}$ and $\overline{uw}$ are presented as positive, the physical sign of $\overline{uw}$ is actually negative in the flow cell examined.

Figure 28 shows the measured distribution of the $\overline{uv}$ shear stress component at Re = 53,000. Although $\overline{uv}$ measurements were also made at the higher Reynolds numbers, the results were not considered reliable and have not been presented. The rejection of this data was largely based on the results of measurements along the Z axis where $\overline{uv}$ should vanish due to its antisymmetric distribution. For the lowest Reynolds number, the values of $\overline{uv}/(u^*)^2$ along the Z axis ranged from -0.01 to +0.02. At the higher Reynolds numbers, the measurements generally did not satisfy the requirement of zero $\overline{uv}$ shear along the wall bisector. In addition, the indicated values of $\overline{uv}$ changed significantly during the course of the tests as a result of calibration drift. Examination of the affected probes under a microscope indicated that this drift was caused by a buildup of dust on the sensing wires.

The results in Figure 28 indicate that $\overline{uv}$ is generally smallest in the midwall region and largest in the corner and along the corner bisector. This is in accordance with the predictable behaviour based on the $\overline{U}$ distribution in Figure 14a if it is assumed that $\overline{uv}$ is associated with $\partial\overline{U}/\partial y$ gradients. The main exception to this trend occured in the region very near the wall, $Z=0$, where $\partial\overline{U}/\partial y$ was very small but relatively large values of $\overline{uv}$ were indicated. Measurements in this region were probably influenced by the presence of large velocity and turbulence gradients and have not been included in Figure 28.

One particularly interesting feature of the $\overline{uv}$ distribution is the region of negative $\overline{uv}$ straddling the wall bisector. The validity of these negative values may at first appear questionable since they are only of the order of magnitude of the deviations from zero shear on the Z axis. However, a similar change in sign was noted in almost every attempt to measure the $\overline{uv}$ distribution. In addition, Brundrett and Baine(12) observed that the corresponding stress in square duct flow changes sign within a flow cell. It would therefore appear that the indicated sign reversal in Figure 28 is real and is a phenomena associated with flows in noncircular ducts.

Contour plots of the $\overline{uw}$ distributions at two Reynolds numbers are compared in Figure 29. The distributions are very similar. As expected, $\overline{uw}$ is a maximum near the wall and a minimum at the center of the duct. Gradients of $\overline{uw}$ along normals to the wall are much steeper in the corner than in the midwall region. This is clearly illustrated in Figure 30 where distributions of $\overline{uw}$ along normals to the wall have been plotted. The results in Figure 30 also indicate that, in the corner region, the maximum values of $\overline{uw}$ represent significantly larger portions of the local wall shear stress than in the midwall region. Along the Z - axis, the maximum value of $\overline{uw}$ is only about 80% of the local wall shear stress. For a similar Reynolds number in pipe flow, the corresponding turbulence stress attains a value equalling 90% of the wall shear stress.

As mentioned in Section 3.1, the axial momentum equation for triangular duct flows cannot be simplified and integrated to give a theoretical distribution of $\overline{uw}$ similar to that for pipe flow. However, some useful information can be obtained by examining the simplified form of the momentum equation along the line y/l=0. Away from the wall, this equation reduces to equation 3.13 which is repeated here for convenience

$$\frac{1}{\rho}\frac{\partial \overline{P}}{\partial x} = - \overline{W}\frac{\partial \overline{U}}{\partial z} - \left(\frac{\partial \overline{uv}}{\partial y} + \frac{\partial \overline{uw}}{\partial z}\right) \qquad (3.13)$$

In pipe flow, only the terms corresponding to the first and last terms in equation 3.13 are nonzero, and the axial momentum equation can be directly integrated to give a theoretical distribution for the $\overline{uw}$ shear stress.

For discussion's sake, a hypothetical $\overline{uw}$ distribution was calculated by assuming that simplifications similar to those for pipe flow could be made along the bisectors of the walls of an equilateral triangular duct. The hypothetical distribution was obtained by direct integration of the first and last terms in equation 3.13 and is given by :

$$\overline{uw} = \frac{1}{\rho}\frac{\partial \overline{P}}{\partial x}(h-z)$$

or

$$\frac{\overline{uw}}{(u^*)^2} = \frac{4}{D_h}(h-z) \qquad (5.5)$$

The above $\overline{uw}$ distribution is compared with $\overline{uw}$ measurements for three tunnel speeds in Figure 31. In the wall region, the viscous stress for a Reynolds number of 53,000 is also shown. The large differences between the hypothetical and measured distributions indicate that the terms omitted in obtaining equation 5.5 make an important contribution to the axial momentum balance at all points along the wall bisector.

In order to illustrate more clearly the relative importance of the various terms in equation 3.13, a point by point momentum balance was carried out along the line $y/l=0$. All terms except $\overline{W}\,\partial\overline{U}/\partial z$ were calculated from experimental data. The value of $\overline{W}\,\partial\overline{U}/\partial z$ was obtained by treating it as a closure term. In the wall region, the viscous term, $\nu\partial^2\overline{U}/\partial z^2$, was also considered. Its magnitude was calculated from the inner law of the wall.

Calculated distributions of the momentum balance terms at Re = 53,000 are shown in Figure 32. These results show that, in the central region of the duct, the $\overline{uw}$ shear stress gradient is the predominant term. The gradient of $\overline{uv}$ also makes a significant contribution in this region. Very near the wall, the axial pressure drop contribution is balanced by viscous forces. Between these two regions, the overall momentum balance is dominated by the convection of axial momentum by a secondary flow normal to the wall. This phenomena evidently accounts for the apparent discrepancy between the values of the local wall shear stress and the $\overline{uw}$ shear stress in the midwall region.

5.7 Axial Turbulence Power Spectra

Axial turbulence power spectra at the duct centerline and at points along the wall and corner bisectors were measured at each Reynolds number. The results for Reynolds numbers of 53,000 and 107,300 are presented in Figures 33 and 34 respectively. Each of the spectra has been scaled to make the area under the curves equal to the total value of u'^2 in the frequency range investigated. When scaled in this manner, the spectra for the triangular test section exhibit the same general shape as the corresponding spectra for flow in pipes and in the wall region of turbulent boundary layers. In the spectra for the triangular duct, the largest contribution to the total energy is made by velocity fluctuations with frequencies of less than 100 hz. The portion of the total energy contributed by these relatively low frequency fluctuations is greatest in the wall region where production occurs.

As illustrated in Figures 33 and 34, the high frequency portions of the present spectra tend toward the n^{-7} slope associated with turbulence dissipation. None of the spectra exhibited the extended region of -5/3 slope which has been observed in both pipe and boundary layer flows and which is frequently referred to as the nonviscous subrange. The absence of this region can probably be explained by the fact that the present data was obtained at relatively low Reynolds numbers.

5.8 Secondary Velocities

The present work included direct measurements of $\overline{V}$ by the X-probe technique outlined in Appendix B. The problems of wire mismatch and drift normally associated with this method were minimized by taking advantage of the anti-symmetric distribution of $\overline{V}$. (See Appendix B). Results for Re=53,000 are presented in Figure 35 in the form of velocity profiles along normals to the wall. The individual data points for Re=107,300 are presented for comparison. Both sets of data have been normalized by u^*.

From the results presented in Figure 35, it is evident that the secondary flow patterns indicated by Nikuradse's[4] flow visualization tests are indeed correct. As suggested previously, these secondary flow patterns can be subdivided into the six primary flow cells illustrated in Figure 3. In each of these cells, a secondary current is directed from the center of the duct to the corner via the corner bisector. The continuity requirement for the cell is met by a return flow along the wall and the wall bisector. The horizontal component of this flow, $\overline{V}$, reaches a maximum value of 1.5% of U_b near the wall in the corner region.

In accordance with the findings of Launder and Ying[14], the secondary velocities over most of the cross-section are practically independent of Reynolds number when reduced by u^*. For the present results, an apparent exception to this rule occured in the corner where the $\overline{V}$ profiles appeared to vary with changes in the Reynolds number. These variations were probably due to experimental error since they did not exhibit a systematic trend with respect to Reynolds number.

Due to the complexity of the X-probe technique for measuring secondary velocities, a detailed assessment of the errors in the present data was not possible. However, a crude estimate of the accuracy was obtained by applying the requirements of mass conservation to individual velocity profiles within flow cell boundaries. Integration of the velocity profiles in the midwall region indicated that flows into and away from the corner differed by less than 15%. This compares favourably with the 20% discrepancy which Gessner and Jones[(13)] observed in data obtained with a single rotatable wire. Unfortunately, the accuracy of velocity profiles near the corner of the triangular duct could not be checked because of a lack of data near the wall.

The applicability of the X-probe technique for measuring secondary velocities is limited, in practice, to components of secondary velocity which have an antisymmetric distribution. In the present test section, only $\overline{V}$ qualifies in this respect. However, it was possible to obtain estimates of the $\overline{W}$ distribution along the z axis by two indirect methods.

The first indirect method involved a simple calculation of $\overline{W}$ from the measured distribution of $\overline{U}$ and the calculated distribution of $\overline{W}\, \partial\overline{U}/\partial z$. The latter quantity was the closure term in the momentum balance calculation discussed in section 5.6.

The second method for estimating $\overline{W}$ is based on the mean flow continuity equation for fully developed flow which is given in equation 3.1. By rearranging this equation and integrating along the z axis, the following expression for $\overline{W}$ can be obtained:

$$\overline{W} = - \int_0^z \left(\frac{\partial \overline{V}}{\partial y}\right)_{y=0} dz \qquad (5.6)$$

For the present case, the required distribution of $\partial\overline{V}/\partial y$ was obtained from the direct measurements of $\overline{V}$. The gradient was obtained by assuming that the distribution of $\overline{V}$ between y/l=0 and y/l=0.12 was linear. Although this was a rather crude approximation, the quantity and accuracy of $\overline{V}$ data did not warrant a more sophisticated treatment.

The distributions of $\overline{W}$ calculated by the above methods are presented in Figure 36. Results from the two methods are in good agreement. Both indicate that secondary currents in the midwall region are directed toward the center of the duct. As the flow leaves the wall region its strength increases rapidly to a maximum value of about $\overline{V}/U_b = 0.6\%$ at $z/h = 0.35$. It then decreases to a value of $\overline{V}/U_b = 0$ by $z/h = 0.75$. As shown in Figure 36, this pattern is very similar to the observed distribution for the corresponding component of secondary velocity in a square duct[12]. In a square duct, however, the maximum value of the secondary velocity along the midwall bisector is about twice that in a triangular duct.

In the central region of the triangular duct, a secondary flow towards the wall is indicated by the results in Figure 36. This implies that two directions of circulation exist within each primary flow cell. Since all other evidence points to a single direction of rotation, it is very probable that the negative values of $\overline{W}$ are the result of the large errors inherent in the indirect methods for calculating $\overline{W}$.

6.0 CONCLUDING REMARKS

The following conclusions are based on the above results and are applicable to fully developed turbulent flows in equilateral triangular ducts for Reynolds numbers in the range of 5×10^4 to 1.1×10^5.

a) The friction factor is 5% to 6.5% lower than that predicted by the Blasius equation. The "Universal Criterion Relationship" proposed by Malak et al[26] provides a satisfactory correlation of the present friction factor data.

b) The wall shear stress distribution is sensibly independent of Reynolds number when normalized by the average surface shear stress. Due to momentum transport by secondary flows, the wall shear stress over the central half of each wall is constant to within a few percent.

c) The mean velocity distribution in the wall region can be described by the inner law of the wall if u^+ and η are based on local valves of the wall shear stress.

d) The mean velocity and turbulence fields are clearly influenced by the presence of secondary flows. Differences between the measured mean velocity distribution and Gerard's[22] predicted isovel pattern are mainly due to the neglect of secondary flow effects in Gerard's analysis. Secondary flows influence the turbulence kinetic energy distribution more than the mean velocity distribution.

e) The normal Reynolds stress distributions are essentially independent of Reynolds number when normalized by the average friction velocity.

f) The secondary flow pattern observed by Nikuradse was confirmed by direct measurements of $\overline{V}$. The actual pattern consists of six counterotating flow cells in which the flow is directed from the centre of the duct to the corner via the corner bisector. The return flow is along the wall and the wall bisector. The $\overline{V}$ component of the secondary velocity has a maximum strength of about 1.5% of U_b in the return flow along the wall.

The present work indicates that secondary flows have an important influence on the distributions of both mean flow and turbulence quantities in triangular duct flows. The secondary flow effects arise from the lateral convection of momentum and energy by the helical flow. This mechanism must be considered if the flow is to be effectively modelled. It is therefore suggested that, as the next phase of the work, both components of secondary velocity be measured. The proposed measurements could be made by using a single rotatable slanted wire in conjunction with the equations derived in Appendix B.

Future work should also be directed at the application of a technique such as the Gosman[33] finite difference method to the prediction of secondary flows from turbulence data. This is an important step in the development of techniques for the prediction of flow and heat transfer characteristics in noncircular ducts from measured or modelled turbulence data. The successful development of such techniques would undoubtedly be of great benefit in the analysis of heat transfer in noncircular geometries such as nuclear fuel bundles and should be considered the ultimate goal of future research.

7.0 ACKNOWLEDGEMENTS

The funding for the present research was provided by the National Research Council through Grant No. A8921 and their support is gratefully acknowledged. The author also acknowledges with appreciation the guidance and helpful advice given by Dr. A. C. Trupp and the assistance provided by other staff and students in the Mechanical Engineering Department.

8.0 REFERENCES

1. B. Kjellstrom and A. Stenback: "Pressure Drop, Velocity Distributions and Turbulence Distributions For Flow in Rod Bundles", AB Atomenergi, Sweden, Rep. AE-RV-145, (RL-1236), 1970.

2. C. Hall and P. J. Svenningsson: "Secondary Flow Velocities in a Rod Bundle of Triangular Array", AB Atomenergi, Sweden, Rep. AE-RL-1326, 1971.

3. A. C. Trupp and R. S. Azad, "The Structure of Turbulent Flow in Triangular Array Rod Bundles", Nuclear Engineering and Design, Volume 23, No. 1, pp. 47-84, April 1975.

4. J. Nikuradse: "Untersuchungen über turbulente Strömungen in nicht Kreisförmigen Rohren", Ingenieur - Archiv I, pp. 306-332, 1930.

5. J. Nikuradse: "Untersuchungen über die Geschwindigkeitsverteilung in turbulenten Strömungen", Diss. Gottingen 1926, VDI-Forschungsheft 281 (1926).

6. L. Prandtl: "Über den Reibungswiderstand Strömender luft", Ergeb. Aerodyn. Versuch., Gottingen, III series.

7. C. J. Cremers and E. R. G. Eckert: "Hot Wire Measurements of Turbulence Correlations in a Triangular Duct", Trans. ASME, 84E, J. Appl. Mech., 4, pp. 609-614, Dec. 1962.

8. P. C. Bandopadhayoy and J. B. Hinwood: "On the Coexistence of Laminar and Turbulent Flow in a Narrow Triangular Duct", J. Fluid Mech., Vol. 59, Part 4, pp. 775-783, 1973.

9. J. Laufer: "The Structure of Turbulence in Fully Developed Pipe Flow", NACA Rep. 1174, 1954.

10. L. C. Hoagland: "Fully Developed Turbulent Flow in Straight Rectangular Ducts - Secondary Flow, Its Cause and Effect on the Primary Flow", Ph.D. Thesis, Massachusetts Institute of Technology, 1960.

11. H. J. Leutheusser: "Turbulent Flow in Triangular Ducts", Journal of the Hydraulics Division, ASCE, Vol. 89, No. HY3, Proc. Paper 3508, pp. 1-19, May,1963.

12. E. Brundrett and W. D. Baines: "The Production and Diffusion of Vorticity in Duct Flow", J. Fluid Mech., Vol. 19, pp. 375-394, 1964.

13. F. B. Gessner and J. B. Jones: "On Some Aspects of Fully-Developed Turbulent Flow in Rectangular Channels", J. Fluid Mech., Vol. 23, Part 4, pp. 689-713, 1965.

14. B. F. Launder and W. M. Ying: "Secondary Flows in Ducts of Square Cross-Section", J. Fluid Mech., Vol. 54, Part 2, pp. 289-295, 1972.

15. F. B. Gessner: "The Origin of Secondary Flow in Turbulent Flow Along a Corner", J. Fluid Mech., Vol. 58, Part 1, pp. 1-25, 1973.

16. J. A. Liggett, Chao-Ling Chiu, and Ling S. Miao: "Secondary Currents in a Corner", Journal of the Hydraulics Division, ASCE, Vol. 91, No. HY6, pp. 99-117, November, 1965.

17. H. J. Tracey: "Turbulent Flow in a Three-Dimensional Channel", Journal of the Hydraulics Division, ASCE, Vol. 91, No. HY6, pp. 9-35, November, 1965.

18. S. C. Kacker: "Some Aspects of Fully-Developed Turbulent Flow in Non-Circular Ducts", J. Fluid Mech., Vol. 57, Part 3, pp. 583-602, 1973.

19. J. O. Hinze: "Experimental Investigation on Secondary Currents in the Turbulent Flow Through a Straight Conduit", Appl. Sci. Res., Vol. 28, No. 6, pp. 453-465, December, 1973.

20. R. G. Deissler and M. F. Taylor: "Analysis of Turbulent Flow and Heat Transfer in Non-circular Passages", Technical Report R-31, NASA, 1959.

21. L. S. Kogorev, A. S. Korsun, B. N. Kostyunin, V. I. Petrovichev, and R. L. Struenze: "Effect of Secondary Flows on the Velocity Distribution and Hydraulic Drag in Turbulent Liquid Flows in Non-circular Channels", Heat Transfer-Soviet Research, Vol. 3, No. 1, pp. 66-78, January - February, 1971.

22. R. Gerard: "Finite Element Solution for Flow in Non-circular Conduits", Journal of the Hydraulics Division, ASCE, Vol. 100, No. HY3, pp. 425-441, March, 1974.

23. DISA Probe Manual, DISA Elektronik A/S, Herlev, Denmark.

24. DISA Random Signal Indicator and Correlator Type 55A06 - Description and Operating Instructions, DISA Elektronik A/S, Herlev, Denmark.

25. C. W. Carlson and T. F. Irvine, Jr.: "Fully Developed Pressure Drop in Triangular Shaped Ducts", Trans. ASME, J. Heat Trans., 83, pp. 441-444, November, 1961.

26. J. Malák, J. Hejna and J. Schmid: "Pressure Losses and Heat Transfer in Non-Circular Channels with Hydraulically Smooth Walls", Int. J. Heat Mass Transfer, Vol. 18, pp. 139-149, 1975.

27. J. H. Preston: "The Determination of the Local Skin Friction by Means of Surface Pitot Tube", Journal of the Royal Aeronautical Society, Vol. 58, pp. 109-121, 1954.

28. V. C. Patel: "Calibration of the Preston Tube and Limitations on Its Use in Pressure Gradients", J. Fluid Mech., Vol. 23, pp. 185-208, 1965.

29. F. Ower and R. C. Pankhurst: "The Measurement of Air Flow", Pergamon Press, 1966.

30. J. Nikuradse: "Gesetzmaessigkeiten der turbulenten Strömung in glatten Rohren", VDI-Forschungsheft No. 356, 1932.

31. F. H. Clauser: "The Turbulent Boundary Layer", Advances in Applied Mechanics, Vol. 4, 1956.

32. C. J. Lawn: "Turbulence Measurements with Hot Wires at B.N.L.", Central Elec. Gen. Board, Berkley Nuclear Labs. Rep. RD/B/M 1277, April, 1969.

33. A. D. Gosman, W. M. Pun, A. K. Runchal, D. B. Spalding, and M. Wolfshtein: "Heat and Mass Transfer in Recirculating Flows", Academic Press, 1969.

APPENDIX A

Friction Velocity and Reynolds Number Corrections

Tunnel operating conditions for successive tests at the same Reynolds number were matched on the basis of the axial pressure drop in the duct. For each test at a given Reynolds number, the fan speed and damper settings were adjusted to obtain the same pressure drop over the last 62 hydraulic diameters of the test section. Slight variations in the settings were required due to daily variations in atmospheric conditions.

Tunnel conditions in tests with equal pressure drops were related by first assuming a Reynolds number dependence of the friction factor of the form:

$$f = C/(Re)^{1/4} \qquad (1A)$$

Since flow in the last 60 hydraulic diameters of the test section was essentially fully developed it follows that:

$$\frac{d\overline{P}}{dx} = \frac{f_i}{2D_h} \rho_i U_{b,i}^{2} = \frac{C}{2(D_h)^{5/4}} \rho_i^{3/4} \mu_i^{1/4} U_{b,i}^{7/4} \qquad (2A)$$

where the subscript i denotes conditions for the i^{th} test. Since the Reynolds numbers of the mean velocity-pressure drop tests were known, the tunnel conditions for these tests were selected as reference conditions. Denoting the reference conditions by the subscript o and equating pressure drops, equation 2A gives the following relationship:

$$\rho_o^{3/4}\ \mu_o^{1/4} U_{b,o}^{7/4} = \rho_i^{3/4} \mu_i^{1/4} U_{b,i}^{7/4} \qquad (3A)$$

Rearranging 3A, the following expression for the Reynolds number of the i^{th} test is obtained:

$$Re_i = Re_o \ \left(\frac{\rho_i}{\rho_o}\right)^{4/7} \ \left(\frac{\mu_o}{\mu_i}\right)^{8/7} \qquad (4A)$$

Equation 3A can also be rearranged to relate bulk velocities as follows:

$$U_{b,i} = U_{b,o} \ \left(\frac{\rho_o}{\rho_i}\right)^{3/7} \ \left(\frac{\mu_o}{\mu_i}\right)^{1/7} \qquad (5A)$$

Average friction velocities for two matched tests can also be related. By definition:

$$u* = \sqrt{\frac{\tau_w}{\rho}} \ \alpha \ \sqrt{\frac{(d\bar{P}/dx)}{\rho}} \ \alpha \ \sqrt{f\ U_b^{\ 2}} \qquad (6A)$$

Substituting equation 1A for the friction factor, equation 6A can be rewritten:

$$u* \ \alpha \ U_b^{7/8} \left(\frac{\mu}{\rho}\right)^{1/8} \qquad (7A)$$

For two matched tests it follows that:

$$u^*_i = u^*_o \left(\frac{\rho_o}{\rho_i}\right)^{1/8} \left(\frac{\mu_i}{\mu_o}\right)^{1/8} \left(\frac{U_{b,i}}{U_{b,o}}\right)^{7/8} \qquad (8A)$$

Reference values of the friction velocity were calculated from least squares fits of data from the axial pressure drop tests.

APPENDIX B

Equations for Direct Measurement of Secondary Velocities with an X-Probe

The mean effective cooling velocity on a slanted wire parallel to the duct base will contain a component of the secondary velocity in the y direction. For an X-probe with wires slanted at plus and minus 45° to the duct axis, the secondary flow component will increase the cooling effect on one wire and lower the heat transfer rate from the other. The equations for the mean effective cooling velocities of the two wires in an X-probe can therefore be written:

$$(\overline{U}_{eff})^2_{I} = (\overline{U}\cos 45 + \overline{V}\sin 45)^2 + k_1^2 (\overline{U}\sin 45 - \overline{V}\cos 45)^2 = \frac{1}{2}(\overline{U}^2 + 2\overline{U}\overline{V} + \overline{V}^2) + \frac{k_1^2}{2}(\overline{U}^2 - 2\overline{U}\,\overline{V} + \overline{V}^2) \tag{1B}$$

$$(\overline{U}_{eff})^2_{II} = (\overline{U}\cos 45 - \overline{V}\sin 45)^2 + k_1^2 (\overline{U}\sin 45 + \overline{V}\cos 45)^2 = \frac{1}{2}(\overline{U}^2 - 2\overline{U}\,\overline{V} + \overline{V}^2) + \frac{k_1^2}{2}(\overline{U}^2 + 2\overline{U}\,\overline{V} + \overline{V}^2) \tag{2B}$$

where $k_1 = 0.23$ for DISA probes.

For a constant temperature linearized system the mean effective cooling velocities are related to the output voltage by the following relationships:

$$E_I = S_I \ (\bar{U}_{eff})_I \tag{3B}$$

$$E_{II} = S_{II} \ (\bar{U}_{eff})_{II} \tag{4B}$$

where $S_I = S_{II}$ if the wires are matched. Applying these relationships to the difference between equations 1B and 2B and neglecting terms containing $\bar{V}^2$, the following expression can be obtained:

$$E_I^{\,2} - E_{II}^{\,2} = \frac{S_I^{\,2}}{2} \left[(\bar{U}^2 + 2\bar{U}\bar{V} + \bar{V}^2) + k_1^{\,2} (\bar{U}^2 - 2\,\bar{U}\bar{V} + \bar{V}^2) \right]$$

$$- \frac{S_{II}^{\,2}}{2} \left[(\bar{U}^2 - 2\,\bar{U}\bar{V} + \bar{V}^2) + k_1^{\,2} \ (\bar{U}^2 + 2\,\bar{U}\bar{V} + \bar{V}^2) \right]$$

$$= 2\,S_I^{\,2} \ (1 - k_1^{\,2}) \ \bar{U}\ \bar{V} \tag{5B}$$

If the probe is calibrated at the centre of the duct where $\bar{V} = 0$, equations 1B and 2B can be combined with equations 3B and 4B and reduced to the form:

$$E = (S/\sqrt{2}) \ (1 + k_i^{\,2})^{1/2} \ \ \bar{U} \tag{6B}$$

This equation can also be applied at points where $\overline{V}$ is finite if the average voltage from the two wires, $(E_I + E_{II})/2$, is used. An expression for the horizontal component of the secondary velocity can therefore be obtained by solving 6B for S, substituting for S in 5B, and rearranging to give:

$$\overline{V} = \overline{U}\,\frac{1 + k_1^{\,2}}{1 - k_1^{\,2}}\;\frac{E_I^{\,2} - E_{II}^{\,2}}{(E_I + E_{II})^2} \qquad (7B)$$

where $\overline{U}$ is the local value of the axial velocity.

Equation 7B indicates that the secondary flow velocity, $\overline{V}$, is proportional to the difference of the squares of the mean voltage outputs from an X-probe when the wires are parallel to the base. Similar expressions can be obtained for any probe orientation and, in theory, any velocity component can be obtained by a single point measurement with an X-probe.

In practice, the applicability of the point measurement technique is limited by its sensitivity to transverse velocity gradients and wire mismatch. However, a slightly modified technique can be applied to give reliable measurements of velocity components with antisymmetric distributions. This technique requires that separate point measurements be made at symmetric points on opposite sides of the flow cell boundary which is normal to the velocity component desired. In the case of $\overline{V}$, for example, the mean voltage outputs of the two wires would be recorded at symmetric points on opposite sides of the z axis. If $\overline{V}$ is perfectly symmetric, the two output voltages for each wire will be related to the secondary velocity by equation 7B. As a result, separate estimates of $\overline{V}$ can be made for each wire, thereby eliminating the problems of wire mismatch and transverse velocity gradients. Furthermore, it can be shown that the effects of small positioning errors and asymmetries in the axial velocity distribution can be minimized by combining the point measurements in an equation of the form:

$$|\overline{V}| = \left| 4\,\overline{U}\ \frac{1 + k_1^{\,2}}{1 - k_1^{\,2}}\ \frac{(E_{I,a} + E_{II,b})^2 - (E_{II,a} + E_{I,b})^2}{(E_{I,a} + E_{I,b} + E_{II,a} + E_{II,b})^2} \right|$$

The subscrips a and b identify measurements made on different sides of the symmetry line. The physical sign of the secondary velocity component can be determined from the relative magnitudes of the mean voltage outputs by inspection.

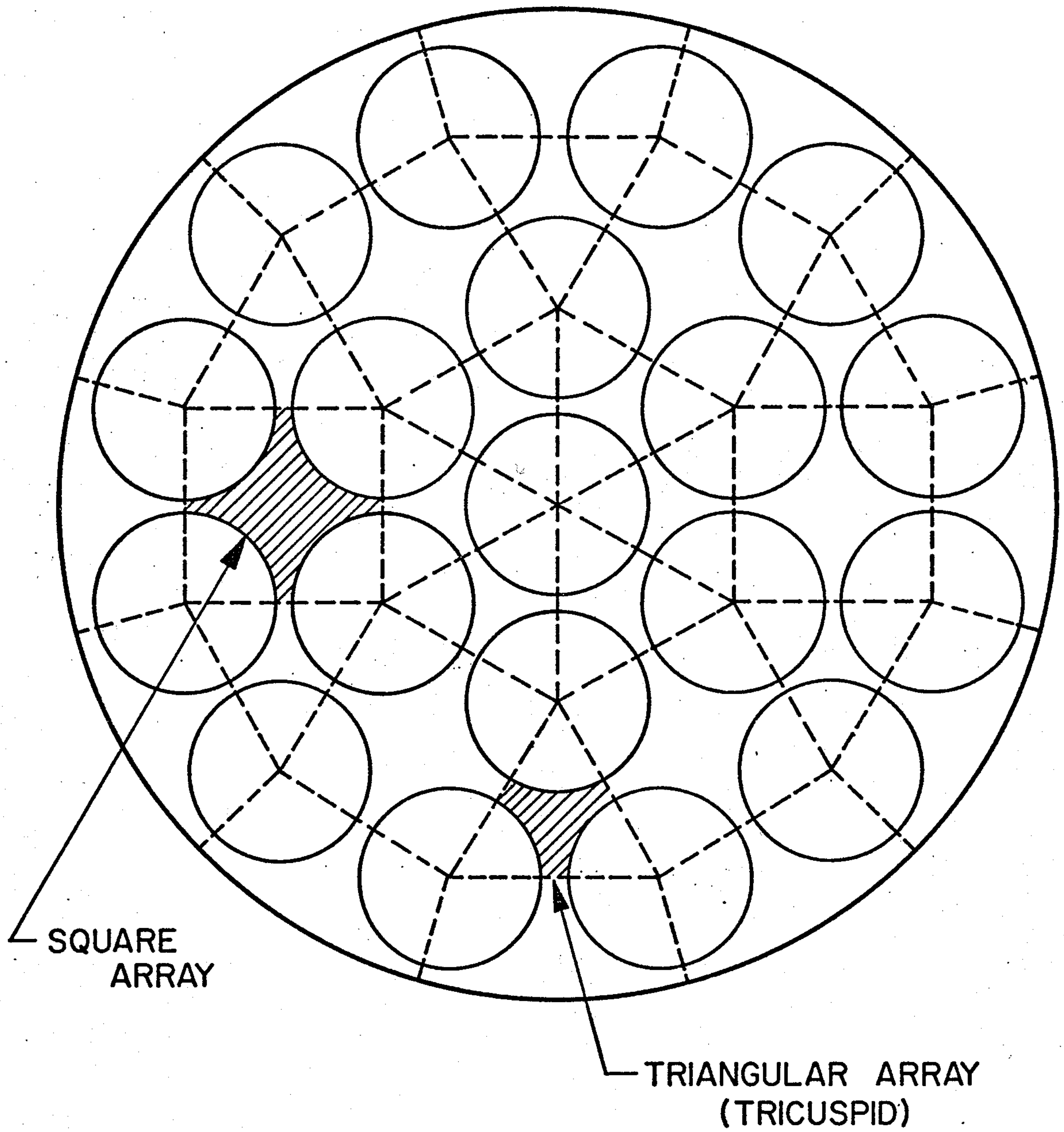

IG. I. CROSS—SECTION of TYPICAL NINETEEN ELEMENT FUEL BUNDLE.

1. Duct
2. Nozzle
3. Canvas Couplings
4. Damper
5. Fan Section
6. Silencer
7. Diffuser
8. Corner with Turning Vanes
9. Diffuser
10. Corner with Turning Vanes
11. Transition
12. Screen Section
13. Contraction Cone
14. Transition
15. Transition
16. Transition
17. Wooden Entrance Section
18. Plexiglass Test Section
19. Test Station

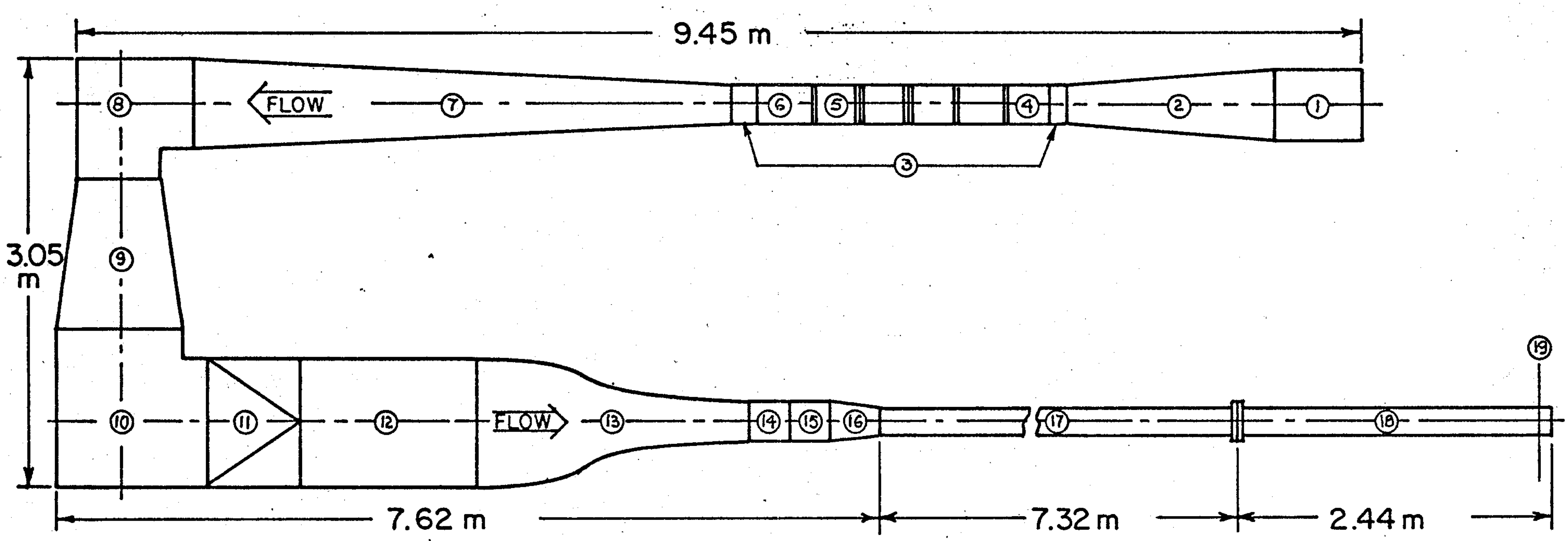

Fig. 2. Plan View of Wind Tunnel for Triangular Duct Turbulence Studies.

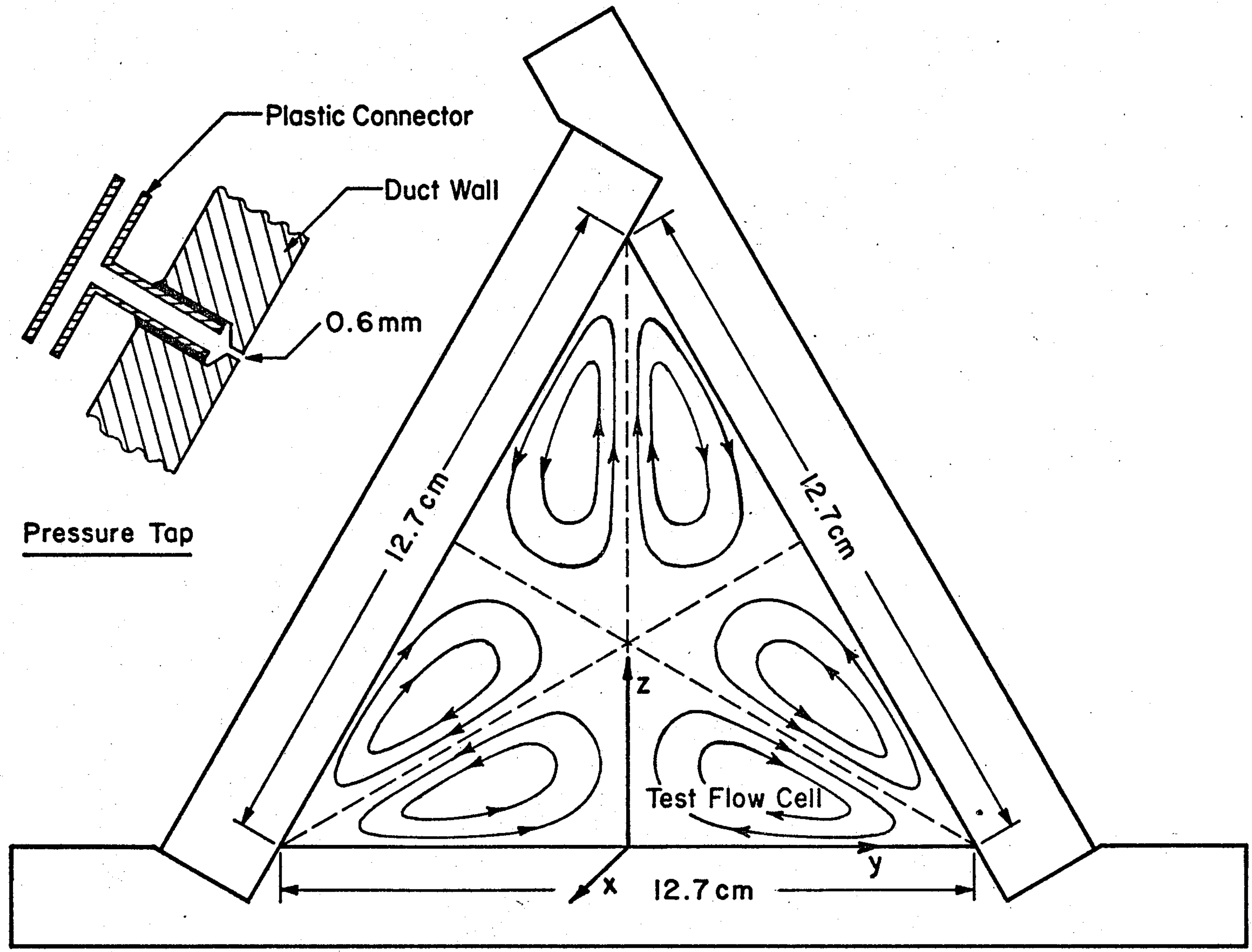

Fig. 3. Cross-Section of Equilateral Triangular Test Section.

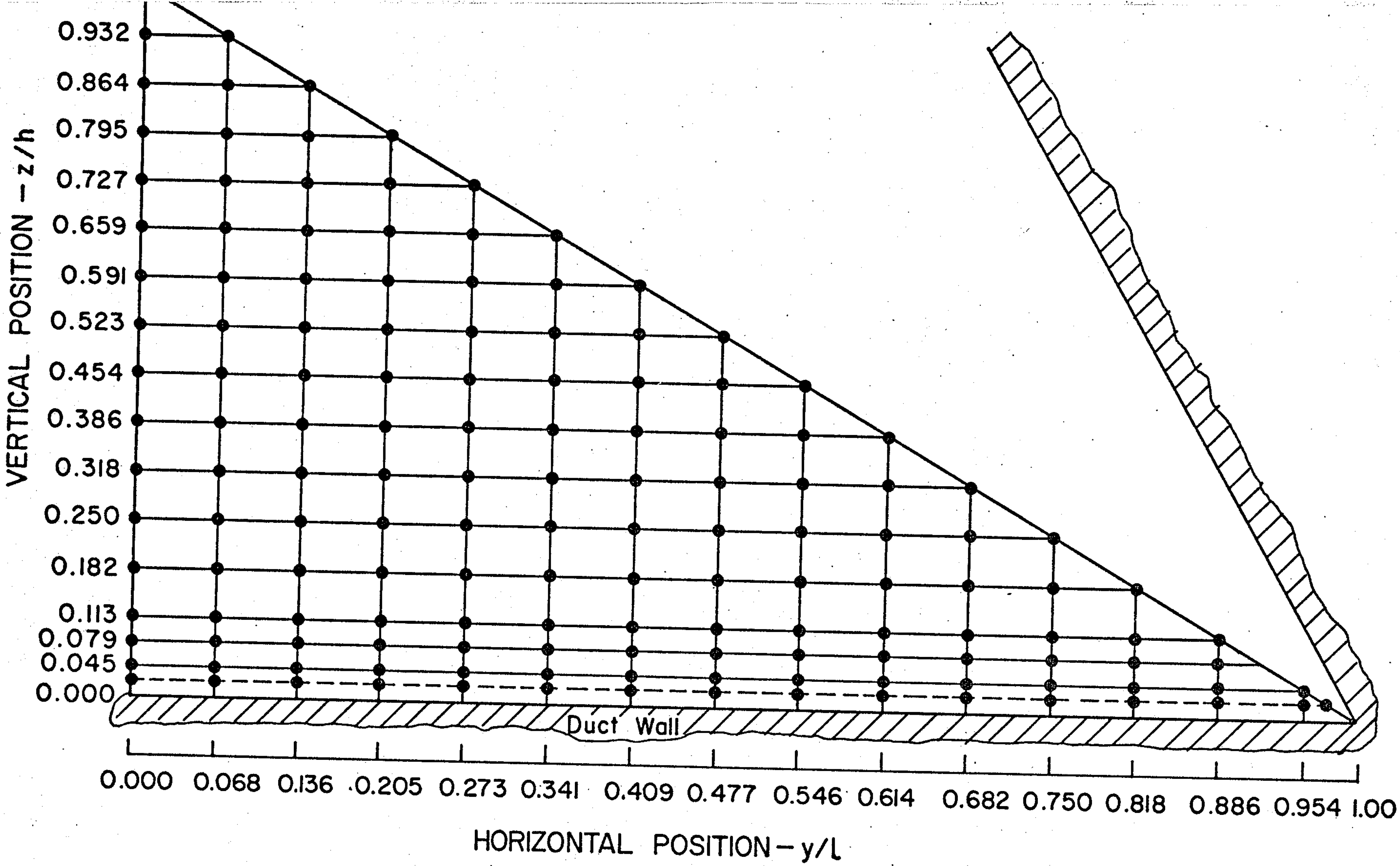

Figure 4. Primary Flow Cell Sub-Division for Measurements.

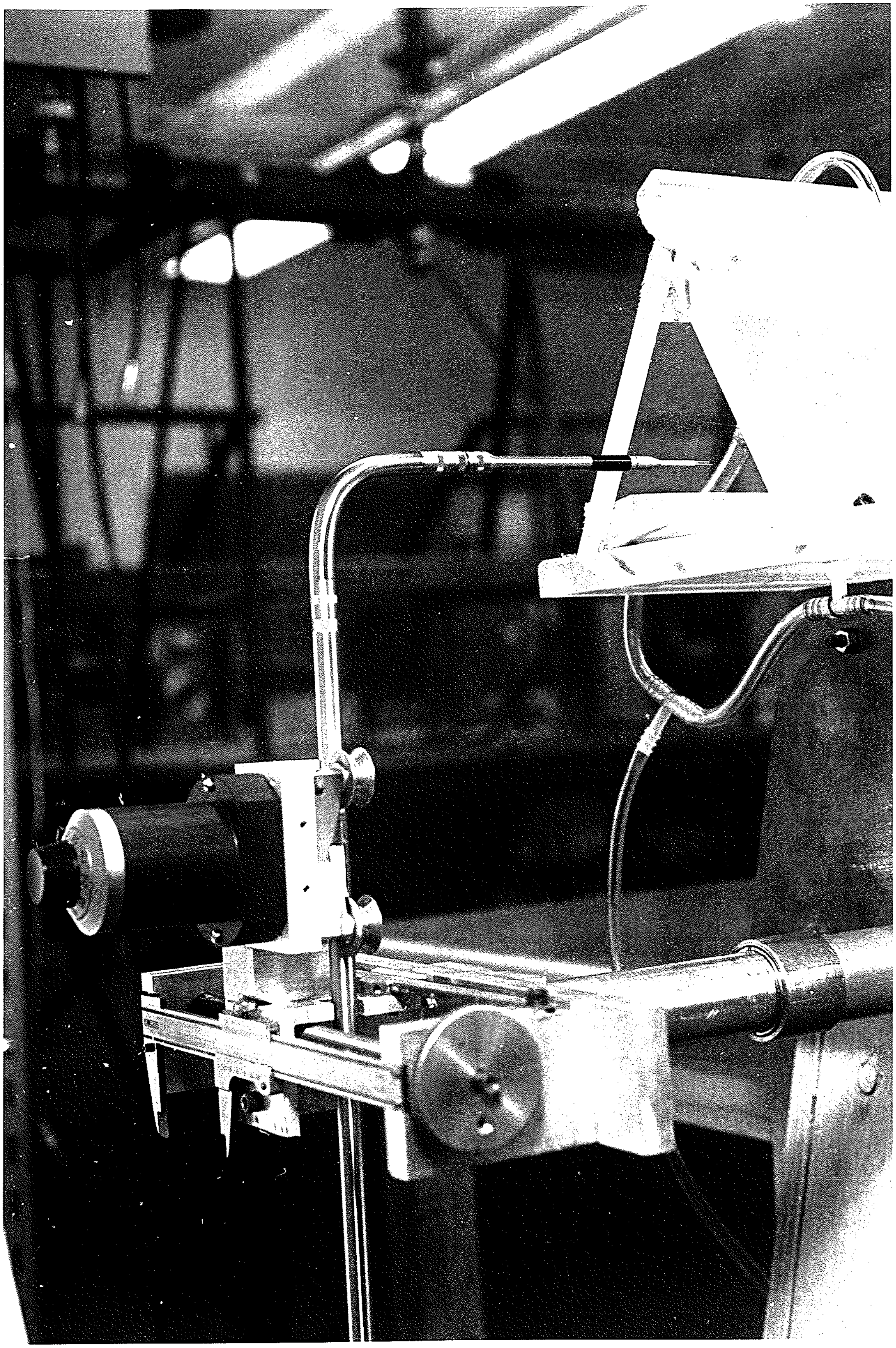

Fig. 5. Traversing Mechanism with X-probe.

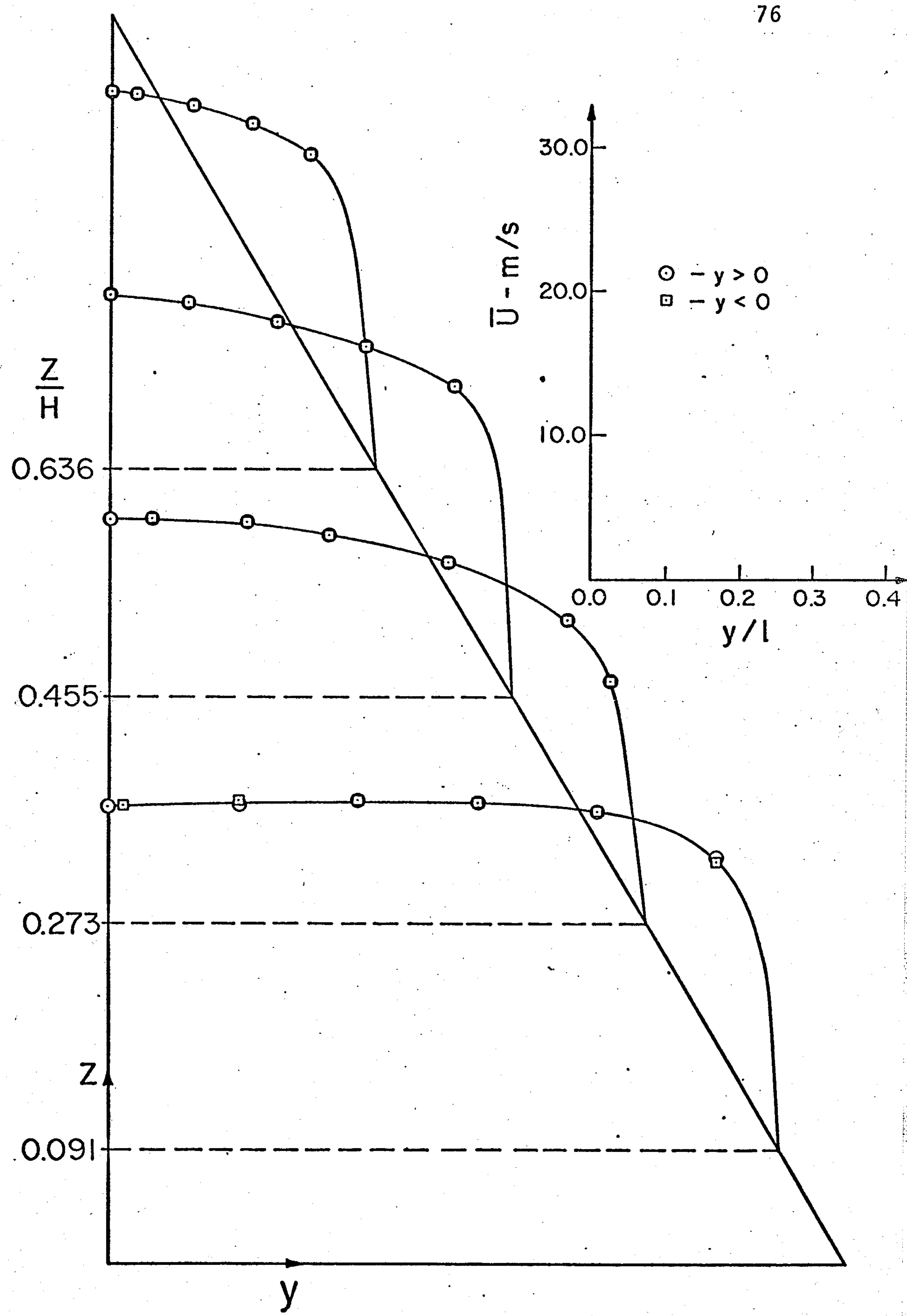

Fig. 6. Comparison of Mean Velocity Profiles from Opposite Halves of Triangular Duct. Re = 107,300.

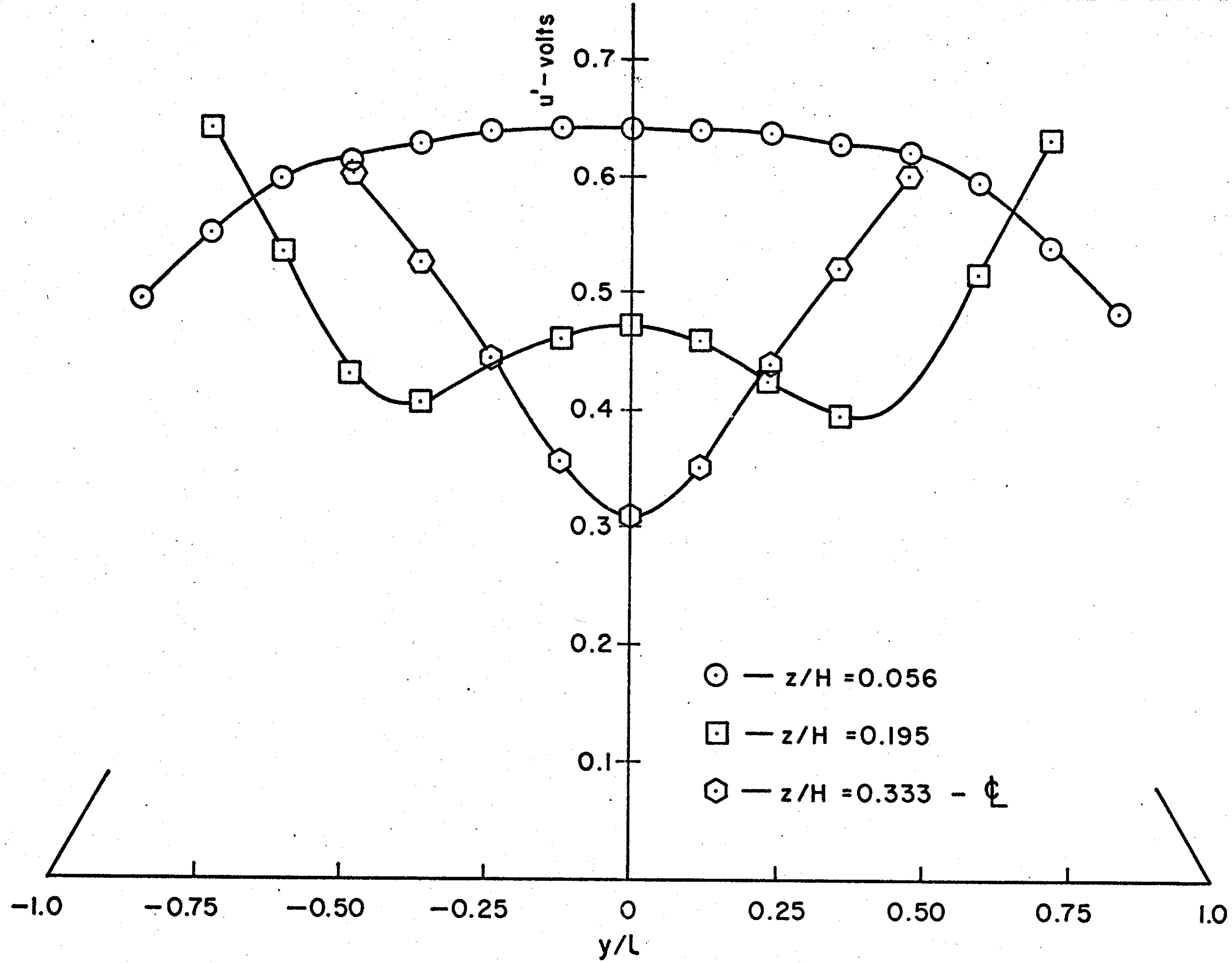

Figure 7. Distribution of u' Along Horizontal Traverses in Triangular Duct.

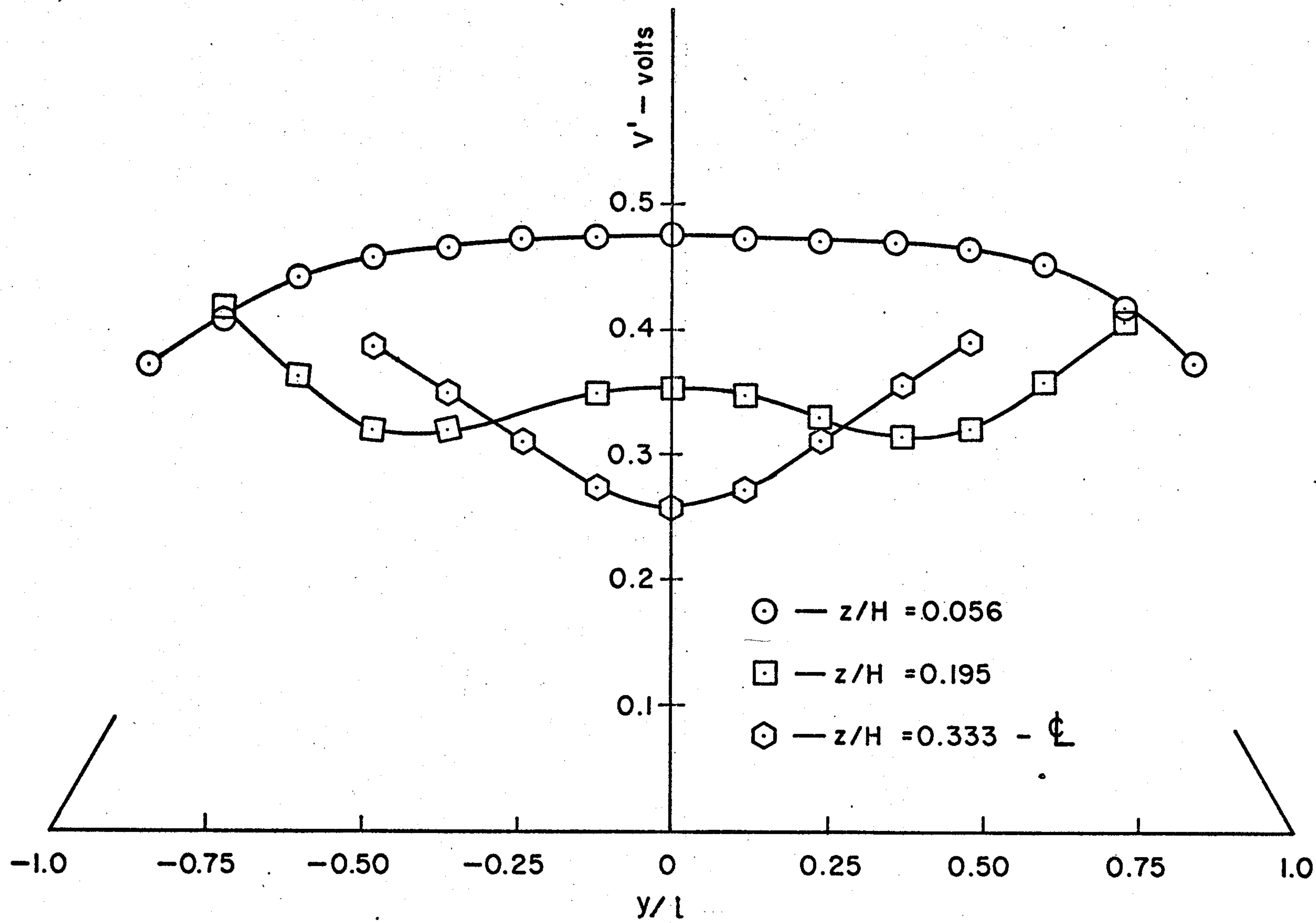

Figure 8. Distribution of v' Along Horizontal Traverses in Triangular Duct.

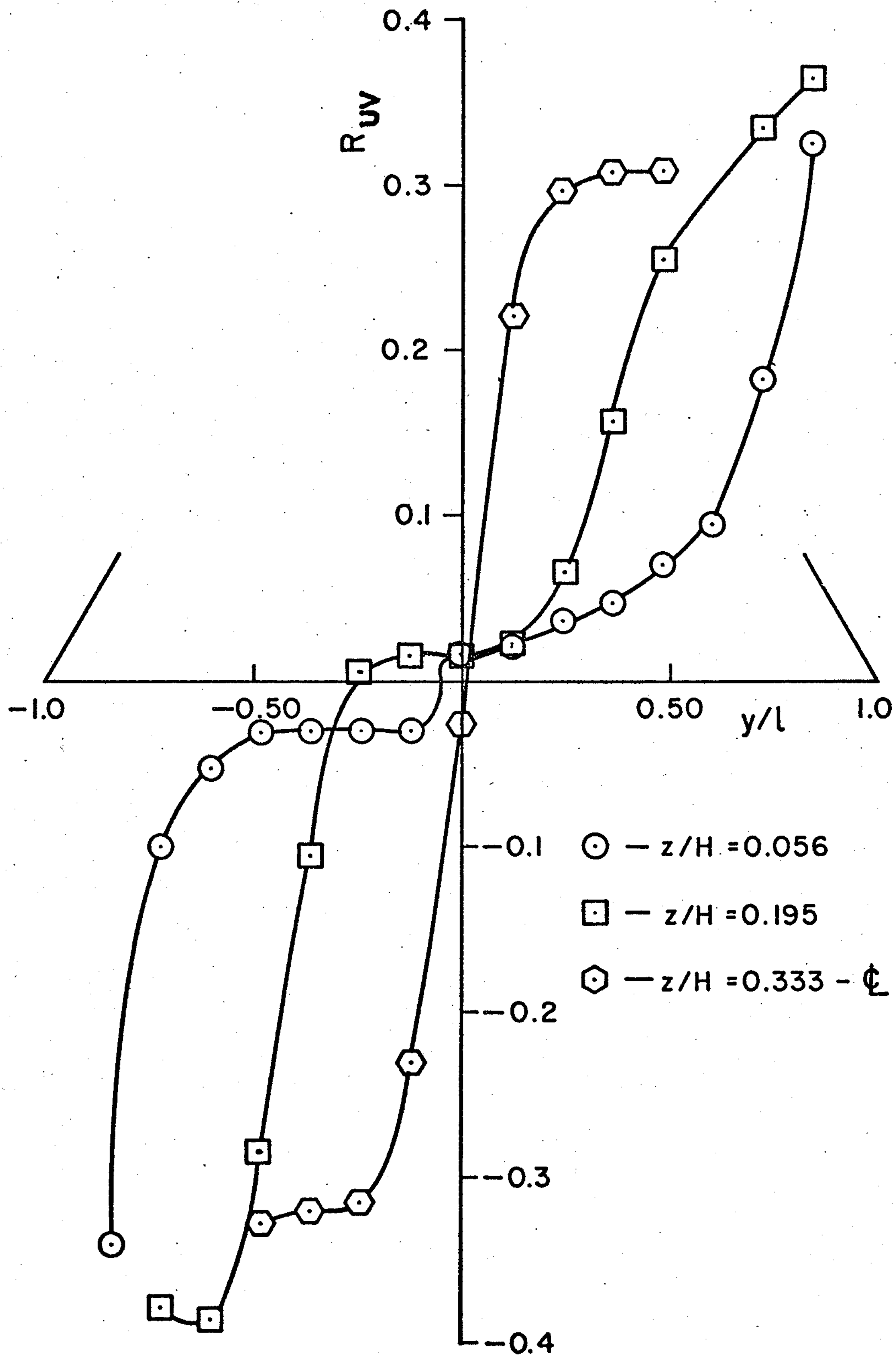

Figure 9. R_{uv} Distribution Along Horizontal Traverses in Triangular Duct.

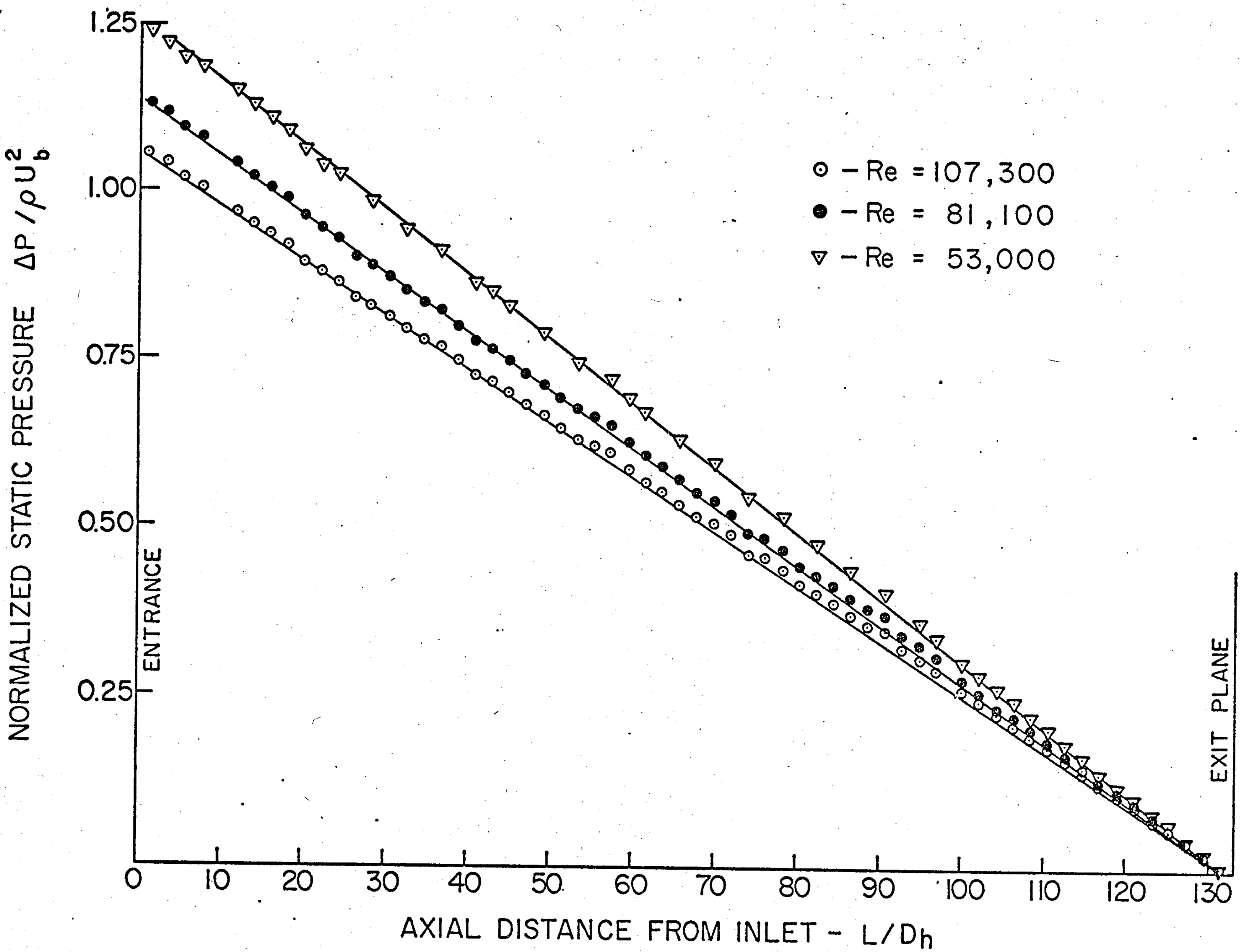

Fig. 10. Static Pressure Distribution Along Duct Axis.

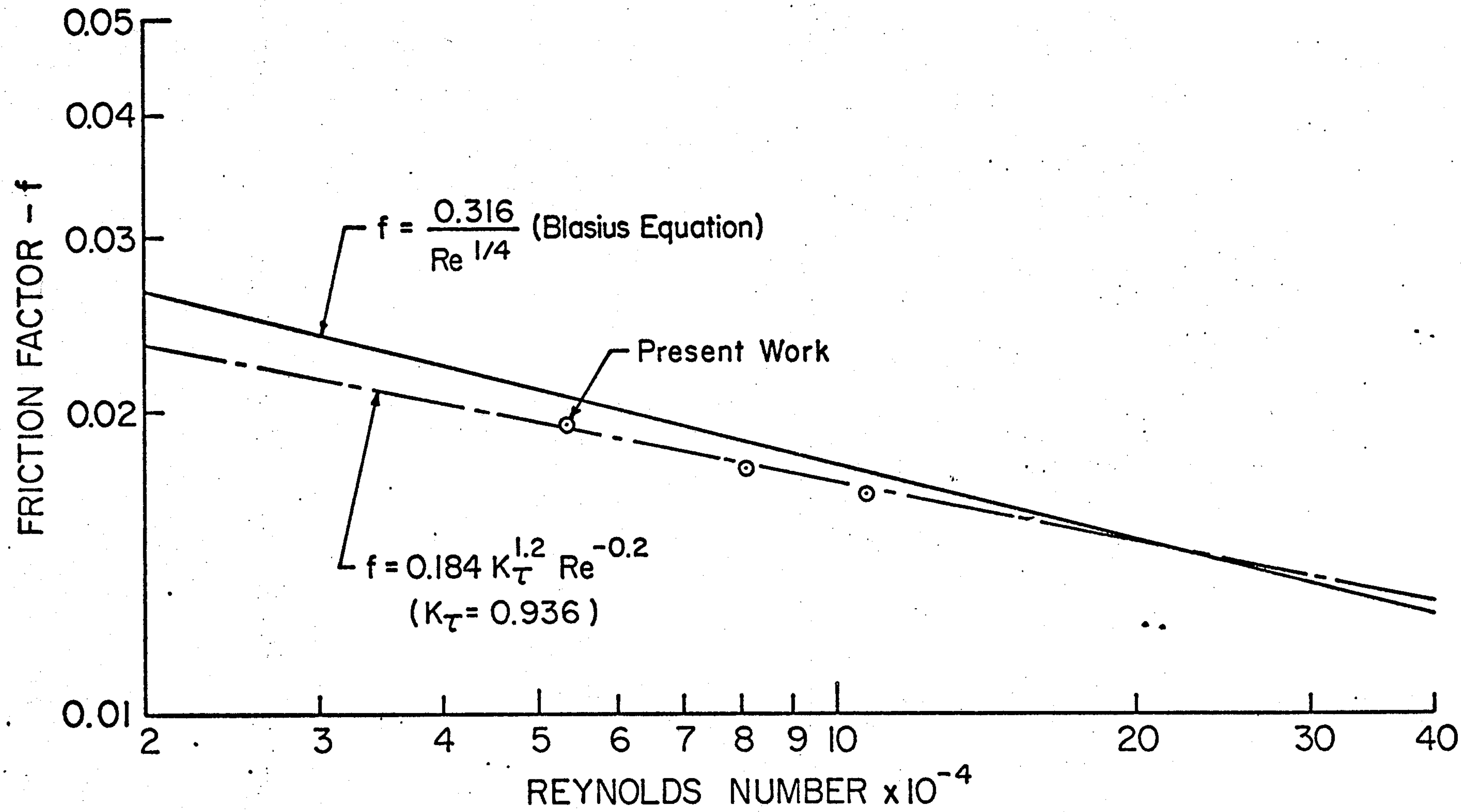

Fig. 11. Friction Factor vs. Reynolds Number in Equilateral Triangular Duct.

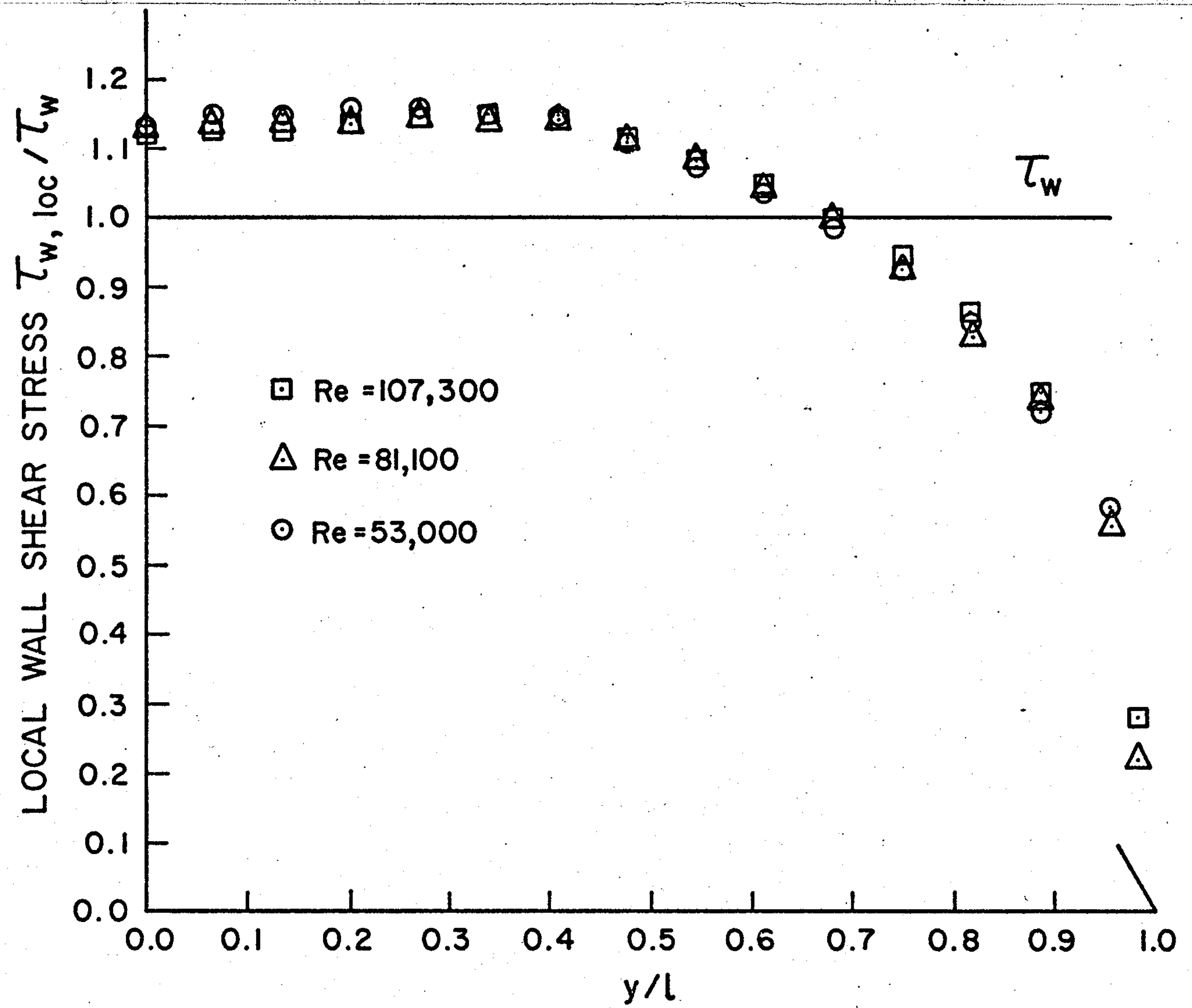

Figure 12. Local Wall Shear Stress Distribution in Equilateral Triangular Duct.

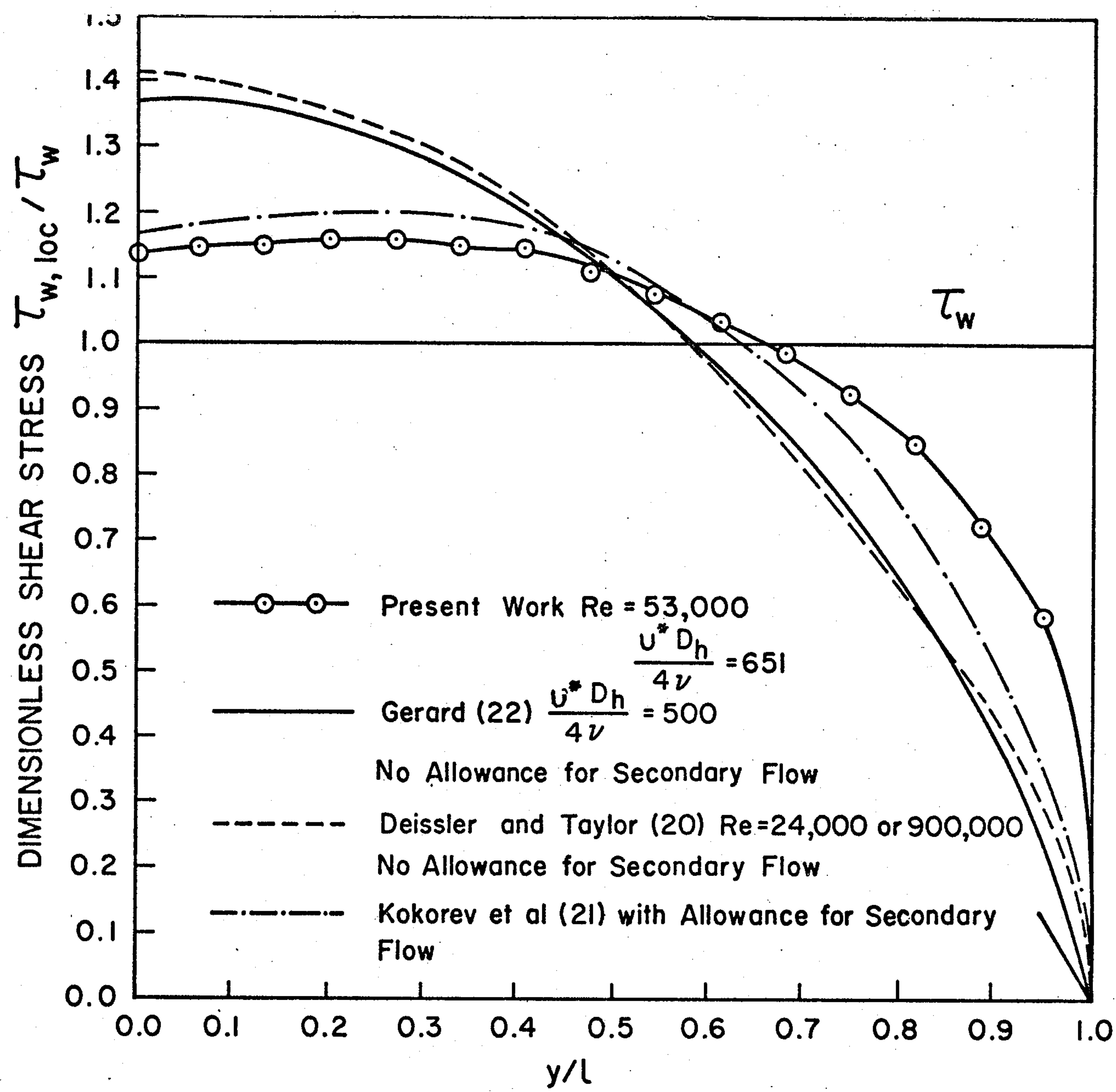

Figure 13. Comparison of Measured and Calculated Wall Shear Stress Distributions in Equilateral Triangular Duct.

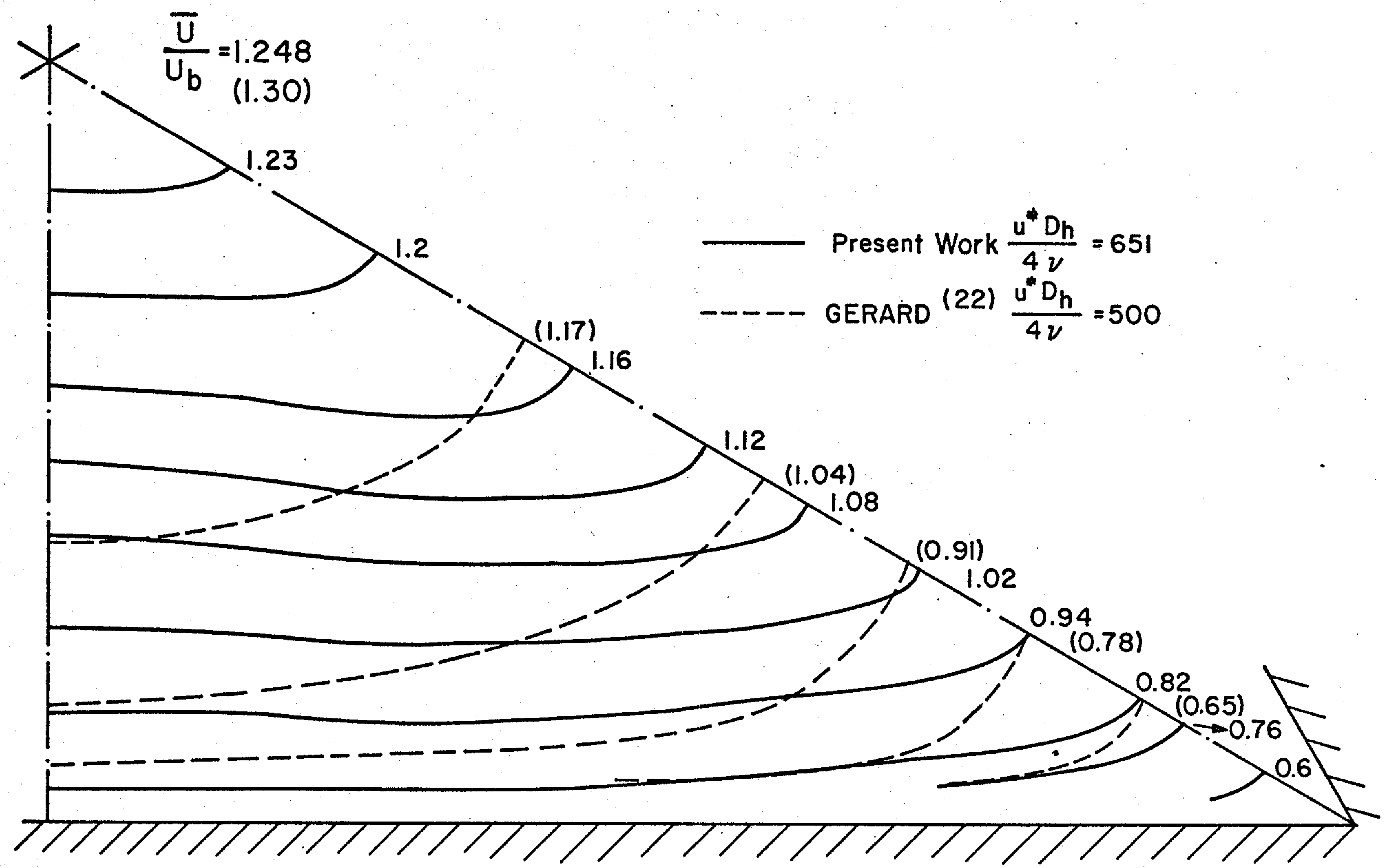

Figure 14 a. Isovel Plots in Primary Flow Cell of Triangular Duct. Re=53,000

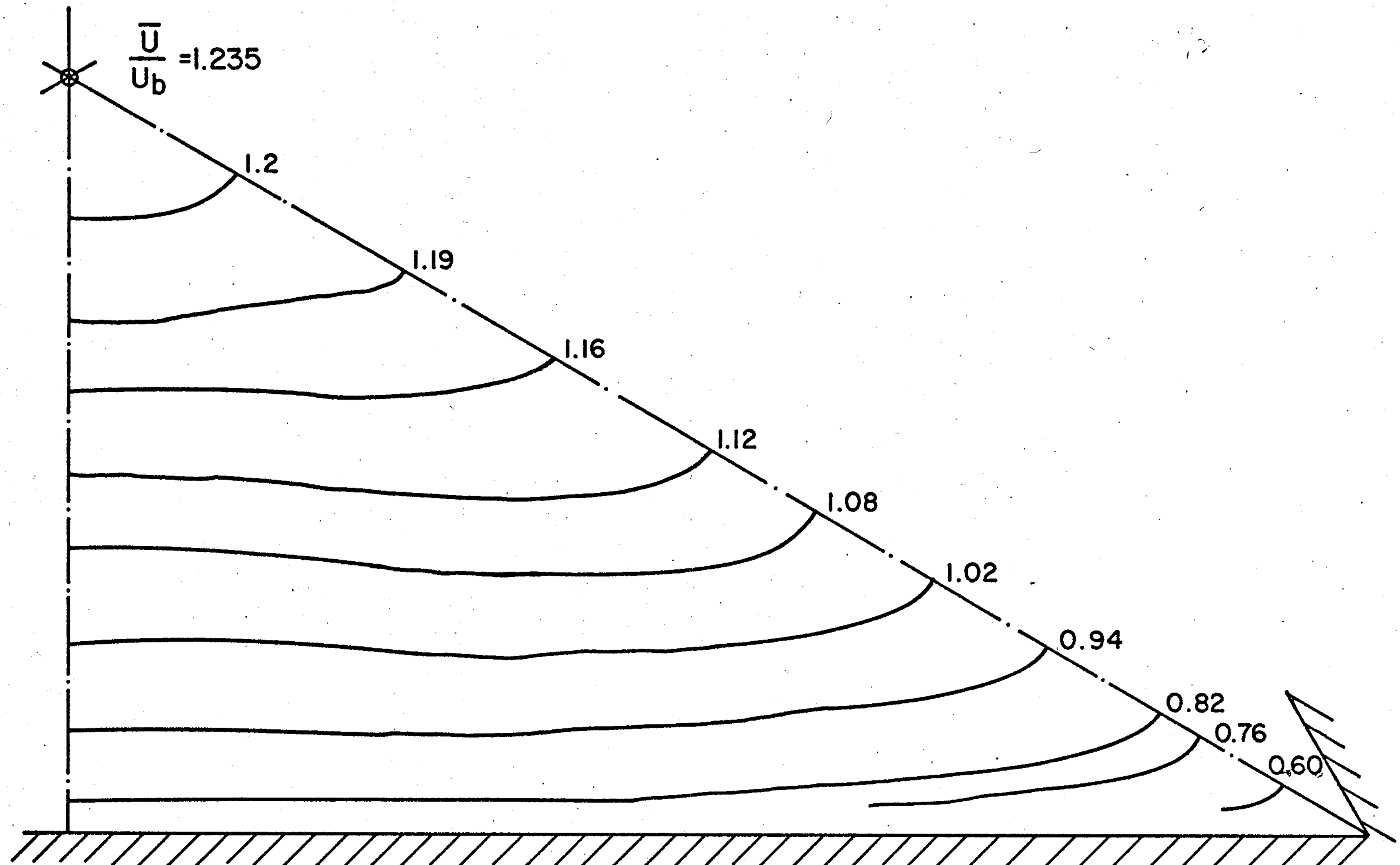

Figure 14b. Isovel Plots in Primary Flow Cell of Triangular Duct. Re = 81,100

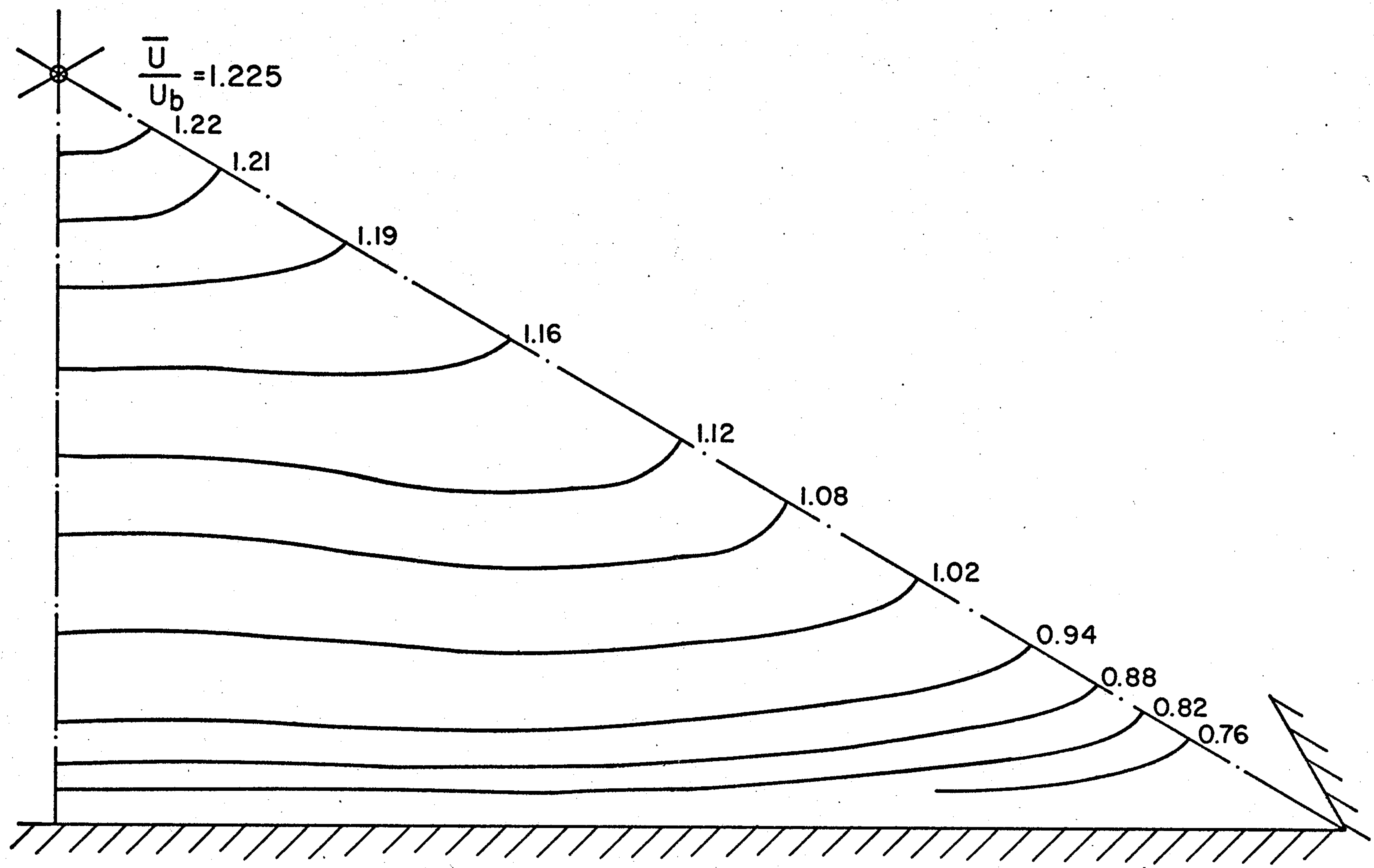

Figure 14c. Isovel Plots in Primary Flow Cell of Triangular Duct. Re=107,300

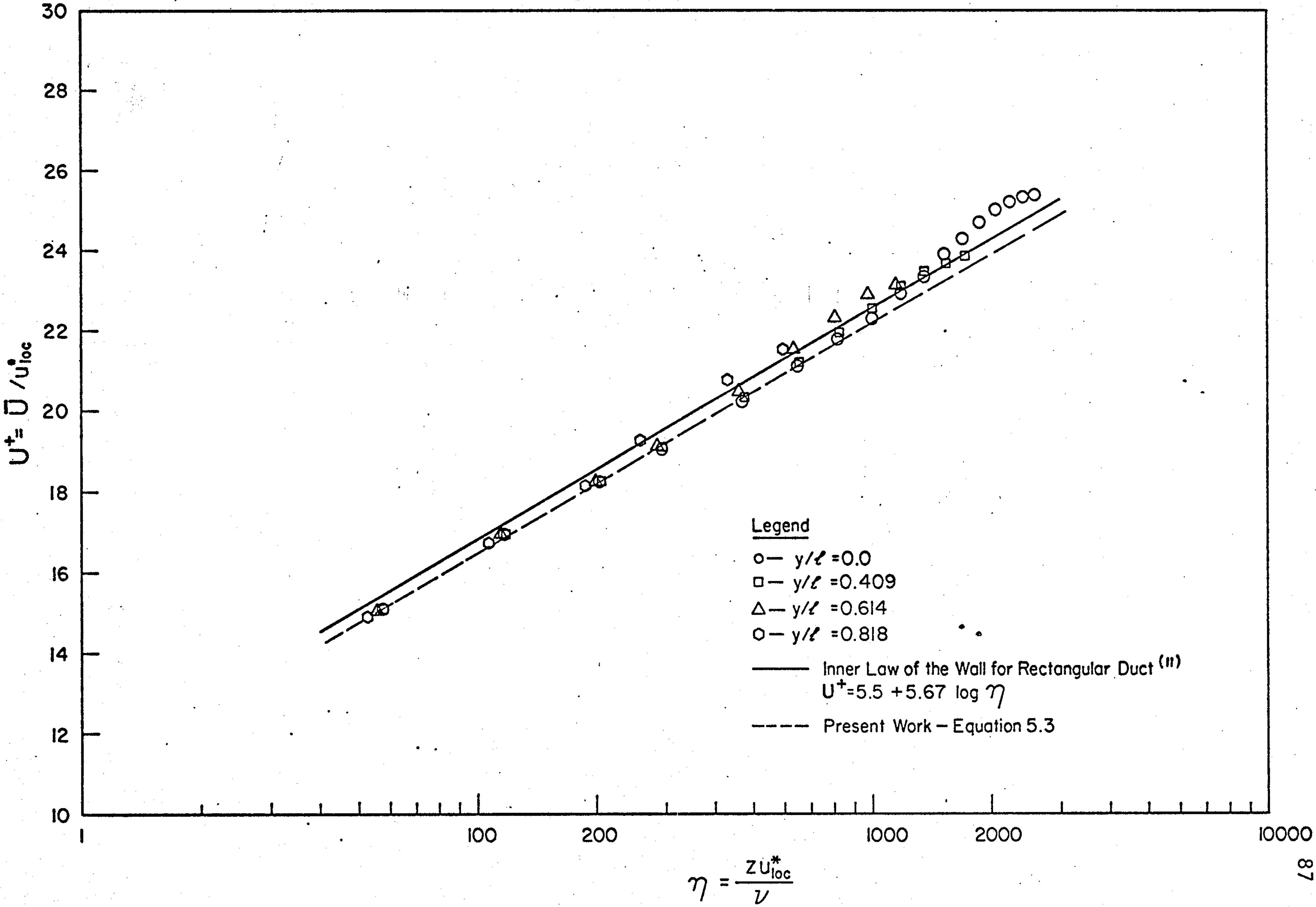

Fig.15 Mean Velocity Distribution in Inner Law Coordinates Based on Local Friction Velocity. Re = 107, 300

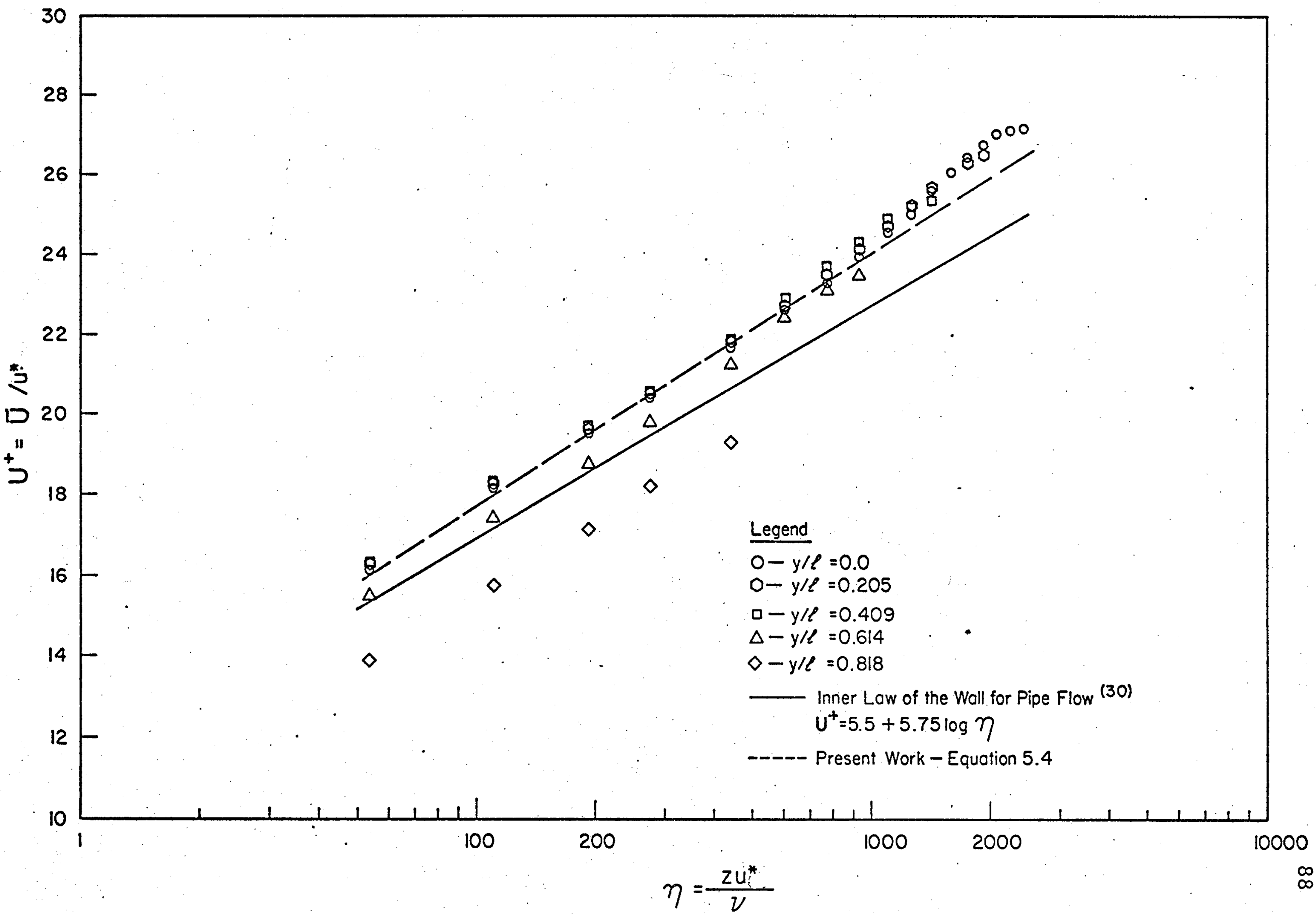

Fig.16 Mean Velocity Distribution in Inner Law Coordinates Based on Average Friction Velocity. Re = 107, 300

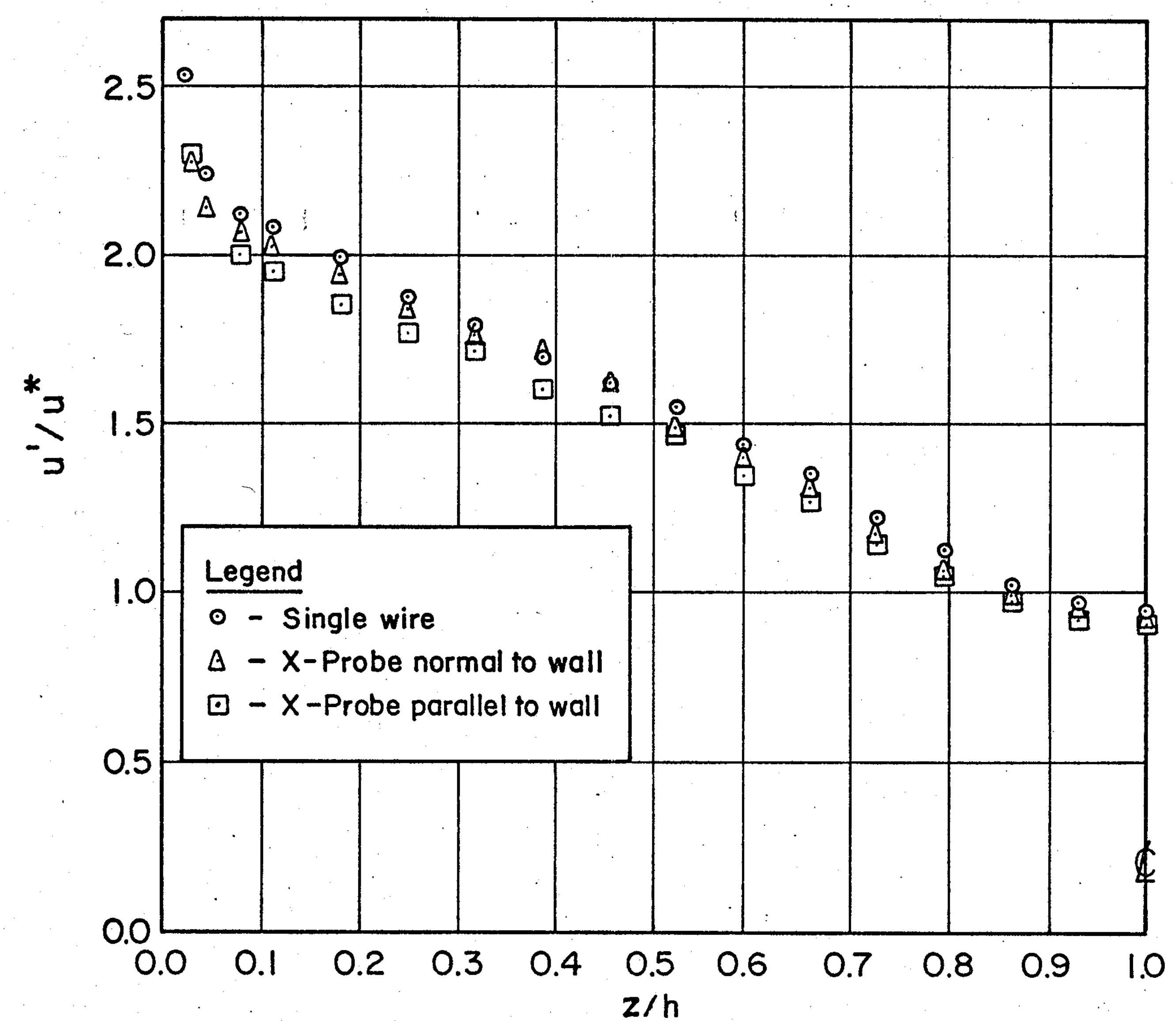

Figure. 17. Comparison of u'/u^* Measurements with Different Probes. $y/\ell = 0$, Re=53,000

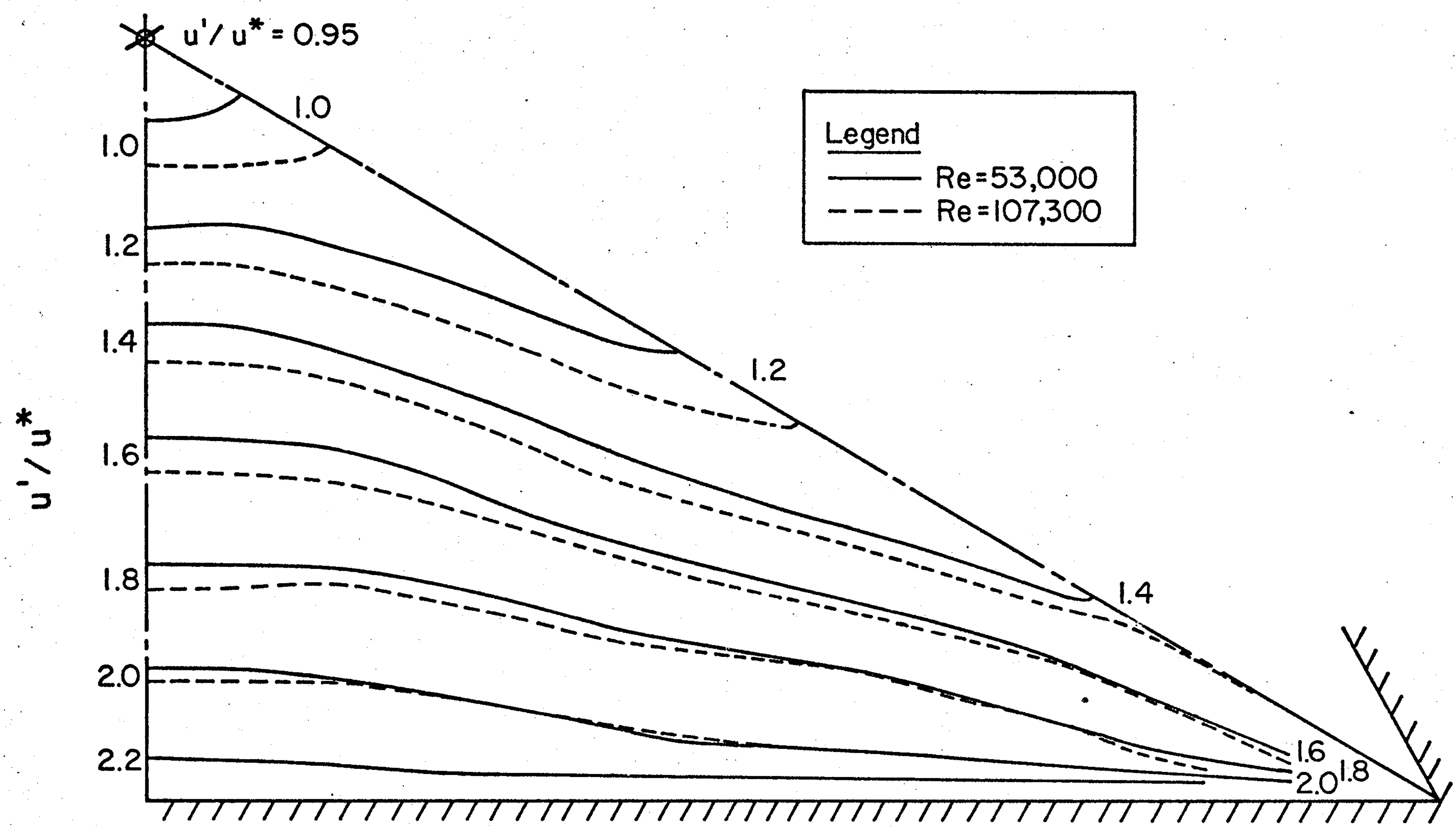

Figure 18. Contour Plot of u'/u^* Distribution in Equilateral Triangular Duct. Re = 53,000.

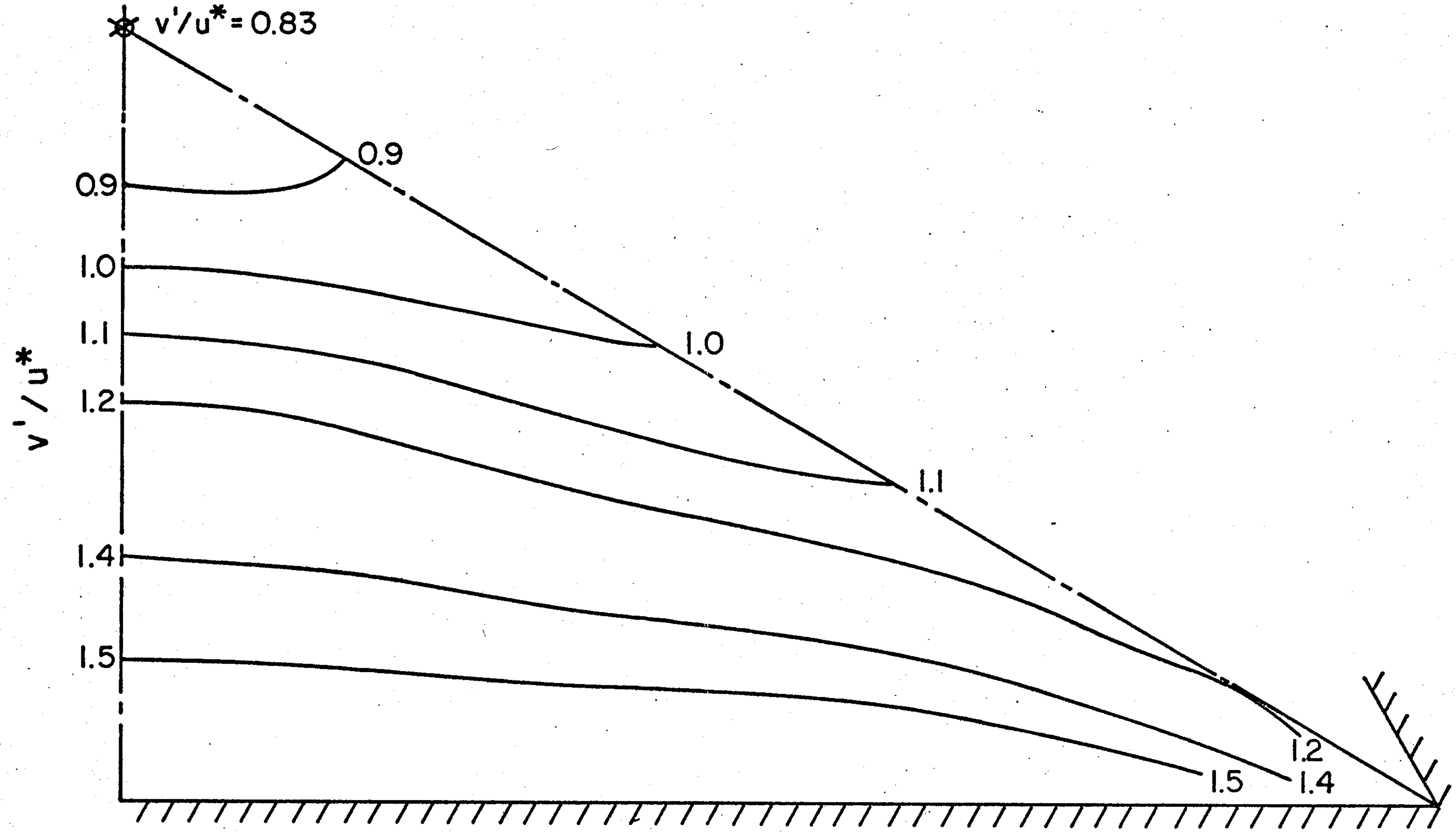

Figure 19. Contour Plot of v'/u^* Distribution in Equilateral Triangular Duct. Re = 53,000

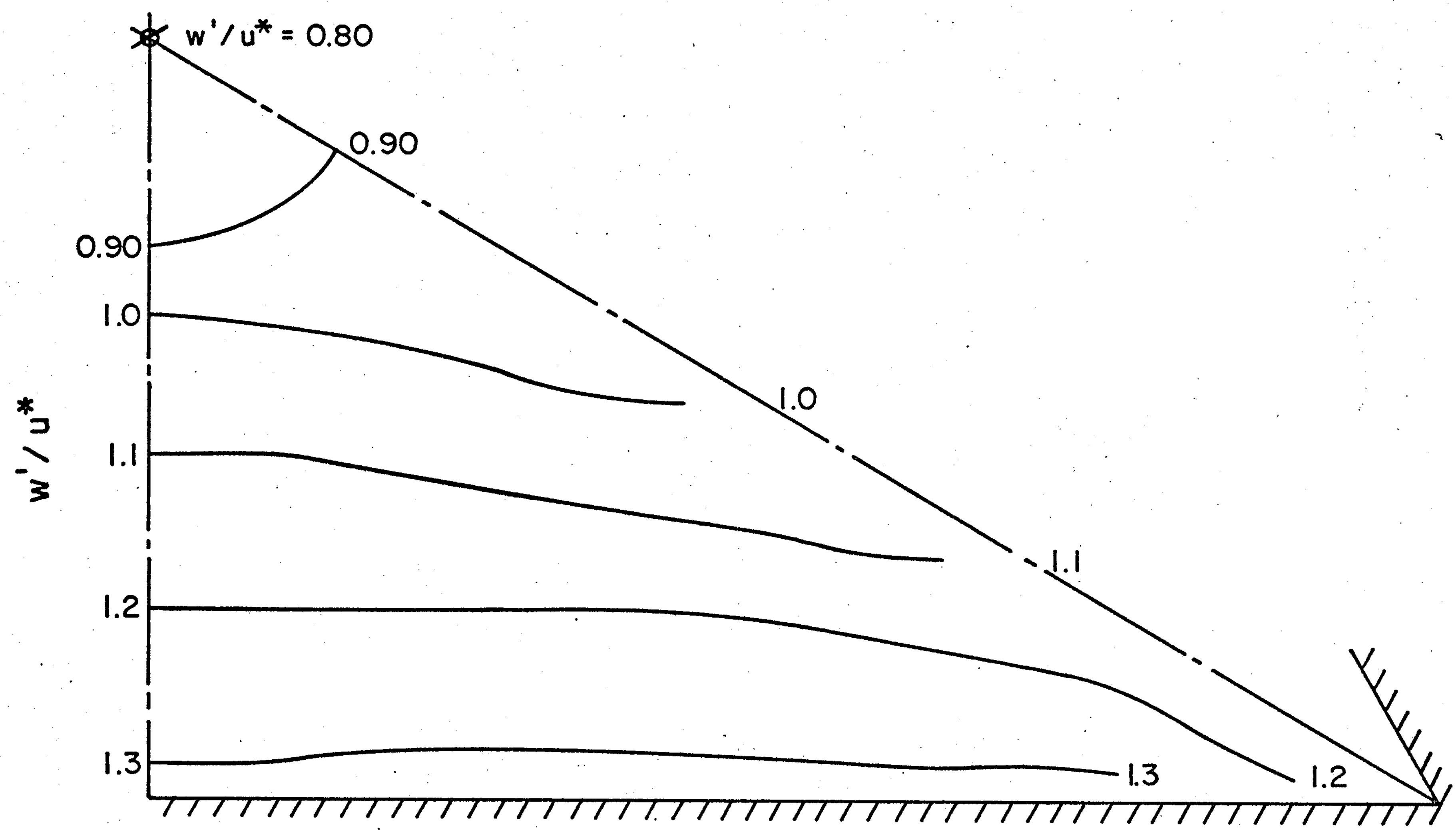

Figure 20. Contour Plot of w'/u^* Distribution in Equilateral Triangular Duct. Re = 53,000.

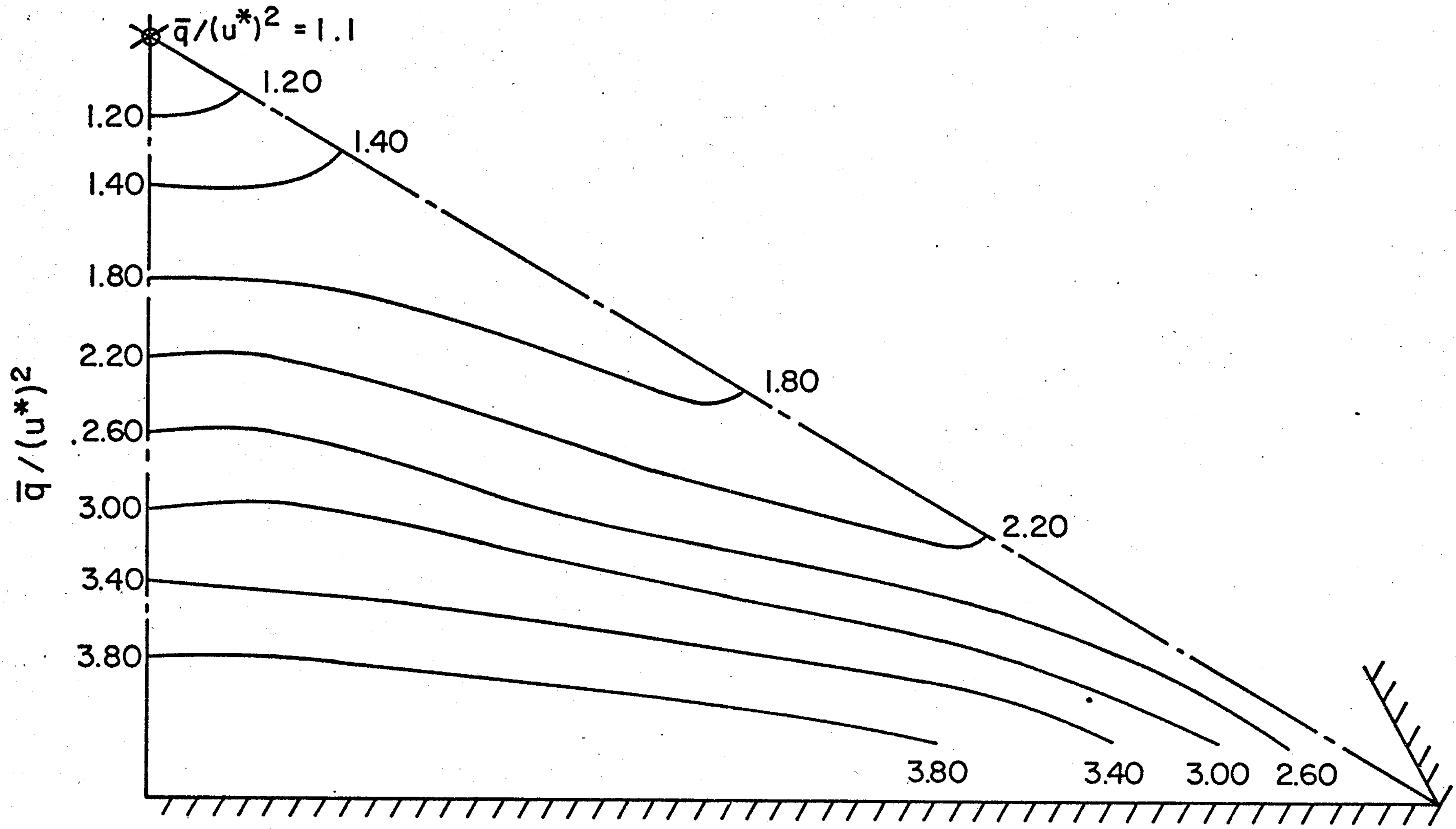

Figure 21. Mean Turbulent Kinetic Energy Distribution in Equilateral Triangular Duct. Re=53,000

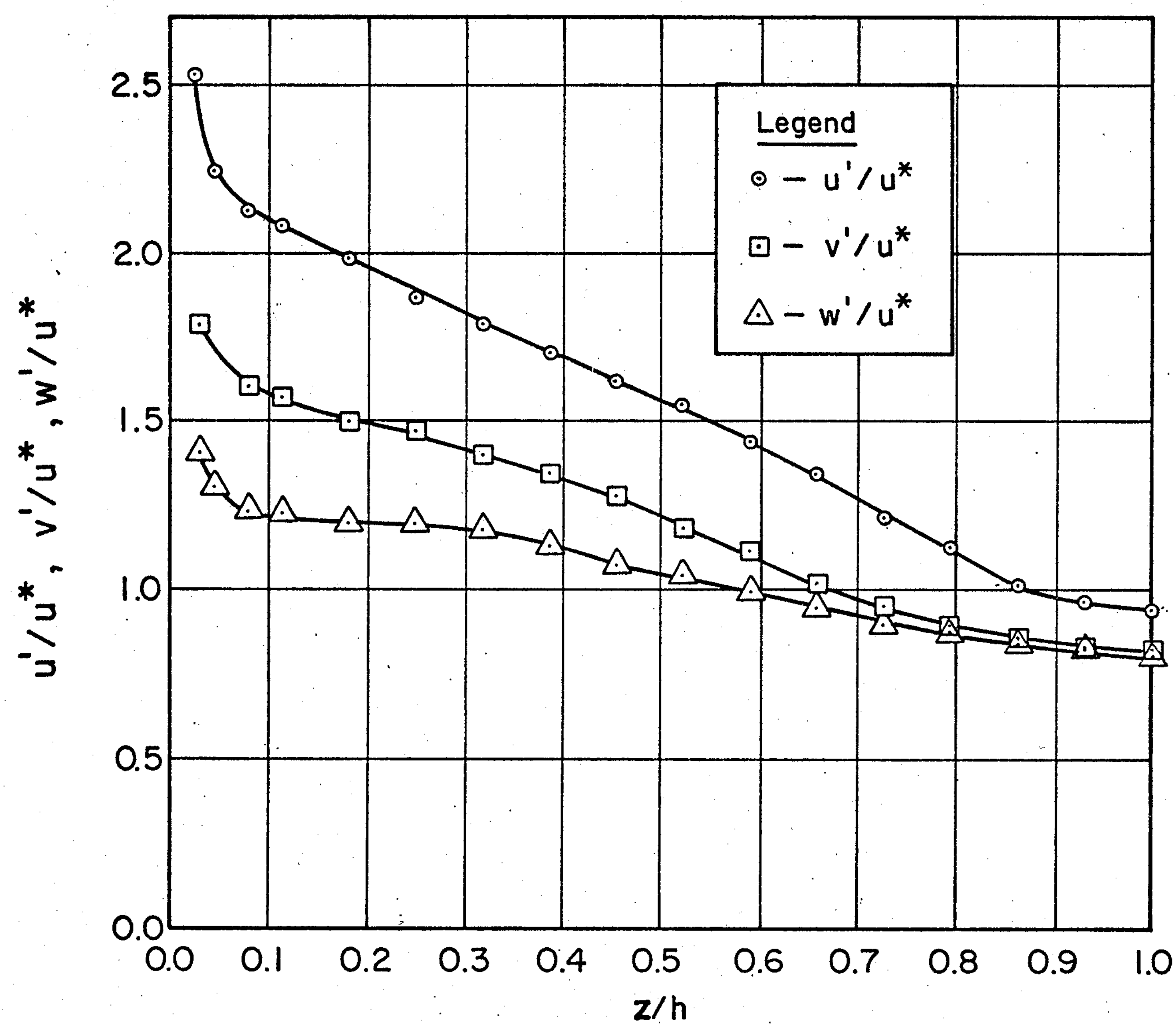

Figure 22. Distributions of u'/u^*, v'/u^*, and w'/u^* Normal to Wall of Equilateral Triangular Duct. $y/\ell = 0$, Re = 53,000.

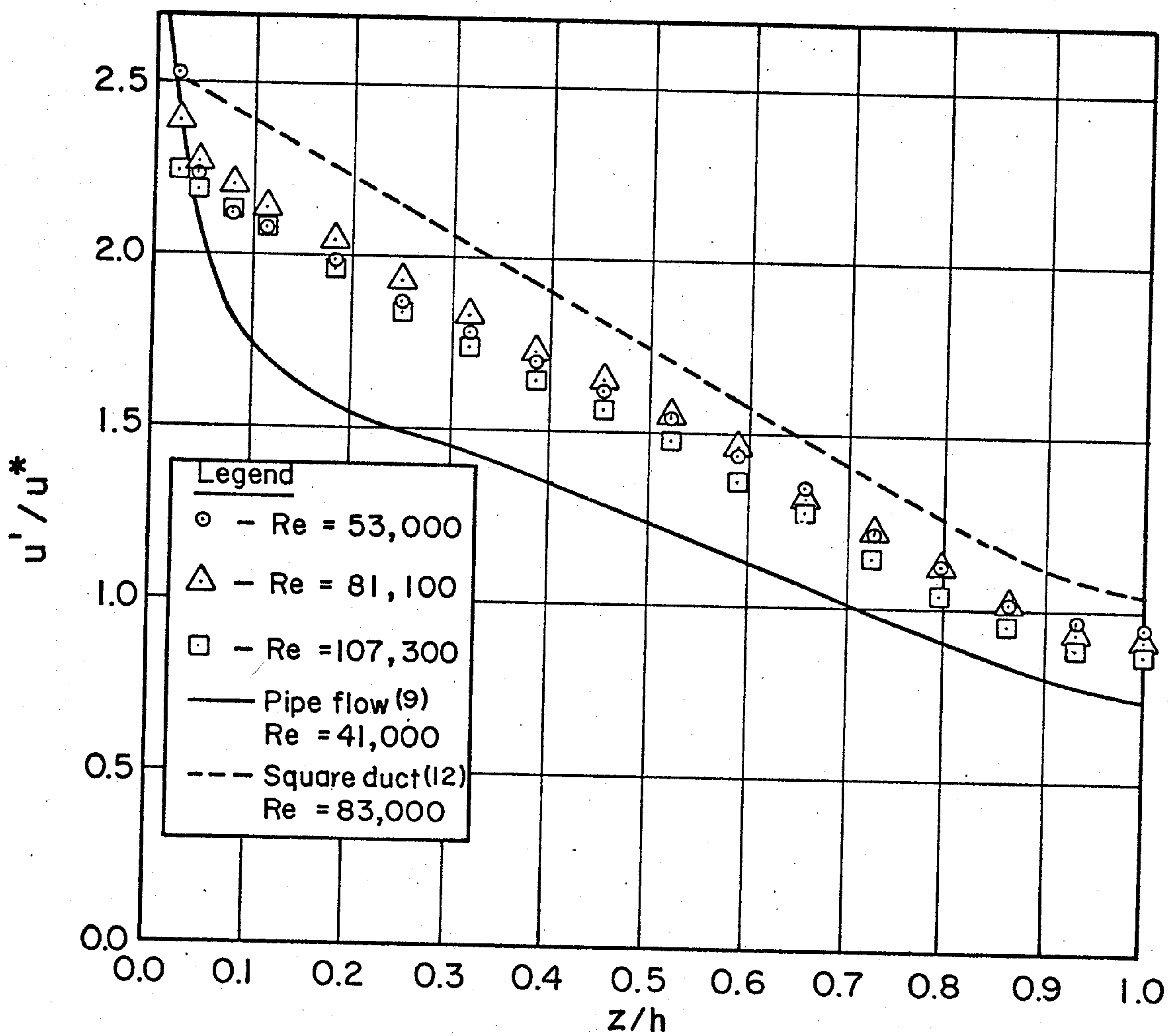

Figure 23. Reynolds Number Variation of u'/u^* Distribution in Equilateral Triangular Duct. $y/\ell = 0$

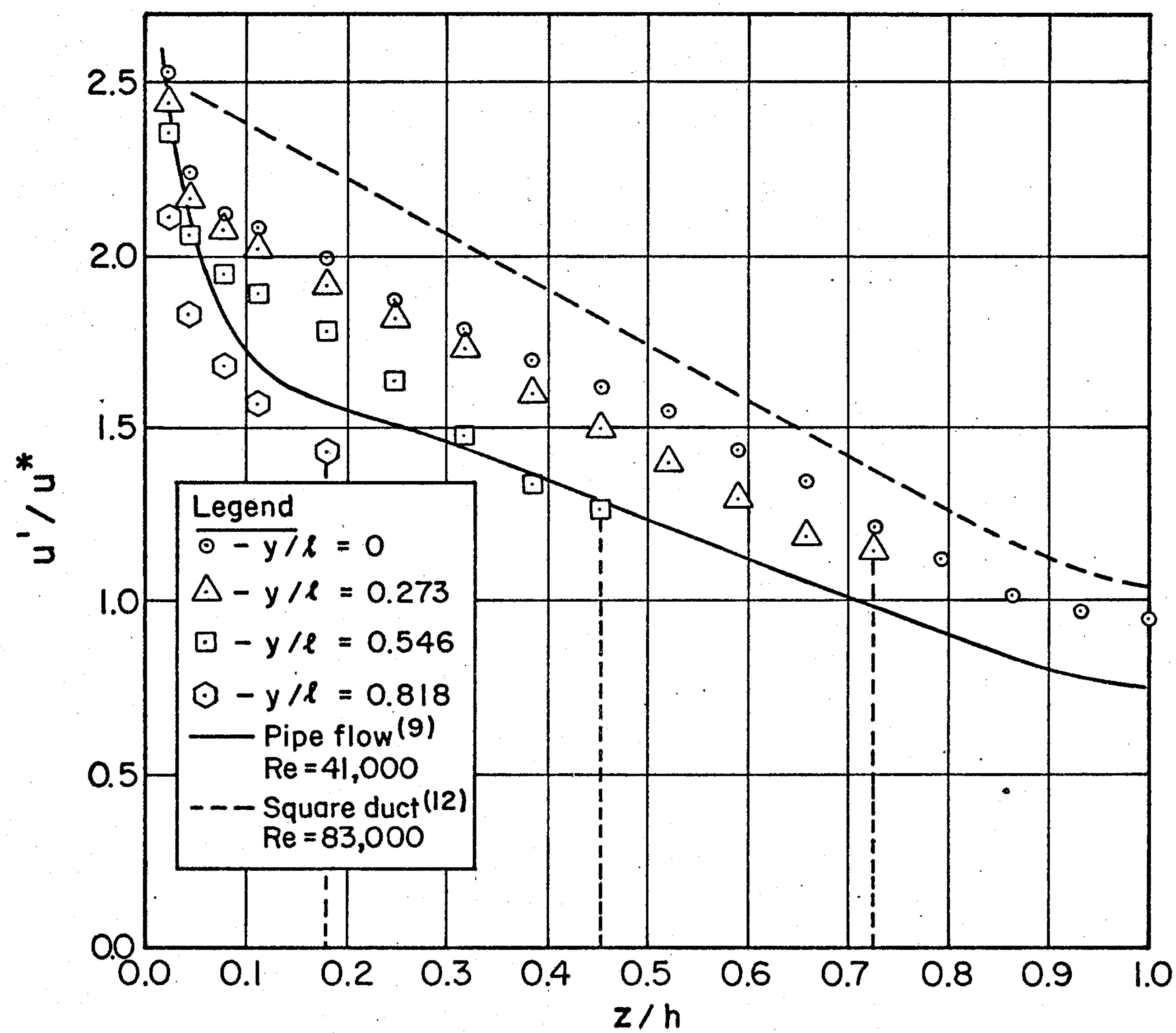

Figure 24. Variation of u'/u^* Distribution with Distance from Midwall in Triangular Duct.
Re = 53,000

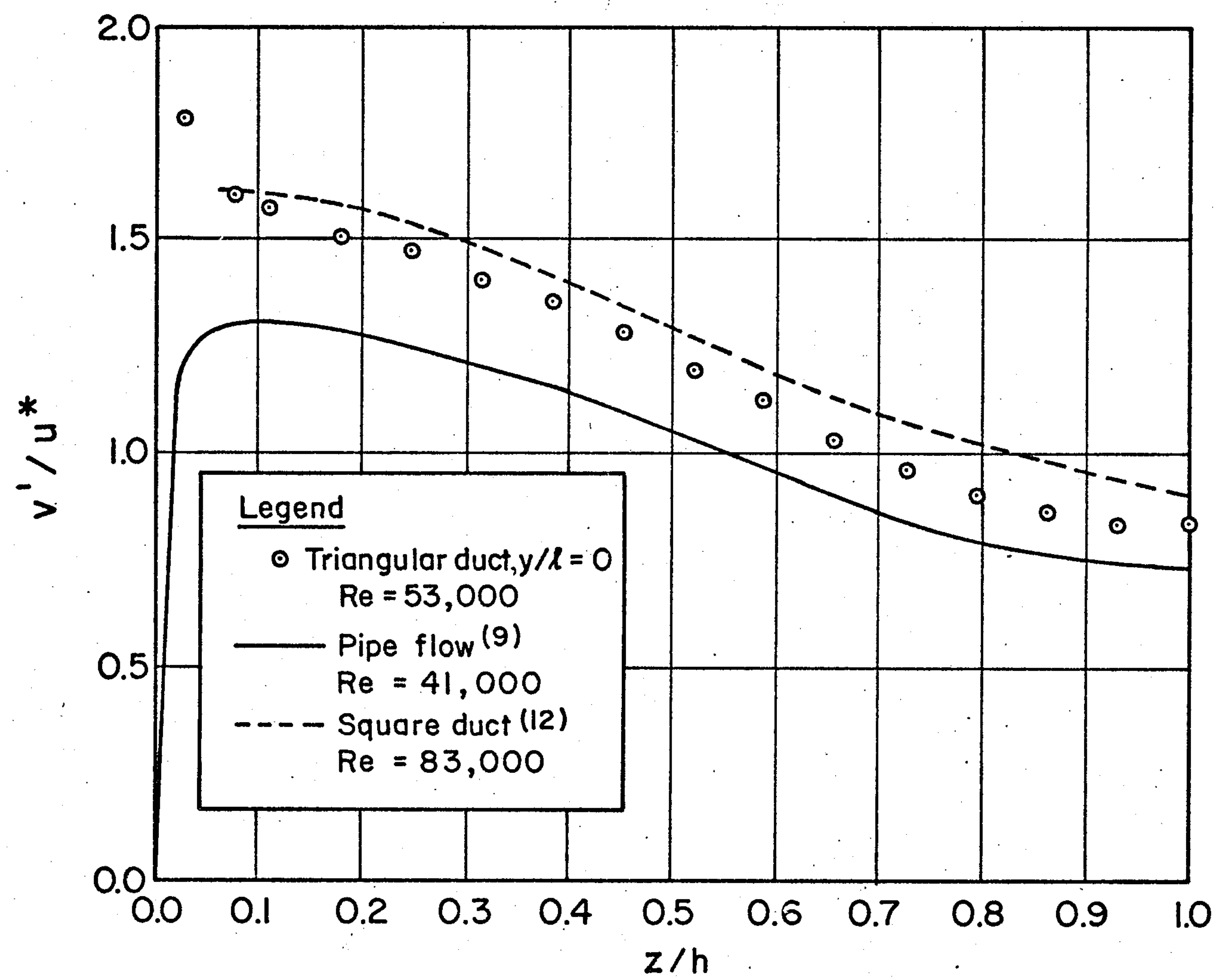

Figure 25. Comparison of v'/u^* Distribution in Equilateral Triangular Duct with Pipe and Square Duct Flows.

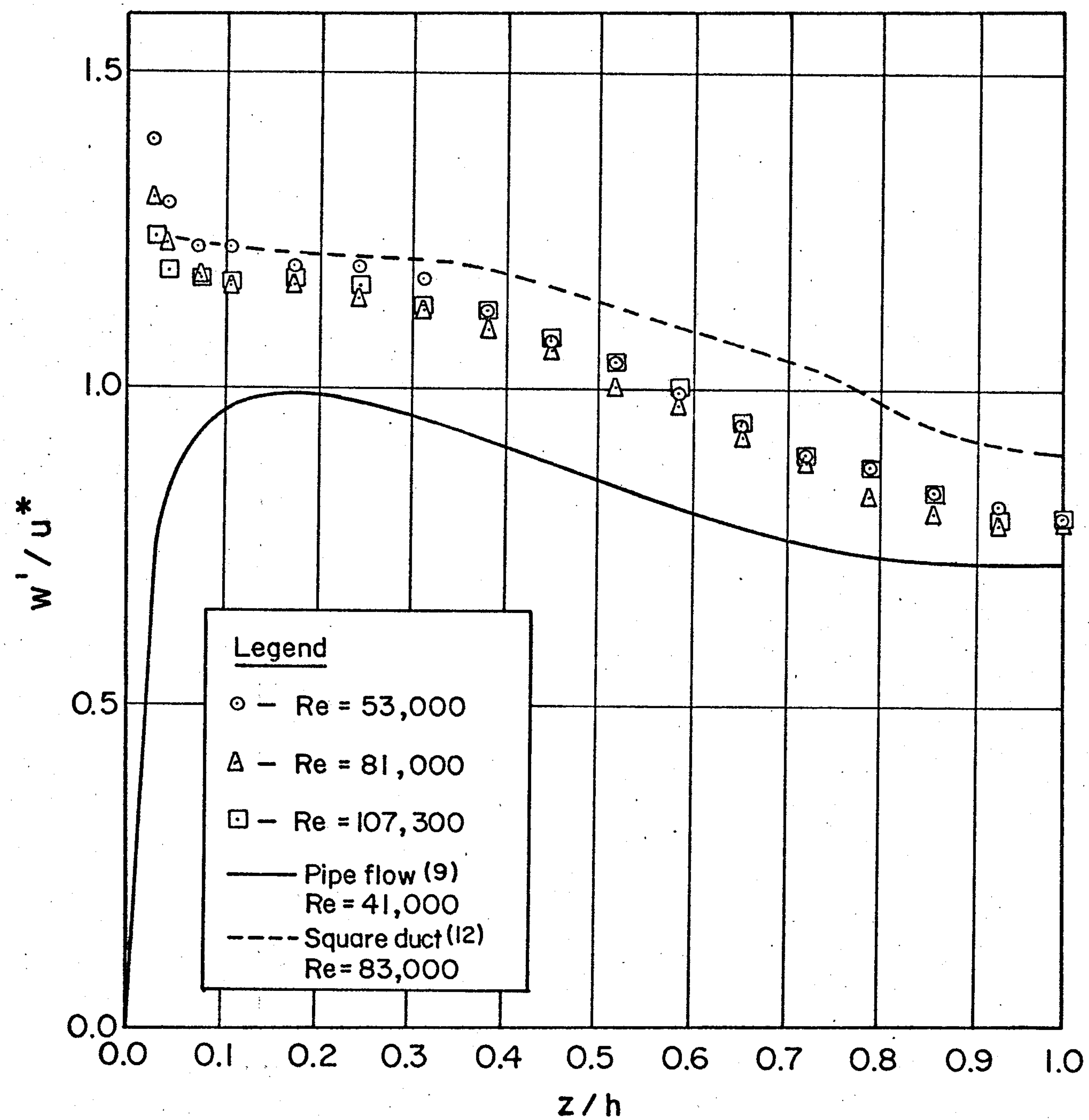

Figure 26. Reynolds Number Variation of w'/u^* Distribution Normal to Midwall in Triangular Duct.

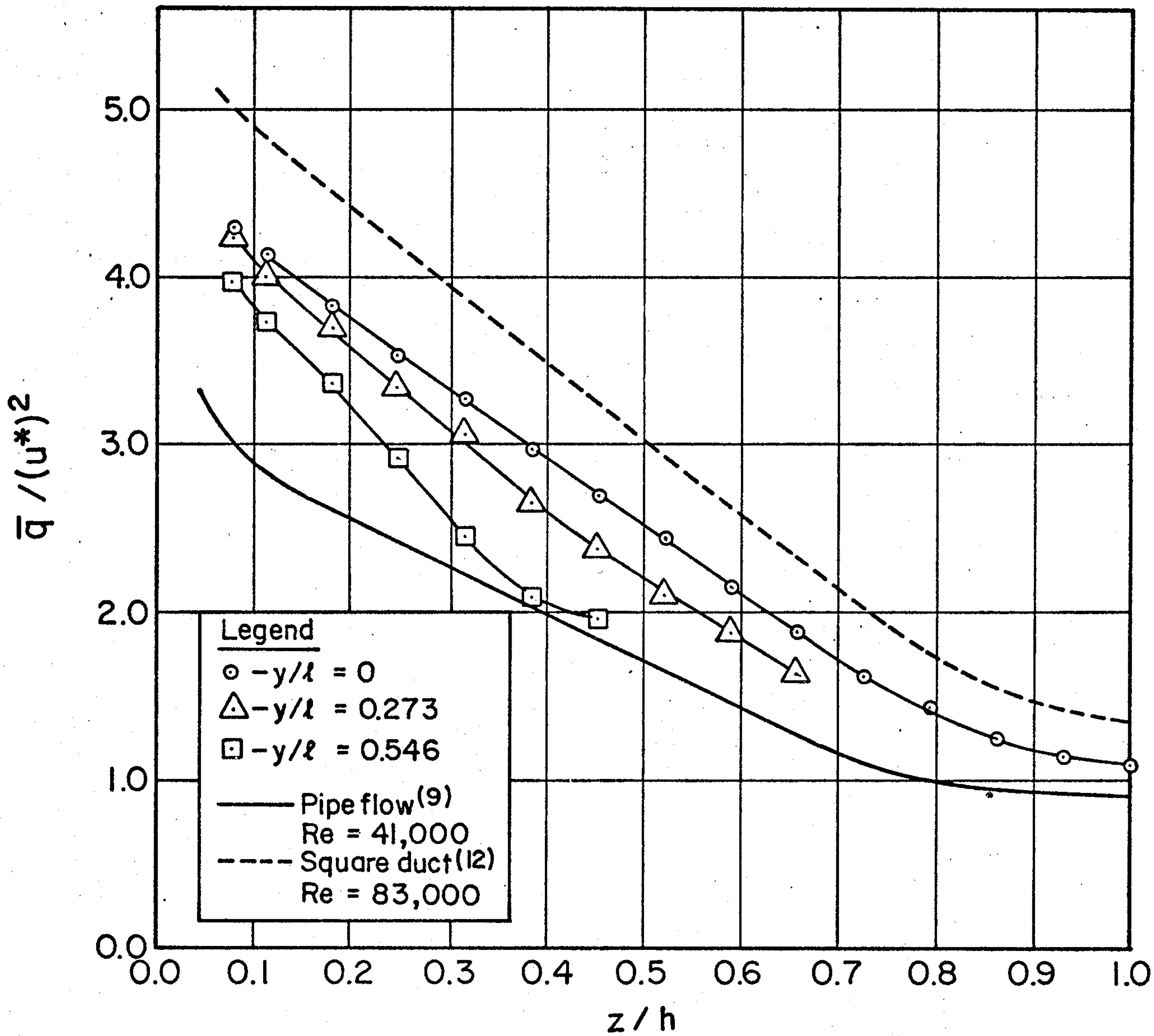

Figure 27. Distribution of $\overline{q}/(u^*)^2$ Normal to Wall in Triangular Duct. Re = 53,000

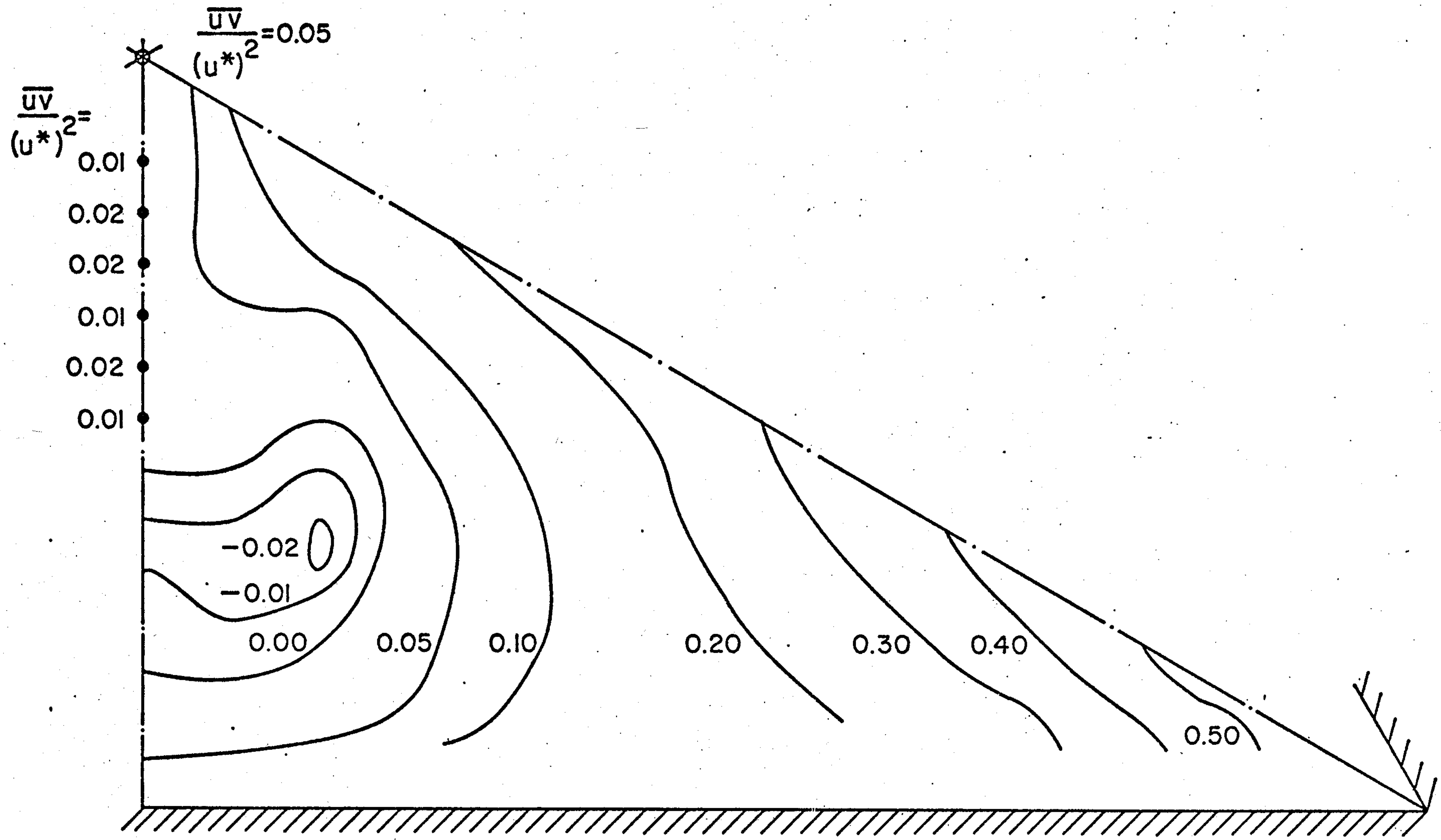

Figure. 28. Contour Plot of $\overline{uv}/(u^*)^2$ Distribution in Equilateral Triangular Duct. Re = 53,000

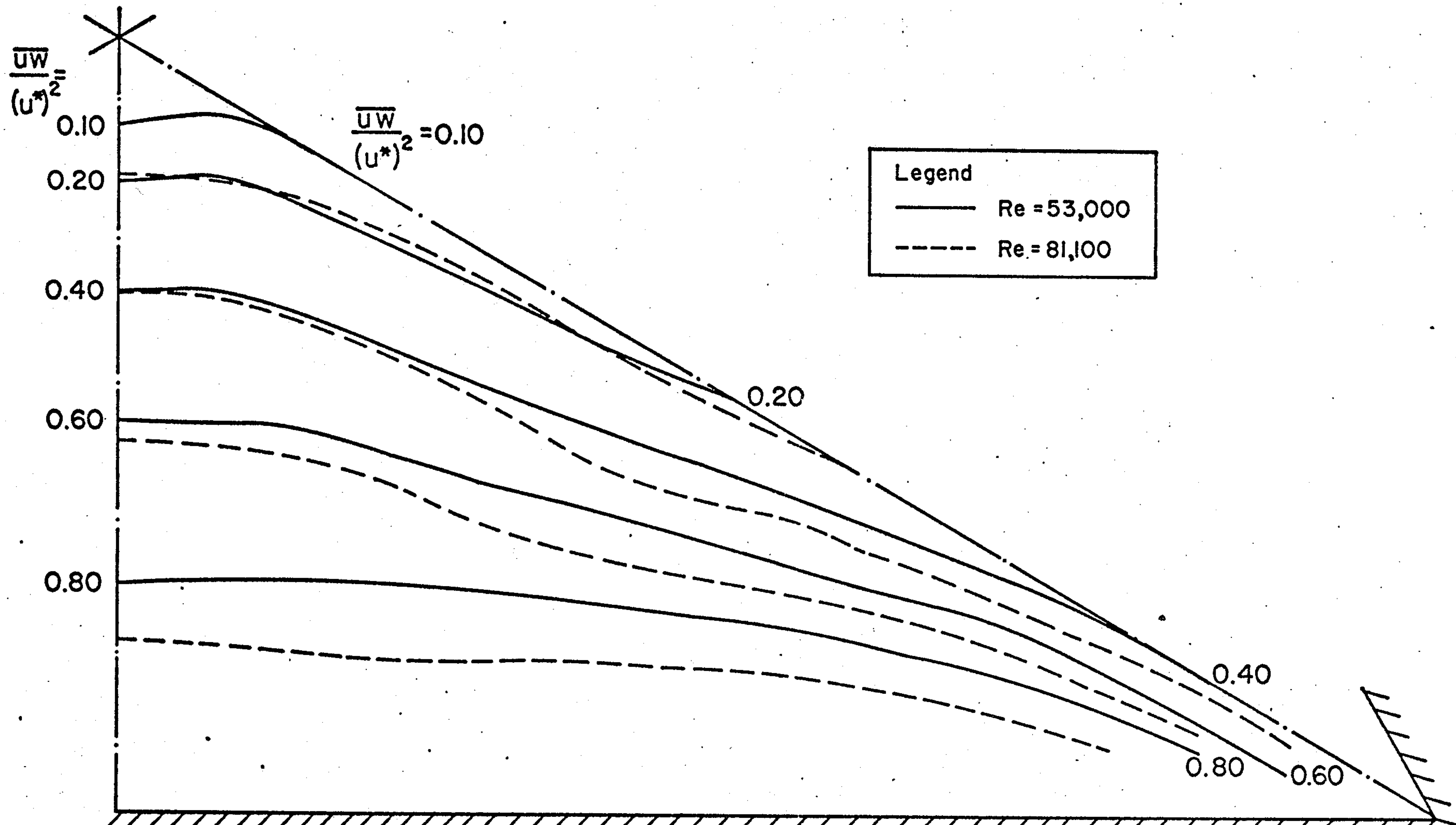

Fig. 29. Contour Plots of $\overline{uw}/(u^*)^2$ Distributions in Equilateral Triangular Duct.

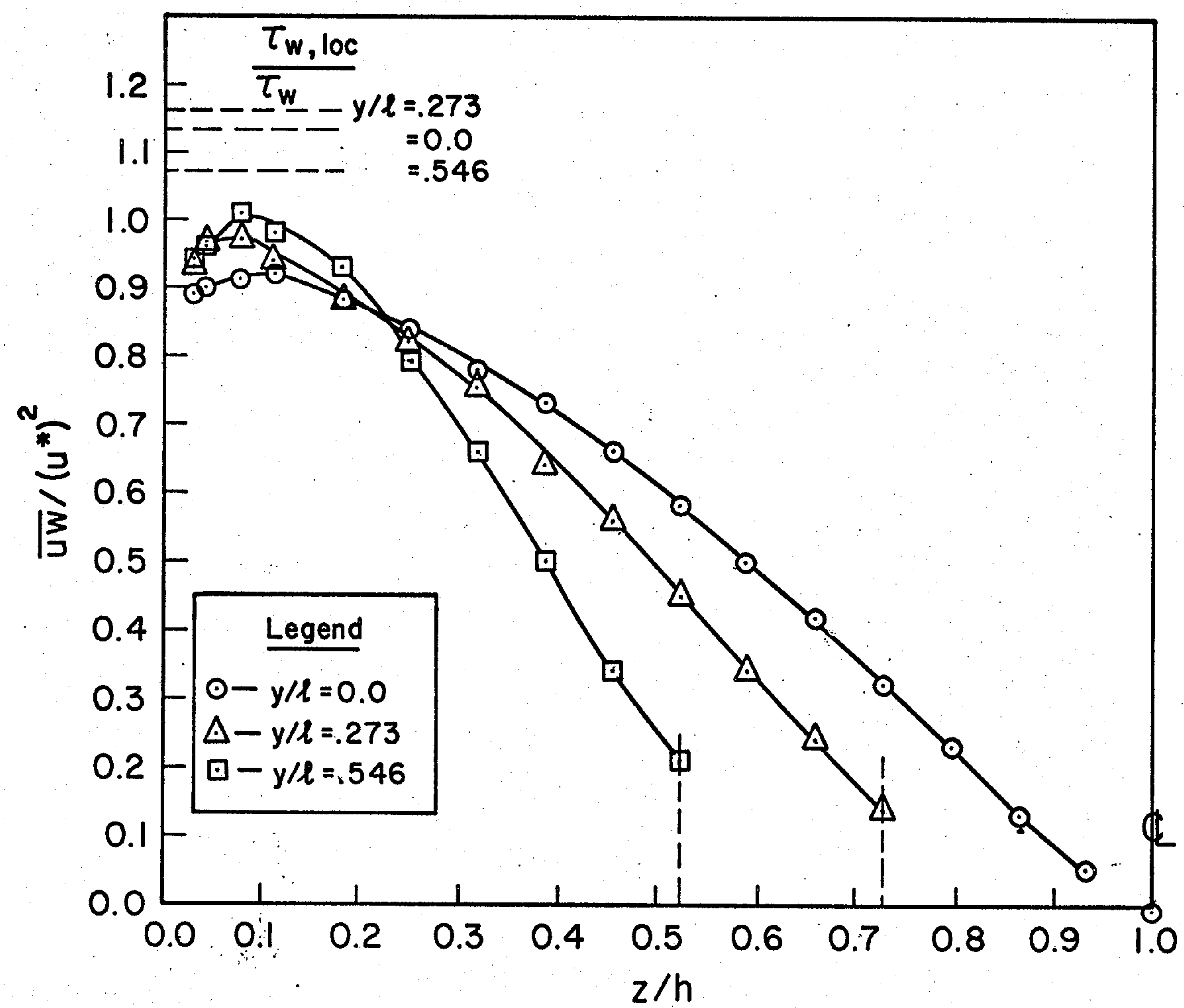

Fig. 30. Distributions of $\overline{uw}/(u^*)^2$ Along Normals to Wall in Equilateral Triangular Duct. Re = 53,000

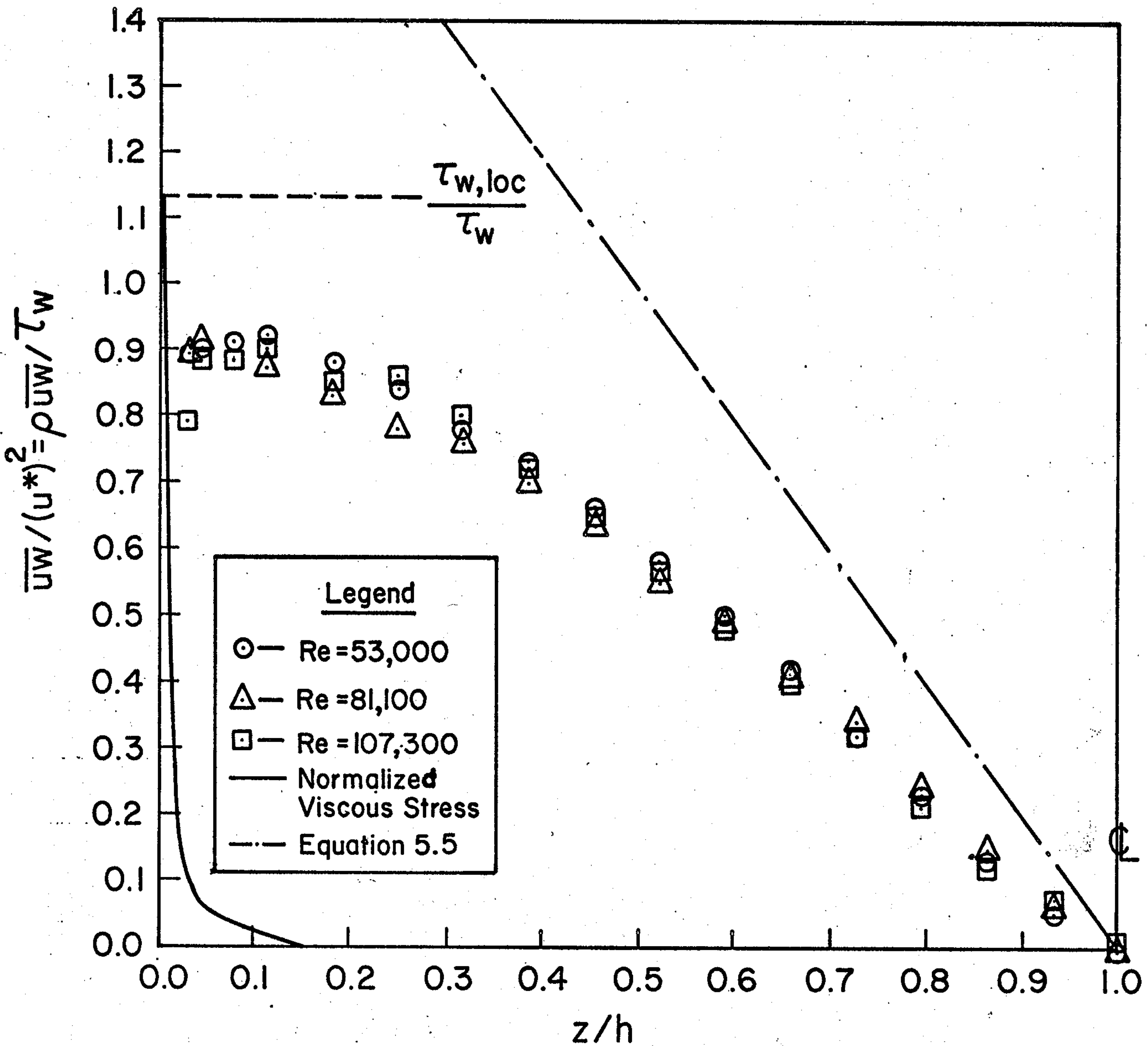

Fig. 31 Distributions of $\overline{uw}/(u^*)^2$ Along Midwall Bisector in Equilateral Triangular Duct.

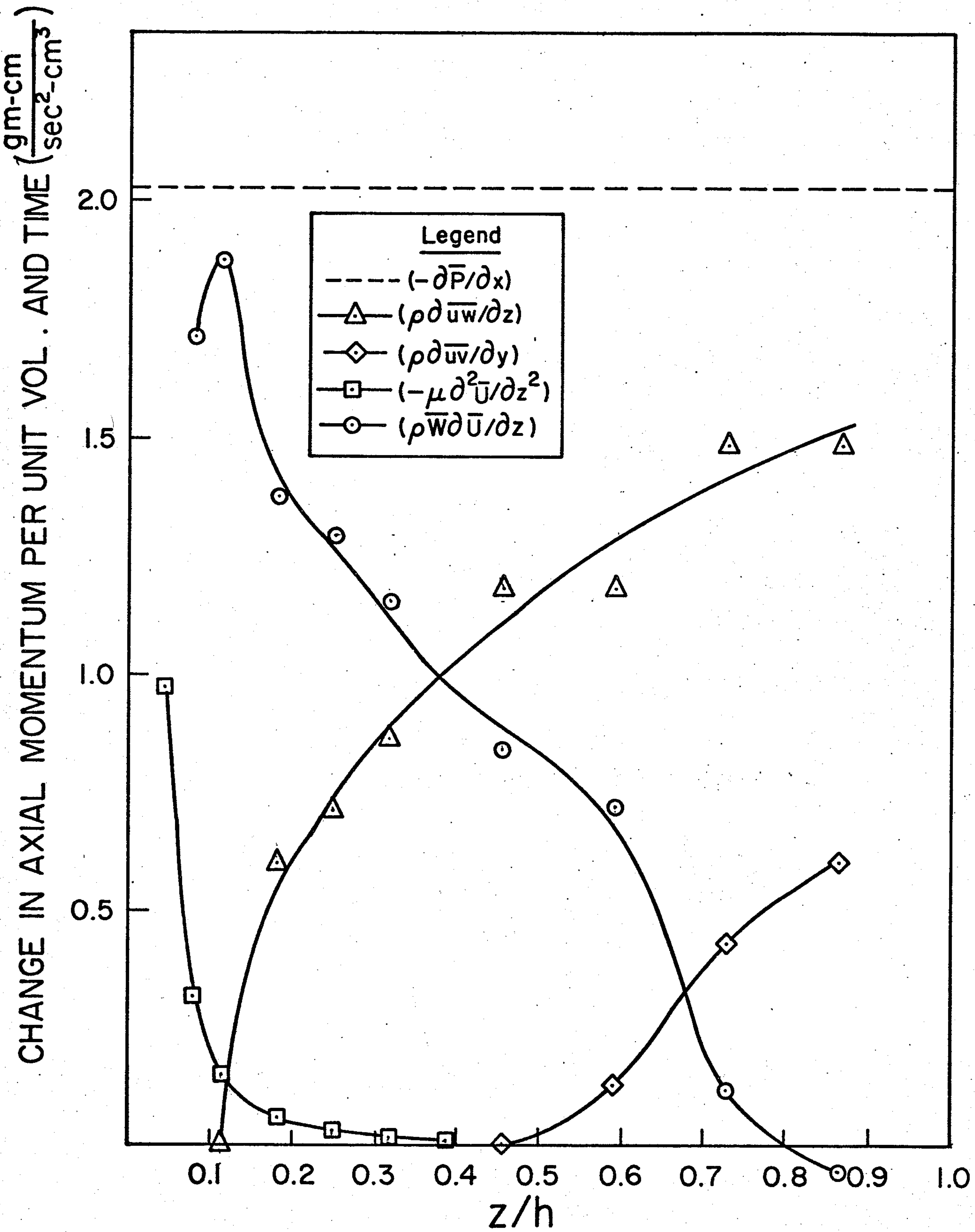

Fig. 32. Axial Momentum Balance Along Midwall Bisector in Equilateral Triangular Duct. Re = 53,000

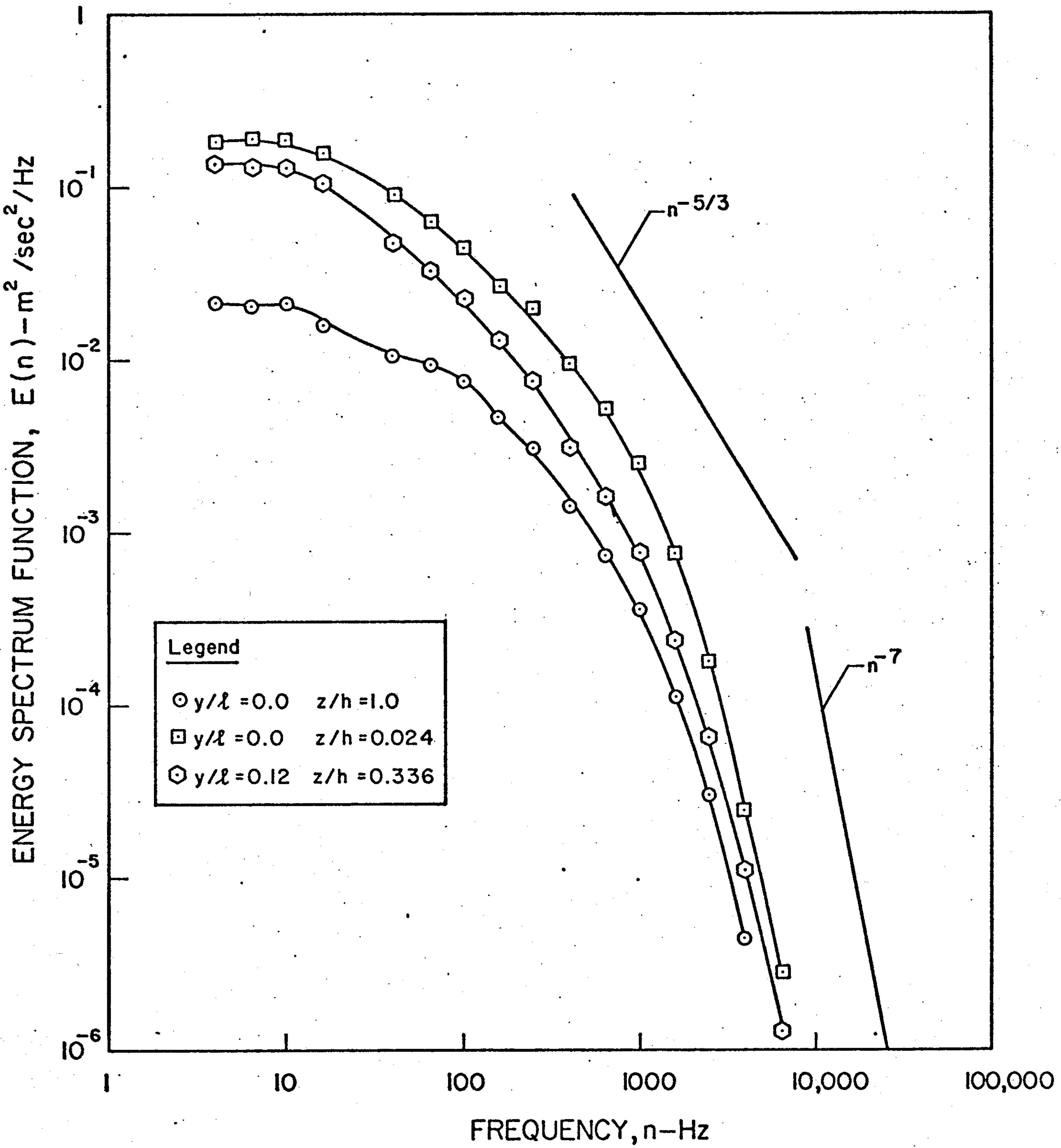

Fig. 33. Axial Power Spectra in Equilateral Triangular Duct. Re = 53,000

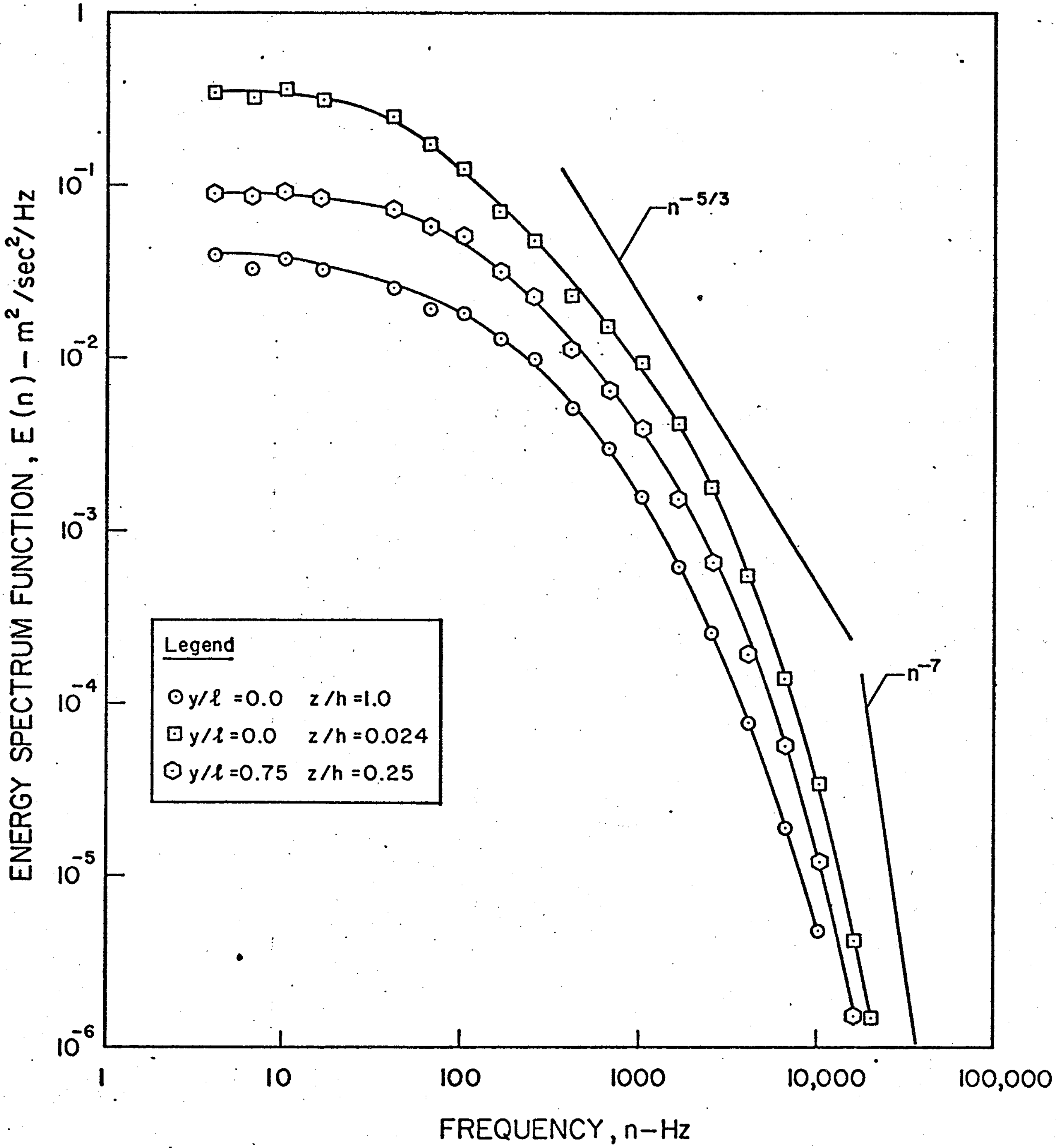

Fig. 34. Axial Power Spectra in Equilateral Triangular Duct. Re = 107,300

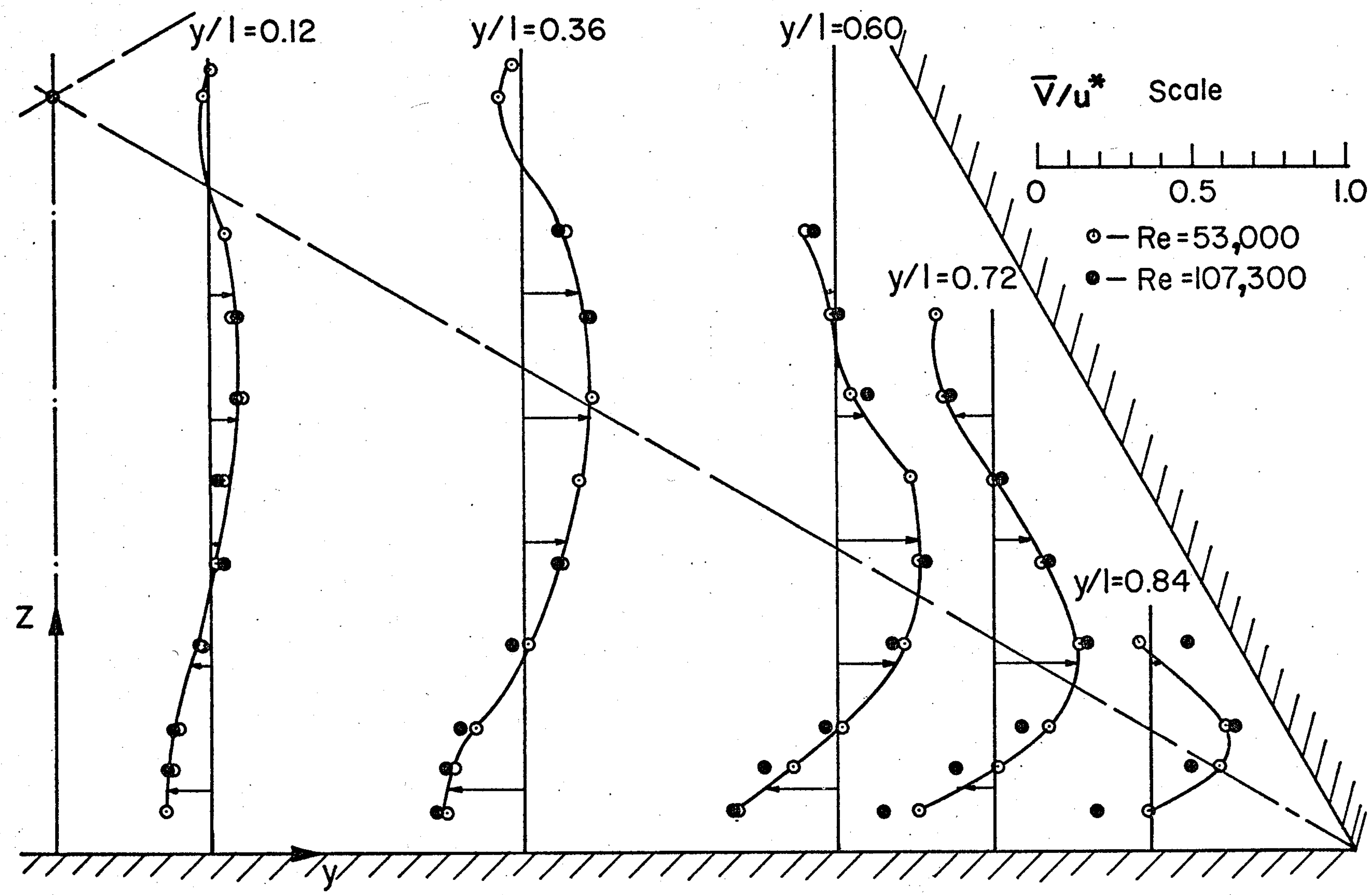

Fig. 35. Profiles of Normalized Secondary Velocity, $\overline{V}/u^*$, in Equilateral Triangular Duct.

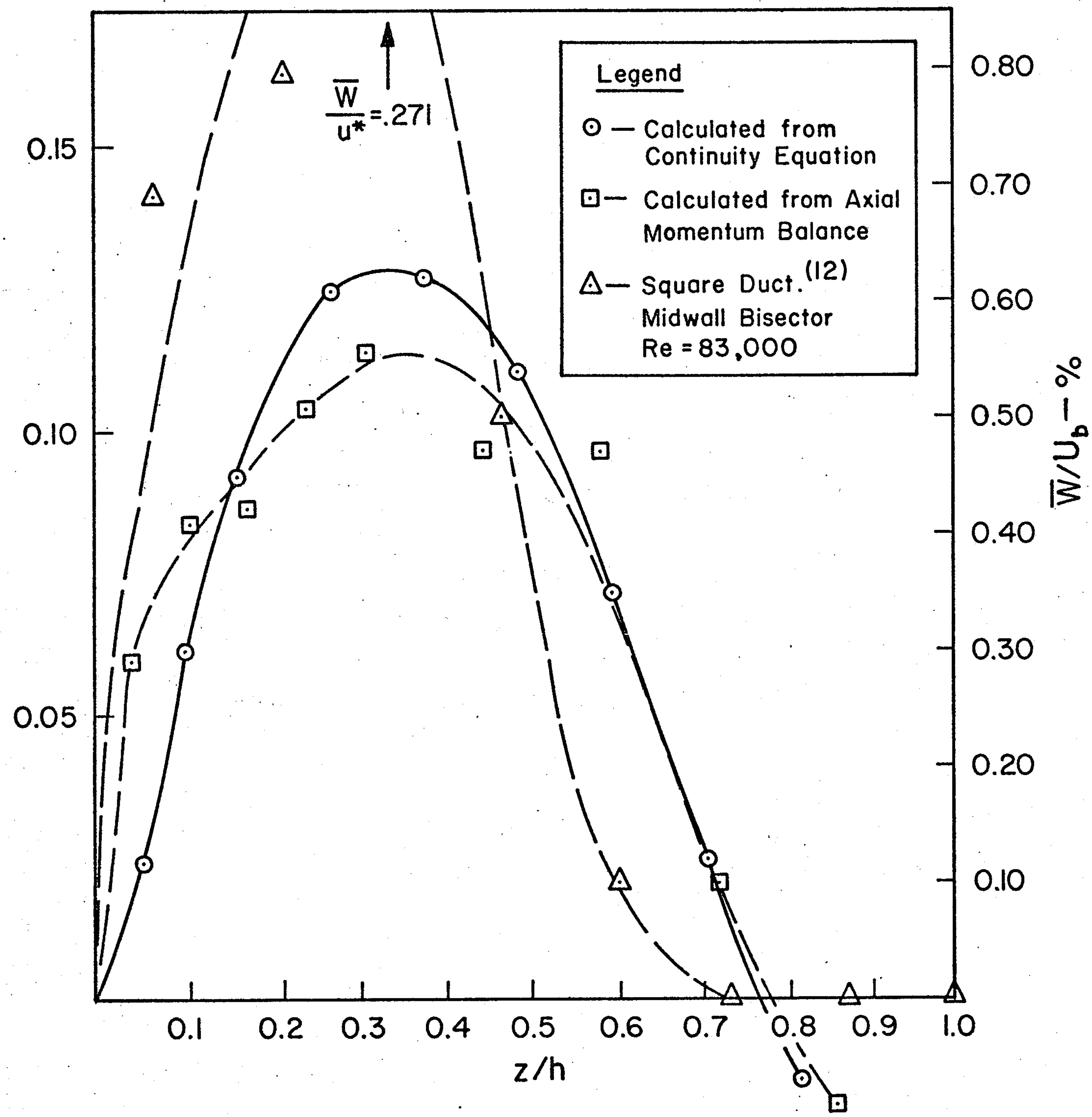

Fig.36. Calculated Distribution of $\overline{W}/u^*$ Along Midwall Bisector in Equilateral Triangular Duct. Re =53,000